CHAPTER THREE

RESULTS AND DISCUSSION*

* The following publications resulted from part of the research work presented in this dissertation and they are not referenced further. Other publications (Appendix A) not directly related to this thesis topic were not reported here but, were cited where necessary.

1. J. Pillay, B. O. Agboola, K. I. Ozoemena, Layer-by-layer self-assembled nanostructured phthalocyaninatoiron(II) / SWCNT-*poly*(*m*-aminobenzenesulfonic acid) hybrid system on gold surface: Electron transfer dynamics and amplification of H_2O_2 response", *Electrochem. Commun.* 11 (2009) 1292.
2. J. Pillay, K.I. Ozoemena, Electrochemistry of 2-dimethylaminoethanethiol SAM on gold electrode: Interaction with SWCNT-poly(*m*-aminobenzene sulphonic acid), electric field-induced protonation-deprotonation, and surface pKa", *Electrochim. Acta* 54 (2009) 5053.
3. J. Pillay, K.I. Ozoemena, T.R. Tshikhudo, "Monolayer-Protected Gold Nanoparticles: Impacts of Stabilizing Ligands on the Heterogeneous Electron Transfer Dynamics and Voltammetric Detection", Submitted to *Langmuir* (2010) DOI: 10.1021/la904463g.
4. B.O. Agboola, J. Pillay, K. Makgopa, K.I. Ozoemena, "Cyclic voltammetric and impedimetric properties of mixed self-assembled nanothin films of water-soluble SWCNT-*poly*(*m*-aminobenzene sulfonic acid) and iron (II) tetra-sulphophthalocyanine at gold electrode", Submitted to *Thin Solid Films*.
5. J. Pillay, K.I. Ozoemena, "Electron transport and voltammetric detection properties of gold nanoparticle-nanosized iron (II) phthalocyanine bilayer films", In preparation.

3 RESULTS AND DISCUSSION

3.1 2-Dimethylaminoethanethiol Self Assembled Monolayer

3.1.1 Electrode Fabrication and AFM Characterization

Scheme 3.1 represents the self-assembly fabrication from bare-Au to Au-DMAET-SWCNT-PABS. The build-up and formation of the films on gold plates were confirmed using AFM technique. Figure 3.1 shows the comparative AFM images of the (a) bare-Au (b) Au-DMAET and (c) Au-DMAET-SWCNT-PABS. There was no significant difference between the thickness of the bare-Au and Au-DMAET, which is expected for this short-chained alkanethiol SAM as other workers [1] also, did not observe any difference between bare-Au and on modification with long-chained SAM of 11-amino-1-undecanethiol. AFM features for the immobilisation of SWCNT-PABS on Au-DMAET show there is clear evidence of flat lying tubes on the surface of the DMAET molecules expected for a side walled functionalised CNTs using the negatively charged sulfonic group to form electrostatic attraction with the positively charged amino of DMAET (Fig. 3.1c).

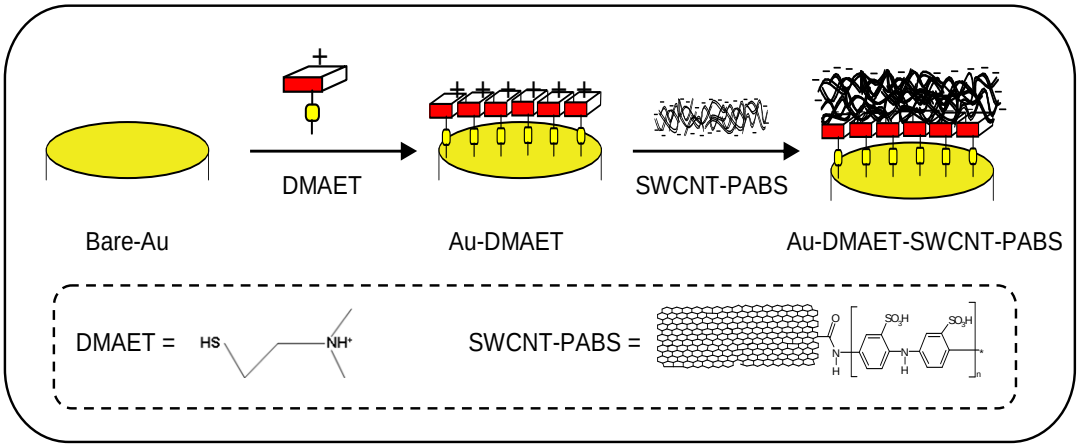

Scheme 3.1: Cartoon showing the schematic representation of the SAM formation of DMAET and DMAET–SWCNT-PABS.

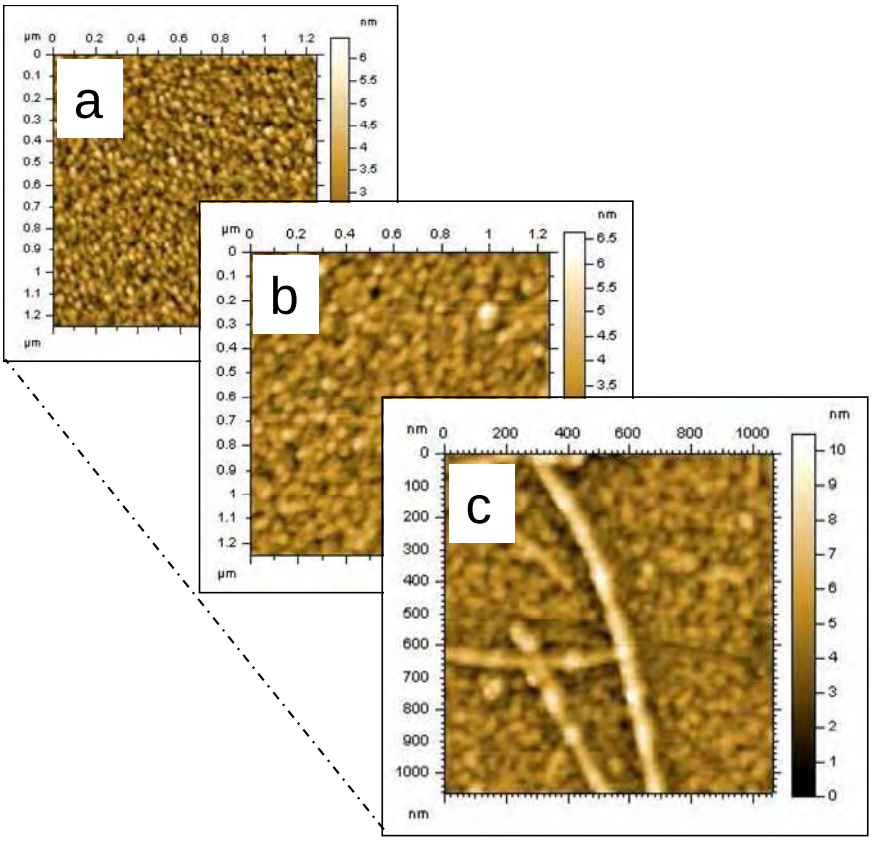

Figure 3.1: Topographic AFM images of (a) bare-Au (b) Au-DMAET and (c) Au-DMAET–SWCNT-PABS.

Furthermore, there is a continuous increase in maximum height (from a–c) as shown by the data in Figure 3.1. Also, the root mean square (R_q) of the roughness profile follows the same trend where, bare-Au (0.81 nm) < Au-DMAET (1.06 nm) < Au-SWCNT-PABS (1.95 nm). These facts provide evidence for the formation of the base monolayer and the subsequent attachment of SWCNT-PABS onto the electrode surface.

3.1.2 Protonation / Deprotonation Effect or Cyclic Voltammetric Behaviour in Various Electrolytes

Figure 3.2 compares the CV profiles of the three electrodes in PBS (pH 7.4). The reversible voltammogram for the Au-DMAET SAM is similar to those observed by White and co-workers for mercaptoundecanoic acid (MUA) SAMs on Ag(III) [2], Burgess and co-workers for MUA on polycrystalline gold [3] and 4-mercaptobenzoic acid (4-MBA) SAMs on polycrystalline gold electrode [4], which I associated with the electric field induced prototonation/deprotonation of the –COOH head groups rather than a Faradaic process.

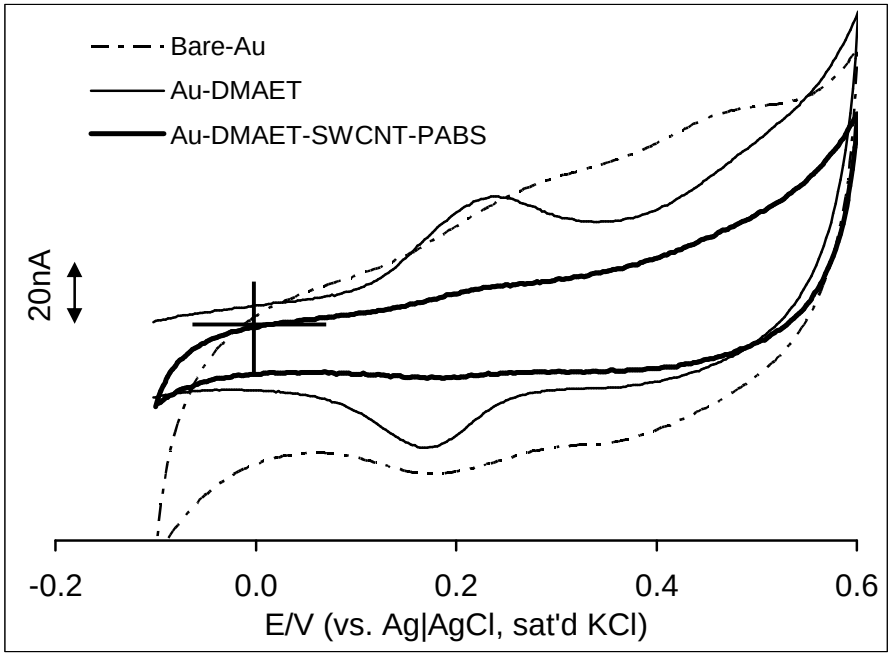

Figure 3.2: Typical cyclic voltammetric evolutions of the bare-Au, Au-DMAET and Au-DMAET–SWCNT-PABS electrodes in PBS pH 7.4.

I believe that the same process is what is being observed in this case, i.e., electric field driven prototonation/deprotonation of the $-N(H)^{+}(CH_3)_2$ head group of the DMAET (Eq. 3.1):

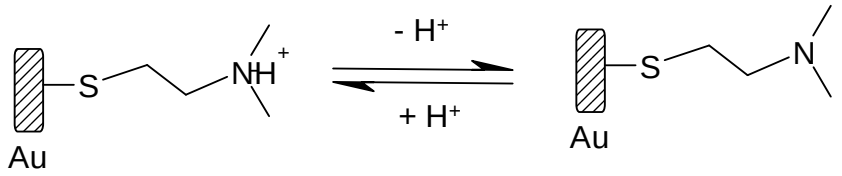

3.1

Figure 3.2 clearly suggests that the integration of the SWCNT-PABS via electrostatic interaction leads to suppression of the

protonation/deprotonation process. To test this hypothesis, I conducted a series of experiments in different unbuffered electrolytes (50 mM K_2SO_4, KCl, NaF, K_2SO_4 and $KClO_4$) with a view to establishing the impact of cations and anions on the evolution of this DMAET reversible voltammogram. As exemplified in Figure 3.3, unlike the NaF and KCl that showed the same reversible process as the PBS, the K_2SO_4 and $KClO_4$ (not shown) suppressed the Au-DMAET voltammogram. Repetitive scanning in any of the electrolyte showed stable voltammograms (exemplified in Figure 3.4 with NaF). It may be inferred from the CVs that (i) the appearance of the reversible peaks in chloride and non-chloride solutions (PBS and NaF) rules out this possibility adsorption/desorption of chloride ions being responsible for the peaks; (ii) cations do not have any impact contrary to the report of Rosentahl and Burgess on 4-MBA [4], and (iii) anions have impact but possibly depend on the size of anion; SO_4^{2-} and ClO_4^- are approximately of the same size and larger than Cl^- that did not show any impact. Unlike the SWCNT-PABS, the original Au-DMAET voltammogram can be regenerated when re-immersed in KCl solution (Fig. 3.3), meaning that SWCNT-PABS is irreversibly adsorbed onto the DMAET while the anions are weakly adsorbed. The CV of the SAM of Sodium 2-mercaptoethanesulphonate (same structure as DMAET, differing only in the head group) was also examined and no peaks

were observed in the PBS (Fig. 3.3 inset), which confirms that the reversible peaks in DMAET SAM arise from its amino head group.

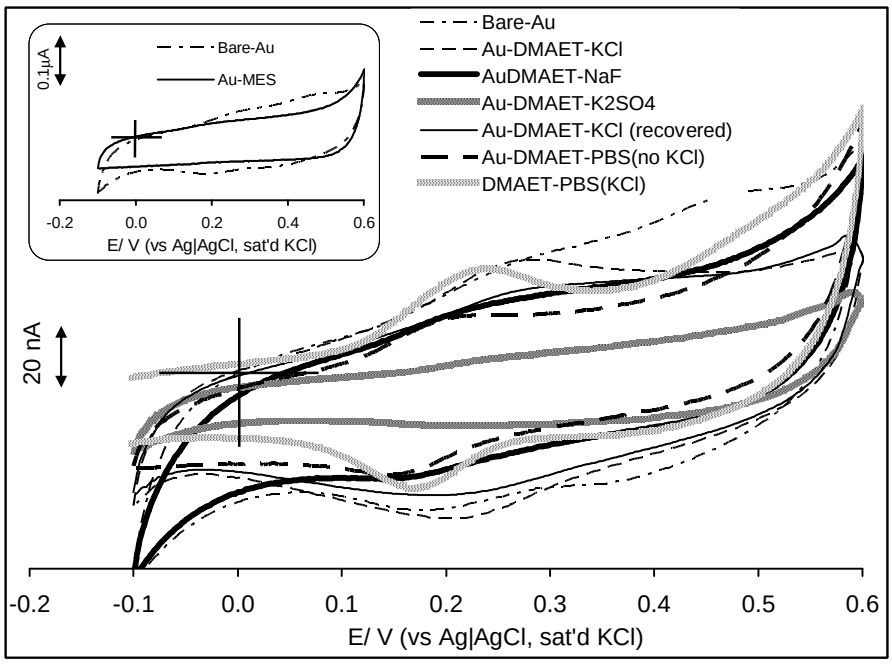

Figure 3.3: Typical cyclic voltammetric evolutions of Au-DMAET in 50 mM PBS (pH7.4), NaF, KCl and K_2SO_4; Inset shows the CV of the Sodium 2-mercaptoethanesulphonate SAM in 50 mM PBS (pH7.4).

Furthermore, the behaviour of the observed peak was also studied in PBS at different pH values. Figure 3.5 shows that the position of the peak potentials shifted as a function of the electrolyte's pH with a slope of *ca.* – 51 mV dec^{-1}.

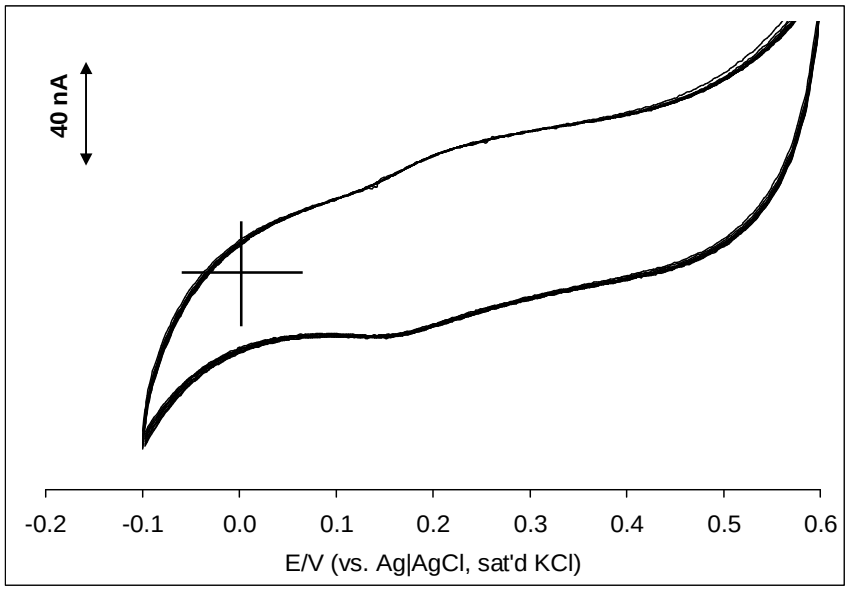

Figure 3.4: Cyclic voltammetric evolutions depicting the repetitive cycling of Au-DMAET in 50 mM NaF.

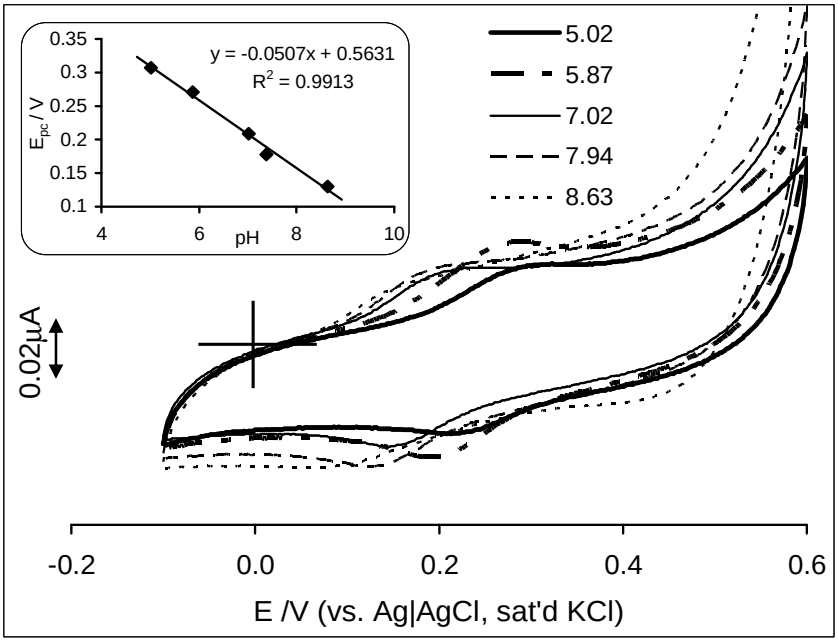

Figure 3.5: Typical cyclic voltammetric evolutions of Au-DMAET in phosphate buffer solutions at different pH levels.

3.1.3 Surface Coverage

Next, cyclic voltammetric reductive desorption experiment in 0.5 M KOH between 0 and –1.2 V (vs. Ag|AgCl sat'd KCl) were conducted. Equation 3.2 represents the chemistry of such irreversible desorption of the DMAET SAM:

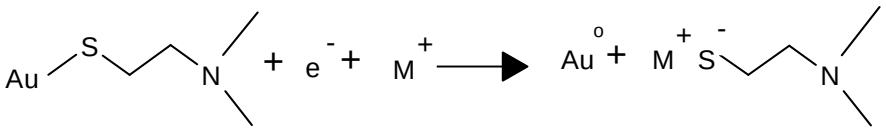

3.2

where, M+ represents the cation from the electrolyte [6]. The same equation holds for the DMAET-SWCNT-PABS. Figure 3.6 shows the sharp desorption peaks at -0.72 V and -0.68 V for DMAET and DMAET-SWCNT-PABS, respectively.

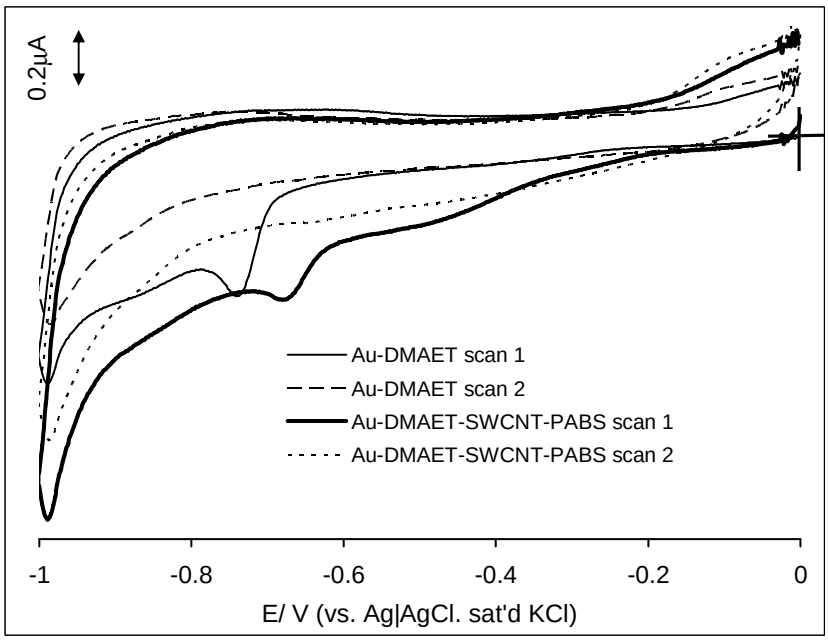

Figure 3.6: Cyclic Voltammetric reductive desorption of DMAET and DMAET-SWCNT-PABS in 0.5 M KOH.

From the area (i.e., charge, Q / C) under the respective reductive peaks, the surface concentrations (Γ_{SAM} /mol cm^{-2}) of the DMAET and DMAET-SWCNT-PABS were estimated from Equation 3.3:

$$\Gamma^{SAM} = \frac{\quad}{\quad} \qquad 3.3$$

where n represents number of electrons transferred (equals 1), F is the Faraday constant and A is the experimentally determined area of the gold electrode. The Γ_{SAM} was approximately 0.53 nmol cm^{-2} for DMAET and 0.58 nmol cm^{-2} for DMAET-SWCNT-PABS. This similar surface coverage for both SAMs suggests that the observed electrochemistry was due to SWCNT-PABS attached onto the surface of the DMAET molecules.

3.1.4 Electron Transfer Dynamics: Estimation of Surface pK_a of DMAET

The charge transfer resistance (R_{ct}/Ω) values, extracted from the impedance spectra using the Randles equivalent circuit shown in Figure 1.5 to fit the data, decreased as Au-DMAET (112 Ω) < Au-DMAET-SWCNT-PABS (115 Ω) < bare-Au (730 Ω). The slightly faster electron transfer recorded at the Au-DMAET compared to the Au-

DMAET-SWCNT-PABS is attributed to the strong electrostatic attraction between the positively charged DMAET and the negatively charged $[Fe(CN)_6]^{3-/4-}$ species.

The pK_a of the surface-confined species is the value of the pH in contact with monolayer when half of the functional groups are ionized [7-9]. Figure 3.7 represents typical impedance spectral profiles of Au-DMAET in PBS solutions of $[Fe(CN)_6]^{3-/4-}$. Increase in solution pH from ~4.5 to 9.0 clearly depicts changes in electron transport, signified by increasing R_{ct} values shown in Figure 3.8. At low pH (< pH 7.0), the $-N(H)^+(CH_3)_2$ head group is mostly protonated (reverse reaction of Equation 3.2 favoured) thereby enhancing electrostatic attraction between the Au-DMAET and the negatively charged $[Fe(CN)_6]^{3-/4-}$ redox probe. However, increase in solution of pH>7.0 leads to an increase in R_{ct} caused by deprotonation process (forward reaction of Equation 3.2 favoured) resulting in electrostatic repulsion between the DMAET head group and the redox probe. From the mid-points of the R_{ct} vs. pH plots (Fig. 3.8), the surface pK_a of the DMAET was estimated as ~7.6, which is about 3 pK_a units lower than its solution pK_a of 10.8 [10].

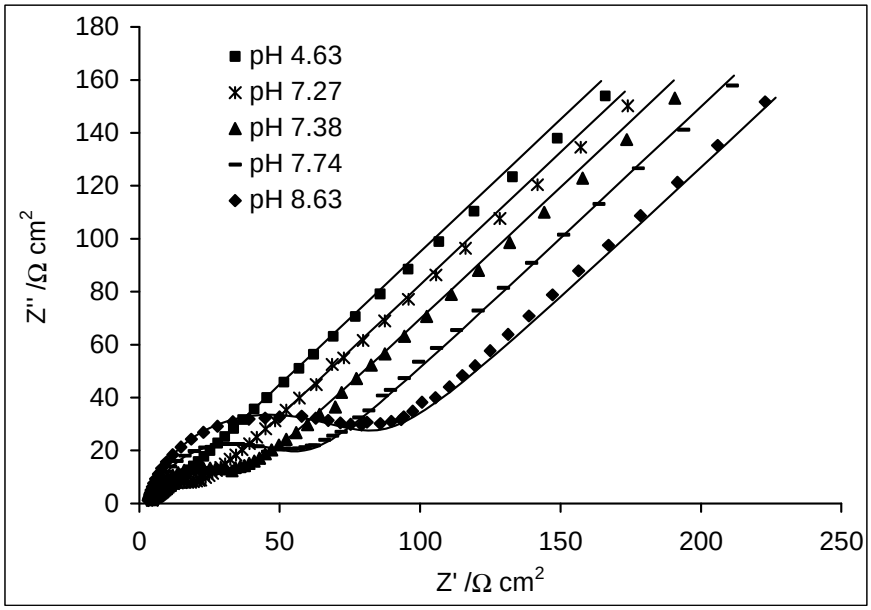

Figure 3.7: Examples of the impedimetric responses of Au-DMAET at different pH values of $[Fe(CN)_6]^{3-}$/ $[Fe(CN)_6]^{/4-}$ solutions.

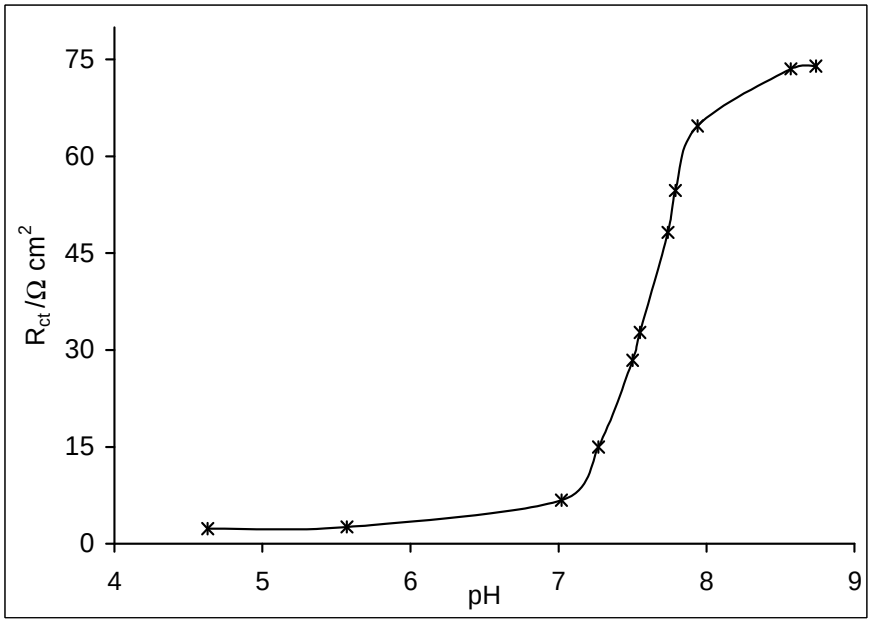

Figure 3.8: Plot of Charge Transfer Resistance (R_{ct}) from the impedimetric responses of Au-DMAET vs. pH in $[Fe(CN)_6]^{3-}$/ $[Fe(CN)_6]^{/4-}$ solutions.

The reason for this large shift of pK_a, as opposed to the usual order of < 1 pK_a is not understood at this time. However, the results are similar to the observation of Saby *et al.* [11] who reported a shift of the pK_a of benzoic acid from a value of 4.2 in solution to a value of 2.8 when covalently attached onto a glassy carbon electrode, which they speculated to be due to some specific interfacial effect between the carbon surface and the carboxylate functionalities or the phenyl ring of the layer. On the other hand, Abinam *et al.* [12] who also observed such large shifts in benzoic acid proved this to be due to some thermodynamic effects. Also, interestingly, Abinam *et al.* [13] observed a large shift in the pK_a of "Jeffamine" from a value of 9.7 in solution to a value of 7.1 when covalently attached onto a carbon substrate and attributed that to entropic contribution arising from the ordering/disordering of solvent molecules at the carbon-water interface. Therefore, these results may be connected with some specific interfacial effect between the DMAET and the gold surface or thermodynamic effects playing some interesting role.

3.2 Single Walled Carbon Nanotubes and Nanosized Iron (II) Phthalocyanine modified Gold Electrodes

3.2.1 LBL Self-Assembly

Figure 3.9 shows the FESEM images of (a) Iron (II) phthalocyanine microcrystals and (b) Iron (II) phthalocyanine nanoparticles (*nano*FePc) clearly confirming the successful nanostructuring of the bulk (crystallite form) FePc molecules to their amorphous, nanoparticles protected by CTAB particles. The EDX profile of *nano*FePc depicted in Figure 3.9 (c) confirms the presence of iron and the sulphur peak at 2.4 eV could have arisen from the synthesis.

The multilayer build-up depicted in Scheme 3.2, involving *nano*FePc and SWCNT-PABS follows the well known LBL technique, where steps (ii) and (iii) are repeated four times for this assembly. To my knowledge, this is the first time this type of molecular building involving both SWCNT-PABS and FePc complex is described.

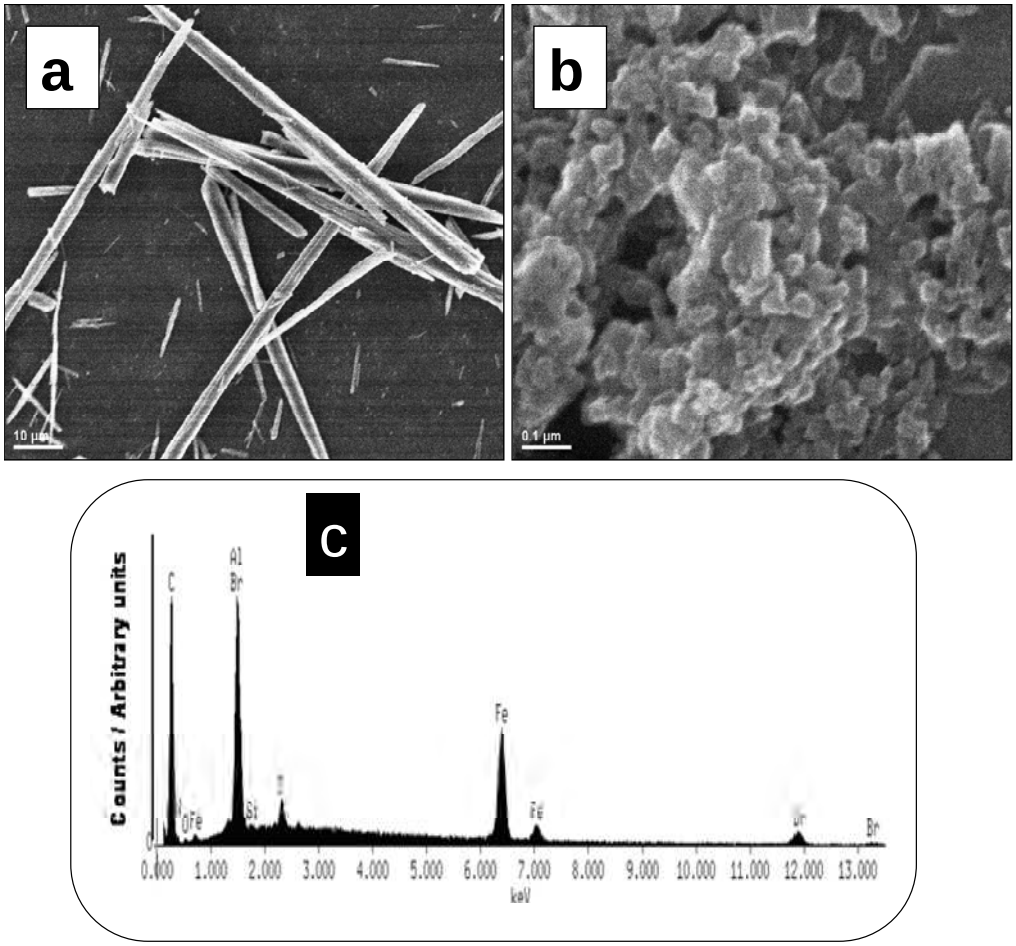

Figure 3.9: Scanning electron microscopy images of (a) Iron (II) phthalocyanine microcrystals and (b) Iron (II) phthalocyanine nanoparticles. (c) EDX profile of Iron (II) phthalocyanine nanoparticles.

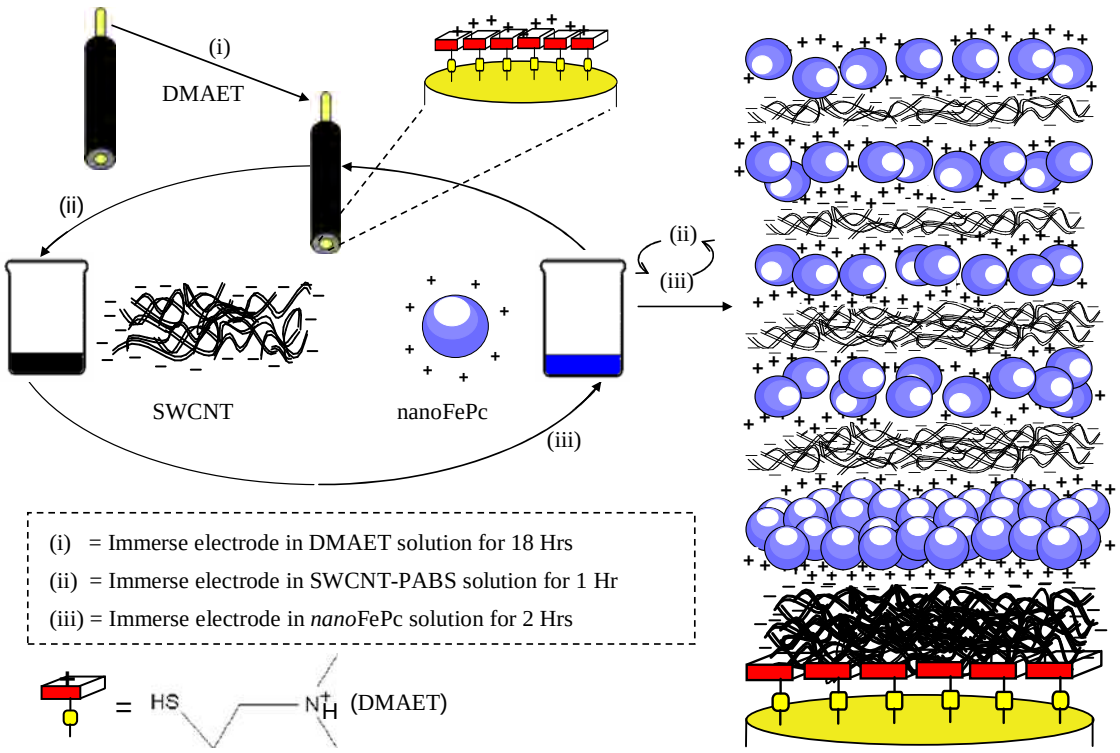

Scheme 3.2: Schematic representation depicting the layer-by-layer assembly of *nano*FePc and SWCNT-PABS on gold surface. The fabrication conditions are as stated in the experimental section. Note that this representation is merely a cartoon, so not drawn to scale.

3.2.2 Characterization

3.2.2.1 Atomic Force Microscopy

The AFM images of the bare-Au, Au-DMAET and Au-DMAET-SWCNT-PABS are shown and discussed in section 3.1.1. Figure 3.10 shows typical 3-D AFM images of (a) Au-DMAET-SWCNT-PABS and (b) Au-DMAET-(SWCNT-PABS-*nano*FePc)$_1$, (c) Au-DMAET-(SWCNT-PABS-*nano*FePc)$_3$ and (d) Au-DMAET-(SWCNT-PABS-*nano*FePc)$_5$.

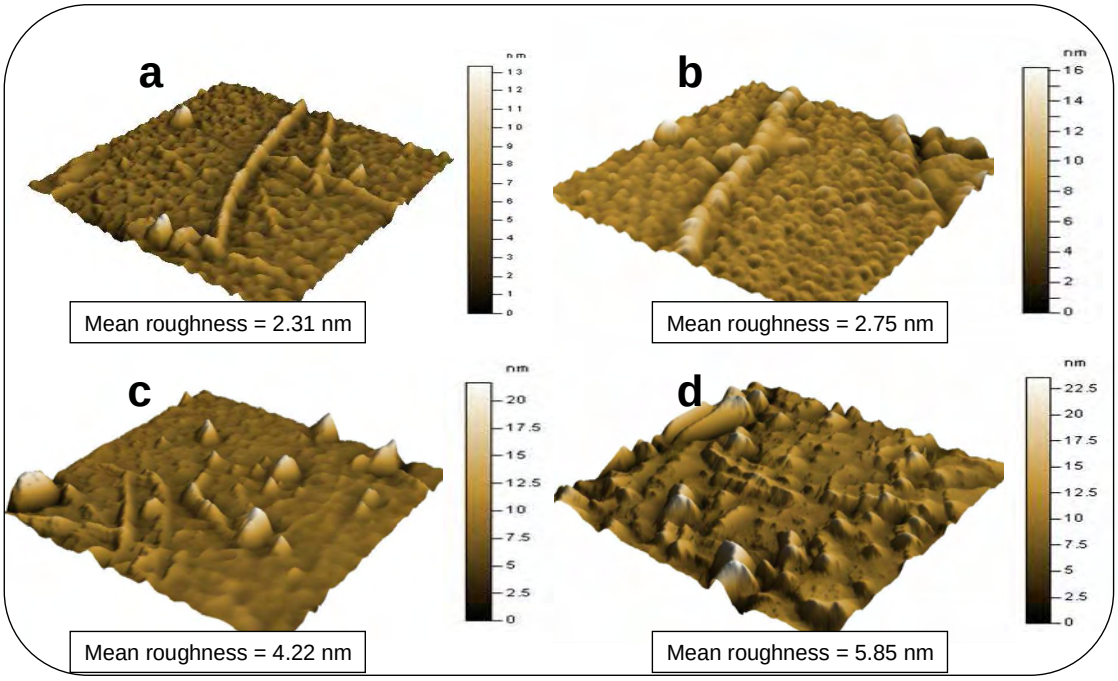

Figure 3.10: 3-D AFM images of (a) Au-DMAET-SWCNT-PABS and (b) Au-DMAET-(SWCNT-PABS-*nano*FePc)$_1$, (c) Au-DMAET-(SWCNT-PABS-*nano* FePc)$_3$ and (d) Au-DMAET-(SWCNT-PABS-*nano*FePc)$_5$.

As can be seen from the data in Figure 3.10, there is a continuous increase (from a–d) in the root mean square deviation (R_q) and maximum height (R_z) of the roughness profiles, indicating the formation of the various modifiers on gold plate. The electrostatic attraction between the negatively charged SWCNT-PABS and the positively charged *nano*FePc particles resulted in an aggregation of *nano*FePc particles forming clusters in the path of the tubes (Fig. 3.10b). Other important observations here include that the first SWCNT-PABS layer on the electrode (i.e, DMAET-SWCNT-PABS) is

much thicker than subsequent SWCNT-PABS layers (*nano*FePc-SWCNT-PABS), suggesting that the interaction between the base monolayer (DMAET) and SWCNT-PABS is stronger than that between SWCNT-PABS and *nano*FePc. Previous investigations have shown that MPC and related complexes strongly adsorb on CNT-modified electrodes [14]. In addition, *nano*FePc is thicker on the first bilayer compared to the subsequent bilayers, possibly due to the strong electrostatic interactions between DMAET and SWCNT-PABS. The AFM images (exemplified in Figure 3.10) show growth and formation of SWCNT-PABS-*nano*FePc films' root mean square (rms) increasing proportionally with increasing bilayers (Fig. 3.11).

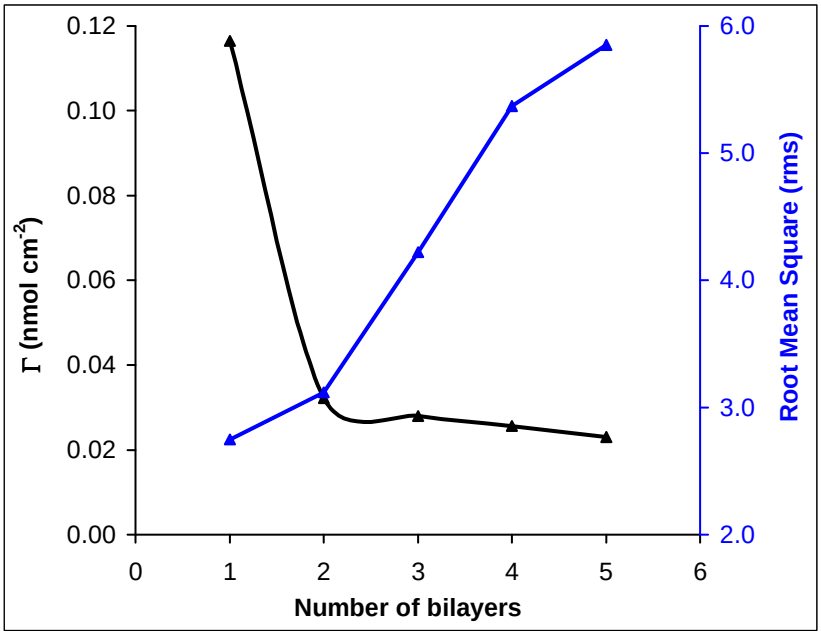

Figure 3.11: Plot of surface coverage (Γ) and Root Mean Square (rms) of *nano*FePc vs. bilayers.

3.2.2.2 Surface Coverage

Cyclic voltammetric evolutions of the bilayers in PBS (Fig. 3.12) showed clear quasi-reversible redox couple centered at $E_{1/2}$ ≈ 0.22 V (vs. Ag|AgCl, sat'd KCl) which, based on redox-active FePc thin fims reports, is attributable to the Fe^{III}/Fe^{II} redox couple [15]. Both Au-DMAET and Au-DMAET-SWCNT-PABS exhibited similar quasi-reversible processes as for the bilayers (not shown) but these couples are very weak with current responses much smaller (~ in the nA range) than the *nano*FePc (in the μA), supporting the assumption that the redox process is due to *nano*FePc. As the bilayer increases, the charges (anodic and cathodic) decreased.

The surface coverage (Γ_{MPc} /mol cm^{-2}) for each of the SWCNT-PABS-*nano*FePc bilayers was obtained by integrating the anodic charges (Q) and employing the formula given in Equation 3.3. From the plot of surface coverage vs. the number of bilayers (Fig. 3.11), the first layer (120 pmol cm^{-2}) was higher than the subsequent (2 – 5) bilayers (*ca.* 30 pmol cm^{-2}), implying that the first *nano*FePc layer mainly assumed standing/vertical orientation while the subsequent *nano*FePc layers lie flat on the underlying SWCNT-PABS layers (as depicted in the multi-layer cartoon, scheme 3.2). The highest coverage seen on the first bilayer suggests presence of more *nano*FePc than subsequent layers, corroborating the AFM topographic evolutions.

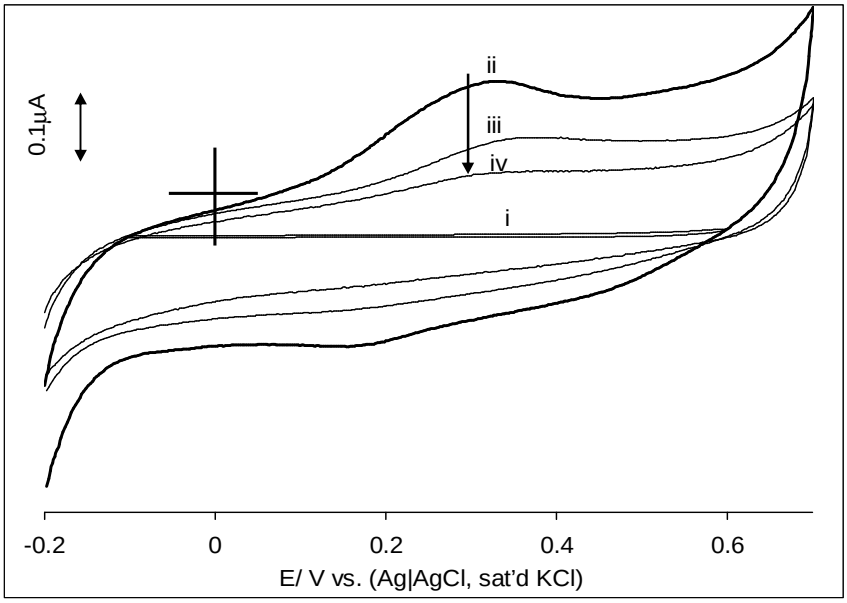

Figure 3.12: Typical CV profiles of (i) bare-Au, (ii) 1st, (iii) 3rd and (iv) 5th bilayers at a scan rate of 30 mV s^{-1} in PBS (pH 7.4). Current response decreases from (ii) to (iv), indicated by the direction of the arrow as the number of bilayers increase.

3.2.2.3 Cyclic Voltammetry

Figure 3.13 illustrates the CV evolutions of the electrodes in the same electrolyte conditions (5 mM $[Fe(CN)_6]^{4-}$ / $[Fe(CN)_6]^{3-}$). The experiment was aimed at answering the question as to what extent do the modifying species permit the electron transfer of the $[Fe(CN)_6]^{4-}$ / $[Fe(CN)_6]^{3-}$ to the underlying gold electrode. The CV responses of the electrodes (including the *nano*FePc-SWCNT-PABS (not shown) as the outer most layer) were essentially the same in terms of (i) the anodic (I_{pa}) and cathodic (I_{pc}) peak current heights, (ii) the peak-to-peak

separation potential ($\Delta E_p \approx 70$ mV vs. Ag|AgCl, sat'd KCl), and (iii) the equilibrium potential ($E_{1/2} \approx 0.25$ V vs. Ag|AgCl, sat'd KCl).

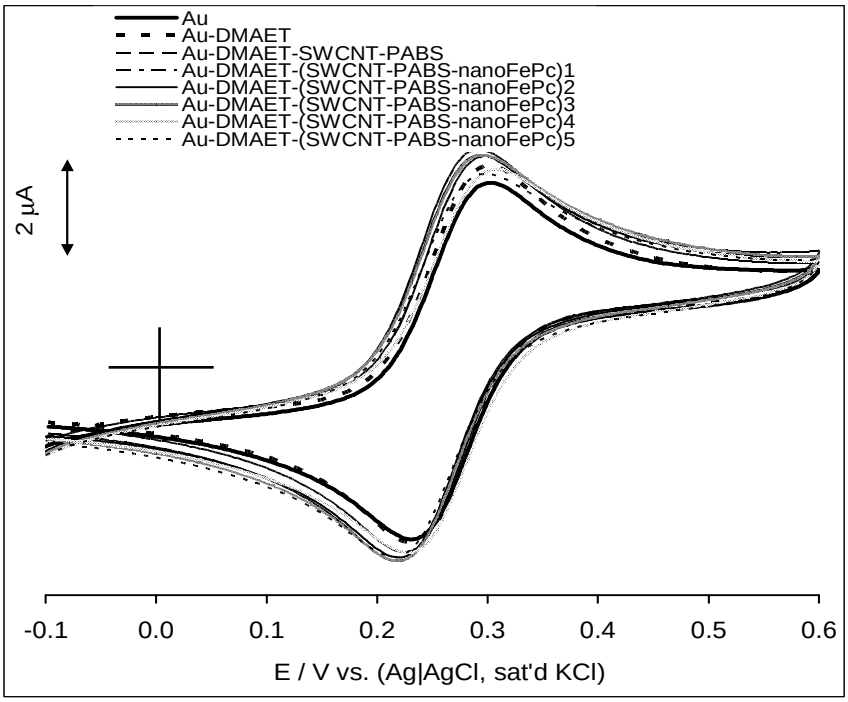

Figure 3.13: Typical CV profiles of the bare-Au, Au-DMAET, Au-DMAET-SWCNT-PABS and Au-DMAET-(SWCNT-PABS-*nano*FePc)$_{1\text{-}5}$ assemblies in 0.1 M KCl containing equimolar mixture of $[Fe(CN)_6]^{3-}$/ $[Fe(CN)_6]^{/4-}$ solutions at a scan rate of 25 mV s^{-1}.

3.2.2.4 Electrochemical Impedance Spectroscopy

Impedance spectroscopy provides a better description of the electrochemical system compared to cyclic voltammetry [16] and was therefore employed to follow the charge transfer kinetics occurring at these electrodes. The nyquist plots shown in Figure 3.14 for the bare-Au, Au-DMAET, Au-DMAET-SWCNT-PABS and subsequent bilayers

satisfactorily fitted (in terms of low percent errors obtained after several iterations, Table 3.1) the modified Randles equivalent circuit (Fig. 1.8a).

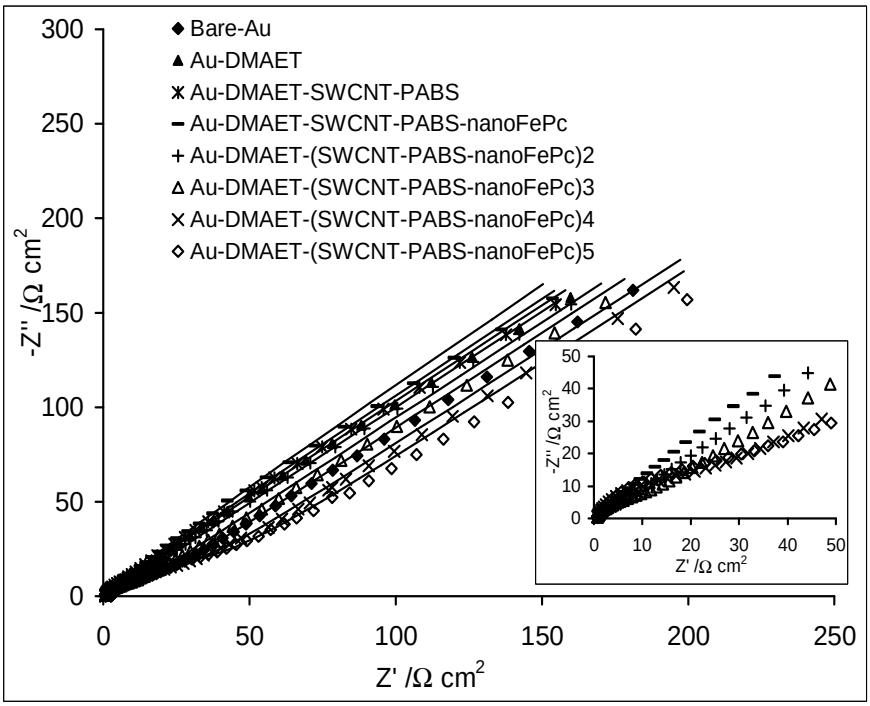

Figure 3.14: Nyquist plots resulting from the bare-Au, Au-DMAET, Au-DMAET-SWCNTPABS and Au-DMAET-(SWCNT-PABS-*nano*FePc)$_{1-5}$ assemblies in 0.1 M KCl containing equimolar mixture of $[Fe(CN)_6]^{3-}$/ $[Fe(CN)_6]^{/4-}$ solutions. Inset shows the high frequency area of the bilayers only.

This equivalent circuit comprised the mixed kinetic and diffusion-controlled processes with R_s as the resistance of the electrolyte and electrode, R_{ct} as the charge-transfer resistance (domain of kinetic control) and Z_w as the Warburg impedance (domain of mass transport

control) resulting from the linear diffusion of redox probe ions from the bulk electrolyte. It is also likely that mass transport is limited by diffusion within and inside the layered structure. Given the inherent roughness of the bare and modified gold surfaces (as also seen from the AFM images), the constant phase angle element, in which the double layer capacitance is replaced by CPE in the Randles' model was used to describe impedimetric data. CPE is ascribed to the energetic non-homogeneity arising from the surface roughness of the electrode. The impedance (Z_{CPE}) is a power-law dependent interfacial capacity given as shown in Equation 1.18:

$$Z_{CPE} = Q(j\omega)^{-n}$$

As previously mentioned n is an exponent (n≤1 for a physically reasonable situation) equals unity for the case of ideal capacitor. It is important to note that the n values lie approximately between 0.7 and 0.8 suggesting pseudocapacitive behavior. The Z_w values, which correspond to the diffusion process of the oxidized and reduced species of the $[Fe(CN)_6]^{3-/4-}$ couple, are approximately of the same magnitude for all the electrodes. Ideally, R_s and Z_w should not be affected by modification of the electrode surface [17].

From data in Table 3.1, the Au-DMAET gave the fastest electron transfer, which may be explained as the consequence of the strong

electrostatic attraction between the positively charged DMAET and the negatively charged $[Fe(CN)_6]^{3-/4-}$ species. In general, the result indicates that charge transfer processes between the $[Fe(CN)_6]^{3-/4-}$ and the underlying gold surface are easier on the initial bilayers than the subsequent bilayers. This may be due to the build-up of the negatively charged SWCNT-PABS leading to more repulsive interaction between the SWCNT-PABS and $[Fe(CN)_6]^{3-/4-}$ species. The modified electrode exhibited stable electrochemistry as each of the voltammograms recorded did not change after several repetitive cycling. After the fifth bilayer, there was no significant change.

The comparative Bode plots of -Phase angle vs. log f is shown in Figure 3.15 (a) showing well-defined symmetrical peaks at different maxima for the different electrodes, corresponding to the different relaxation processes of the electrode|solution interfaces. In all cases, the phase angles were less than 90°, confirming the pseudo-capacitive nature of the electrodes. The bare-Au gave a maximum value of ~41° at 316 Hz corresponding to the relaxation process of the Au|solution interface. Upon modification with the DMAET, this relaxation process is depressed. However when modified with the SWCNT-PABS and the first bilayer, the relaxations shifts to ~ 50° range and at lower frequencies (0.1- 10000 Hz range). Interestingly, from the 2nd to subsequent bilayers, the peaks shift to 43.6° to 60.3° at

approximately the same frequency (1 kHz). These data clearly confirm that the $[Fe(CN)_6]^{3-/4-}$ redox reactions now take place at the surface of the modifying films rather than directly on the bare-Au surface. The log |*Z*| vs. log f type bode plot represented in Figure 3.15 (b) was also studied.

Table 3.1: Summary of the electrochemical impedance spectroscopic evolutions of the electrodes (*n* = 5), percentage errors from fitting the raw EIS data are shown in bracket.

Electrode	**Electrochemical impedance spectral parameters**				
	R_s (Ω cm^2)	**CPE (μF cm^{-2})**	**n**	**R_{CT} (Ω cm^2)**	**10^6 Z_w (Ω cm^2)**
bare-Au	2.66 (0.6)	19.18 (4.7)	0.84 (0.7)	14.68 (2.1)	2.12 (0.3)
Au-DMAET	0.79 (2.1)	18.45 (4.7)	0.85 (0.7)	2.25 (6.6)	2.21 (0.4)
Au-DMAET-SWCNT	0.61 (2.6)	28.7 (11.3)	0.67 (1.5)	2.31 (8.5)	2.17 (1.2)
Au-DMAET-(SWCNT-*nano*FePc)$_1$	0.63 (1.1)	29.01 (4.9)	0.69 (0.7)	2.45 (5.1)	2.03 (1.0)
Au-DMAET-(SWCNT-*nano*FePc)$_2$	0.69 (2.4)	20.96 (11.8)	0.85 (2.5)	3.54 (11.1)	2.28 (0.8)
Au-DMAET-(SWCNT-*nano*FePc)$_3$	0.60 (2.5)	15.21 (6.2)	0.82 (1.1)	10.57 (3.6)	2.15 (0.5)
Au-DMAET-(SWCNT-*nano*FePc)$_4$	0.58 (5.2)	12.58 (8.4)	0.82 (1.3)	25.68 (4.1)	2.01 (1.4)
Au-DMAET-(SWCNT-*nano*FePc)$_5$	0.52 (4.4)	9.89 (6.0)	0.80 (0.9)	34.30 (2.9)	2.07 (1.21)

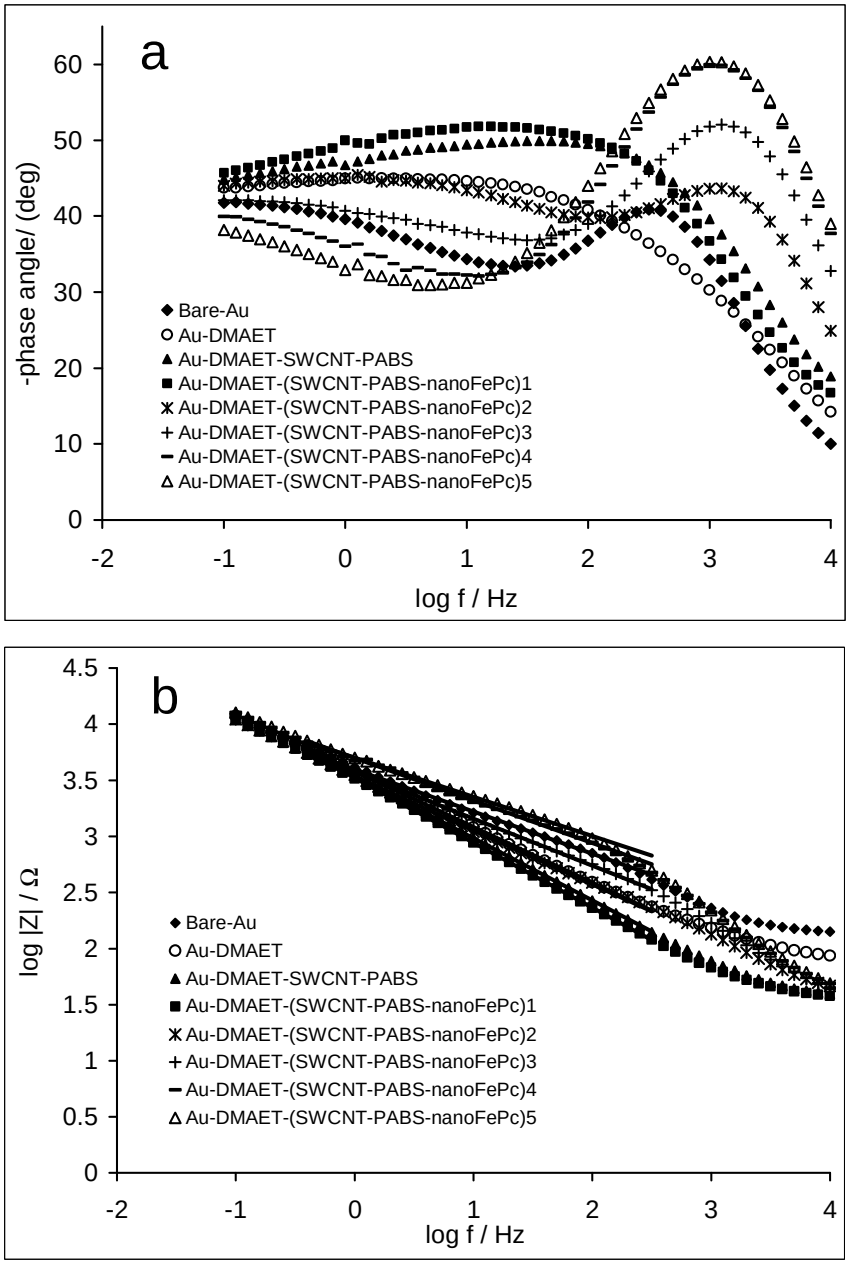

Figure 3.15: Bode plots of (a) -phase angle vs. log f and (b) log |Z| vs. log f for the bare-Au, Au-DMAET, Au-DMAET-SWCNT-PABS, Au-DMAET-(SWCNT-PABS-*nano*FePc)$_{1\text{-}5}$ bilayer assemblies in 0.1 M KCl containing equimolar mixture of $[Fe(CN)_6]^{3-}$/ $[Fe(CN)_6]^{4-}$ solutions.

From Figure 3.15 (b) the following slope values: -48 (r^2=0.999), -0.50 (r^2=0.999), -0.55 (r^2=0.999), -0.58 (r^2=0.999), -0.48 (r^2=0.999), -0.42 (r^2=0.999), -0.48 (r^2=0.998) and -0.45 (r^2=0.995) were obtained for bare-Au, Au-DMAET, Au-DMAET-SWCNT-PABS, 1st, 2nd, 3rd, 4th and 5th bilayers respectively. These slopes correspond to Warburg impedances and confirm that the SAMs studied in the work are redox-active and are not true capacitors as the estimated slopes are far from the ideal minus one value expected for true capacitors and usually observed for electro-inactive SAMs of alkanethiols.

3.2.3 Amplification of H_2O_2 Electrochemical Response

The possibility of using the electrode as a potential sensor for H_2O_2 in physiological pH conditions (pH 7.4) was also investigated. Figure 3.16 compares the reduction current responses of 1 mM H_2O_2 in PBS (pH 7.4) at increasing bilayers (*nano*FePc being the exposed layer, Figure 3.16a) and (SWCNT-PABS as the exposed layer, Figure 3.16b). The results show that unlike the *nano*FePc layers (Fig. 3.16a), when SWCNT-PABS forms the exposed layer of the electrode (Fig. 3.16b); there is no significant improvement in the response of H_2O_2 at a constant concentration. The results suggest that while *nano*FePc acts as the electrocatalyst, the SWCNT-PABS simply acts as the electron conducting nanowires for the reaction. This electrochemical

amplification of the current response of H_2O_2 by *nano*FePc multilayer is remarkable as it promises to provide a viable platform for the development of biosensors. From the current responses of the Au-DMAET-(SWCNT-PABS-*nano*FePc)$_5$ to changes in the concentrations of H_2O_2, the limit of detection and sensitivity was calculated to be 5.5×10^{-4} M and 0.87 m AM^{-1}, respectively. The modified electrode was stable and repeatedly used for the detection of H_2O_2 without significant deterioration of current signals.

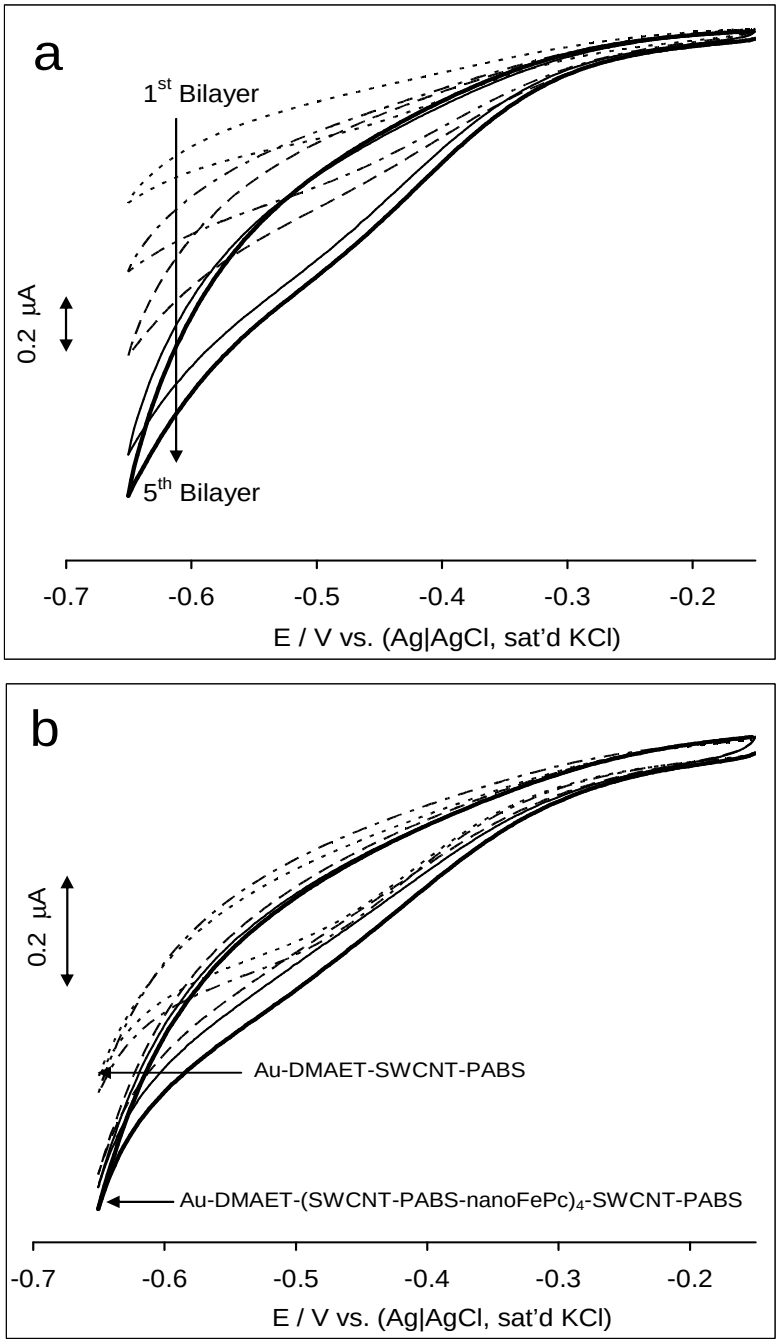

Figure 3.16: Typical CV profiles showing the impact of increasing (a) bilayer (*nano*FePc being the exposed layer) and (b) SWCNT-PABS layers (SWCNT-PABS as the exposed layer) on the current response of 1 mM H_2O_2 in PBS (pH 7.4). Scan rate: 25 mV s^{-1}.

3.2.3.1 Chronoamperometric Analysis

Based on the CV results described above, chronoamperometric technique was employed for the analysis of H_2O_2 (-300 mV) using the multilayer film electrode Au-DMAET-(SWCNT-*nano*FePc)$_5$ in pH 7.4 PBS. Figure 3.17 shows the chronoamperogram that was obtained for a series of H_2O_2 concentrations (0.032-0.268) mM.

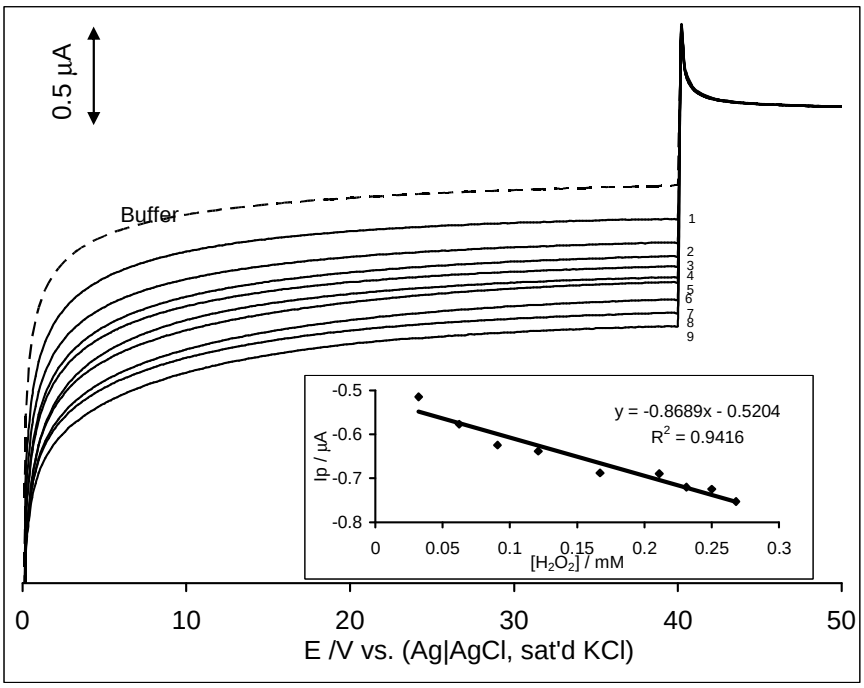

Figure 3.17: Chronoamperometric profile analysis of H_2O_2 in pH 7.4 PBS at a Au-DMAET-(SWCNT-*nano*FePc)$_5$ for a potential step of -300mV vs. Ag|AgCl. The numbers 1-9 correspond to 0.032, 0.062, 0.091, 0.121, 0.167, 0.211, 0.231, 0.250 and 0.268 mM H_2O_2 respectively.

From the current responses of the Au-DMAET-(SWCNT-*nano*FePc)$_5$ and the changes in the H_2O_2 concentration, the limit of detection (LoD

= 3.3s/m) [18], where s is the standard deviation of the intercept and the sensitivity, m, which is the slope of the plot of linear peak current vs. the concentration of H_2O_2,(inset Figure 3.17). The calculated values for the LoD and sensitivity are 5.50 x 10^{-4} M and -0.869 m AM^{-1} respectively. All data were obtained with the same electrode, rinsing the electrode prior to immersing it in a new concentration. Au-DMAET-(SWCNT-*nano*FePc)$_5$ was used in determining the catalytic rate constants and diffusion coefficients of H_2O_2 at constant concentration (at 10 μM in pH 7.4 PBS) poised at -0.3 V using the established Equation [19]:

$$\frac{I_{cat}}{I_d} = \gamma^{1/2}[\pi^{1/2} erf(\gamma^{1/2}) + \frac{\exp^{(-\gamma)}}{\gamma^{1/2}}] \qquad 3.4$$

where, $\gamma = kCt$ is the argument of the error function and in cases where $\gamma > 1.5$, erf($\gamma^{1/2}$) is almost equal to unity and the Equation 3.4 can be reduced to the following Equation 1.14:

$$\frac{I_{cat}}{I_L} = \pi^{1/2}(kC_o t)^{1/2}$$

where the symbols retain their usual meaning. At intermediate times (0– 2 s) of the chronoamperometric measurements the catalytic currents (I_{cat}) were dominated by the rate of the electrocatalyzed reduction of H_2O_2, therefore Equation 1.14 was used to calculate the

rate constant for the chemical reaction between H_2O_2 and the redox sites of surface immobilized $(SWCNT\text{-}nanoFePc)_5$. The plots of I_{cat}/I_L vs. $t^{1/2}$ (Fig. 3.18a) at different H_2O_2 concentrations for Au-DMAET-$(SWCNT\text{-}PABS\text{-}nanoFePc)_5$ were linear. The catalytic rate constant, k, calculated from the plot of slopes^2 vs. H_2O_2 concentration (Fig. 3.18b) is 12.15 $M^{-1}\ s^{-1}$.

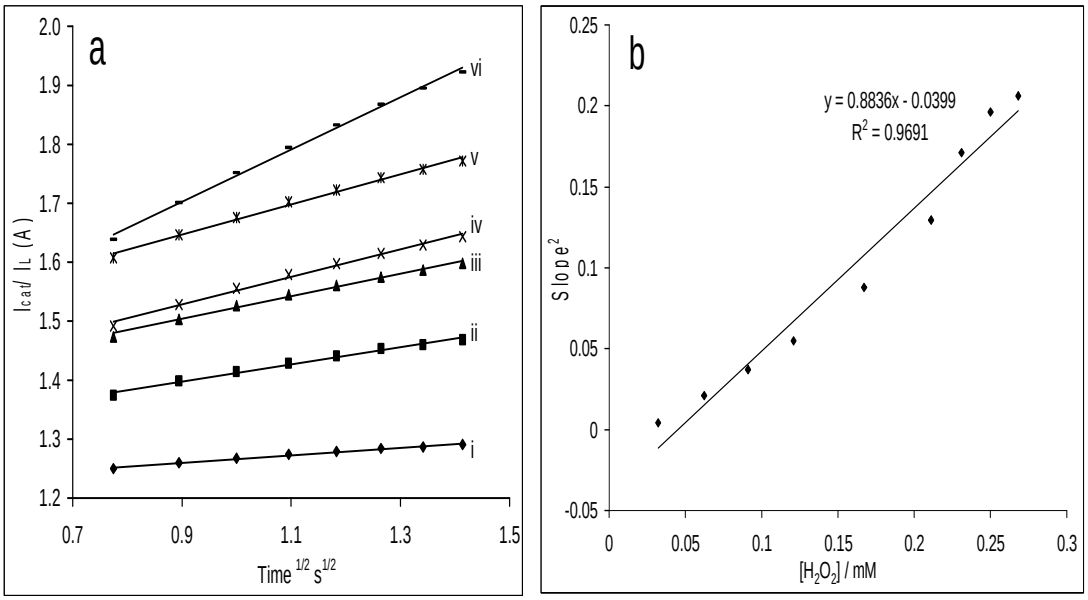

Figure 3.18: Plots of (a) I_{cat}/I_L vs. $t^{1/2}$ and (b) Slopes^2 vs. $[H_2O_2]$. The roman numerals (i) to (vi) correspond to 32.3, 62.5, 90.9, 121, 167 and 250 μM, respectively. Concentration values were selected for clarity.

Also, from the chronoamperometric data, the diffusion coefficient, D, was determined using the Cottrell equation represented in Equation 1.13:

$$I = nFAD^{1/2}C\pi^{-1/2}t^{-1/2}$$

where the symbols retain their usual meaning. The plots of I_{cat} vs. time$^{-1/2}$ (Fig. 3.19a) at different H_2O_2 concentrations for Au-DMAET-(SWCNT-PABS-nanoFePc)$_5$ were linear, and from the subsequent plot of the respective slopes vs. H_2O_2 concentration (Fig. 3.19b), the diffusion coefficient was calculated to be 12.80 x 10 cm^2 s^{-1}. The values vary from one electrode to another; various D values have been reported in literature [20, 21]. Yang et al. [20] reported a value of 2.0x10^{-9} cm^2 s^{-1} for epinephrine at GCE-cys-nanoAu while Wang et al. [21] reported a value of 7.4 x 10^{-5} cm^2 s^{-1} at nano-Au-mixed dithiothreitol/dodecanethiol gold electrode.

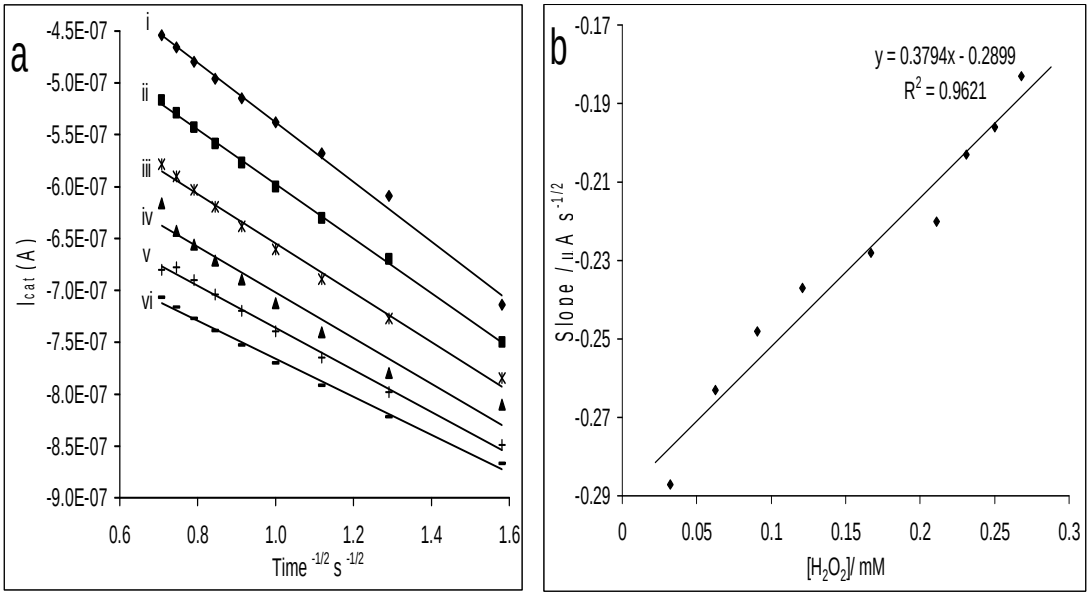

Figure 3.19: Plots of (a) I_{cat} vs. $t^{-1/2}$ and (b) Slopes vs. [H_2O_2]. The roman numerals (i) to (vi) correspond to 32.3, 62.5, 121, 211, 231 and 268 μM, respectively. Concentration values were selected for clarity.

3.2.4 Comparative Electrocatalytic Responses at Electrodes towards Epinephrine

The layer-by-layer assembly depicted in Figure 3.20 involving SWCNT-PABS and *nano*FePc showed an increase in bilayer formation results in a decrease in epinephrine current response. Figure 3.21 compares the cyclic voltammetric evolutions of 10 μM EP at bare-Au, Au-DMAET, Au-DMAET-SWCNT-PABS and Au-DMAET-SWCNT-PABS-*nano*FePc in phosphate buffer solution. The cyclic voltammetric evolutions obtained in buffer solution alone have been dealt with and discussed in section 3.1.2.

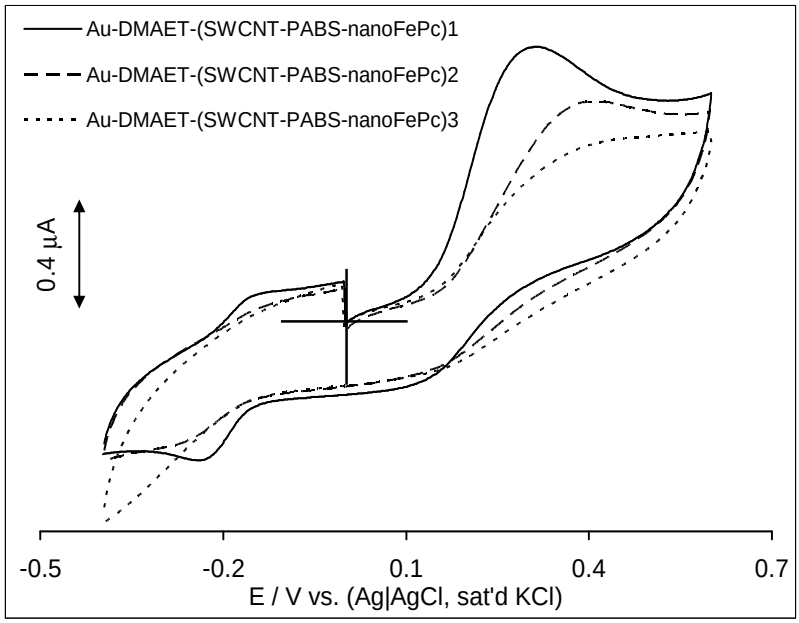

Figure 3.20: Cyclic voltammetric profiles of Au-DMAET-(SWCNT-PABS-*nano*FePc)$_{1-3}$ assemblies in 10 μM epinephrine in PBS (pH 7.4). Scan rate: 25 mV s^{-1}.

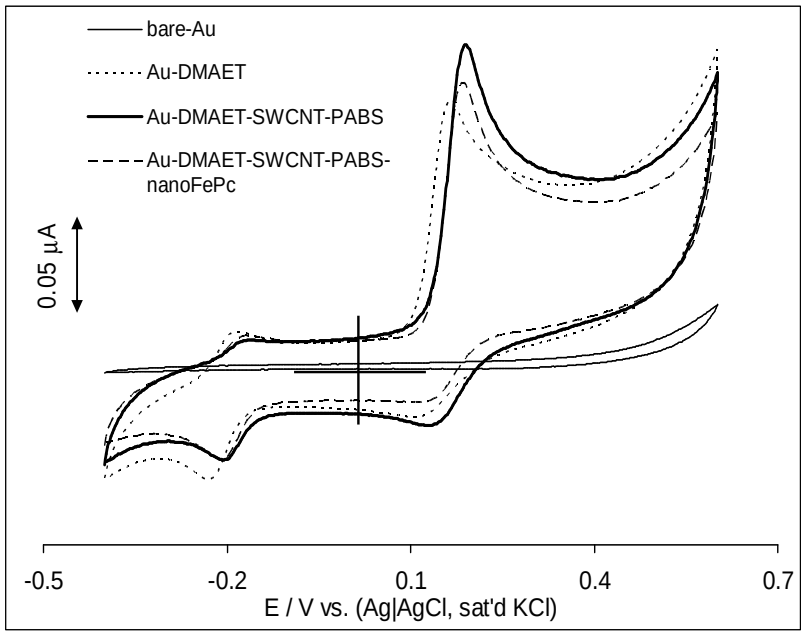

Figure 3.21: Cyclic voltammetric evolutions in the presence of 10 µM epinephrine in PBS (pH 7.4) at bare-Au, Au-DMAET, Au-DMAET-SWCNT-PABS and Au-DMAET-SWCNT-PABS-*nano*FePc. Scan rate: 25 mV s^{-1}.

The observed CV evolutions are characteristic of epinephrine redox process [22-23] involving an irreversible anodic peak at the anodic potential window (corresponding to the oxidation of epinephrine to epinephrinequinone), and at the reduction window, a pseudo-reversible couple corresponding to processes due to epinephrinequinone/ leucoadrenochrome and leucoadrenochrome/ adrenochrome. It can be seen from the comparative CV profiles in Figure 3.21 that Au-DMAET-SWCNT-PABS shows greater catalytic response towards the detection of 10 µM epinephrine compared to Au-

DMAET-SWCNT-PABS-*nano*FePc, Au-DMAET and bare-Au. However, it has been documented that Au-cys-SWCNT and Au-cys-SWCNT-CoTAPc show similar catalytic response in terms of current response towards the detection of epinephrine [24]. Therefore, the effect of electrode passivation was investigated.

3.2.4.1 Passivation Studies

Electrode passivation occurs when the surface of the electrode becomes 'blocked' by the species in solution. This implies that the electrodes may demonstrate a similar current response after a few scan as apposed to only after the initial scans. The extent of passivation for the electrodes in relation to each other can be measured from the plot of epinephrine peak current, I_p vs. number of scans shown in Figure 3.22. The percentage decrease in the peak current, I_p after the first scan for Au-DMAET is ~35% greater than the percentage decrease in the current after the first scan of Au-DMAET-SWCNT-PABS and Au-DMAET-(SWCNT-PABS-*nano*FePc)$_1$. After the second scan it can be seen that Au-DMAET-SWCNT-PABS is very stable whereas Au-DMAET-(SWCNT-PABS-*nano*FePc)$_1$ and Au-DMAET continue to show further decrease in peak current response upon subsequent scans. These results prove that Au-DMAET-SWCNT-PABS is

the best electrode and will therefore be used for the remaining electroanalytical studies in this section.

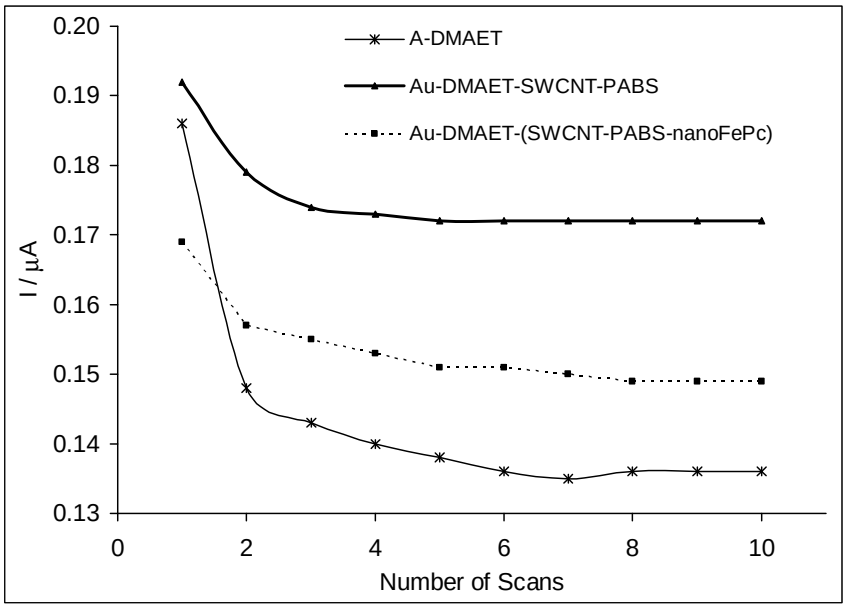

Figure 3.22: Plot of EP peak current (I_p) versus number of CV scans.

3.2.4.2 Rotating Disc Electrode Studies

Figure 3.23 shows the RDE data obtained at different rotating speeds (ω) for 10^{-5} M epinephrine electro-oxidation in phosphate buffer pH 7.4 using Au-DMAET-SWCNT-PABS. Figure 3.23 inset (a) shows the plot of limiting current (I_L) vs. $\omega^{1/2}$ (Koutecky-Levich plot) and (b) Tafel slope for the oxidation of epinephrine.

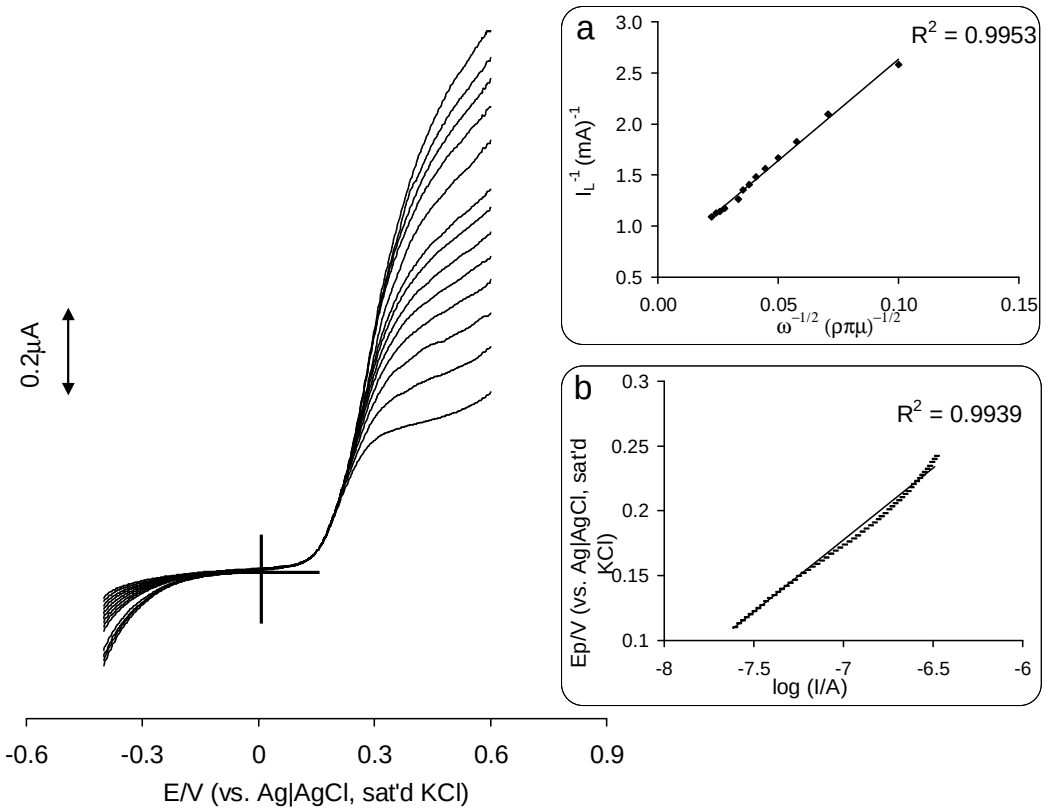

Figure 3.23: RDE voltammograms obtained at different rotating speed (ω) for 10^{-5} M epinephrine electro-oxidation in phosphate buffer pH 7.4 using Au-DMAET-SWCNT-PABS. Inset (a) shows the plot of I_L^{-1} versus $\omega^{-1/2}$ and (b) shows the Tafel slope for the oxidation of epinephrine from the RDE experiment. Scan rate = 50 mV s^{-1}.

The Koutecky-Levich plot was found to be linear with positive intercept; this indicates that the electrode reactions are controlled by both kinetics at the electrode surface and the mass transport of epinephrine species at the electrode surfaces. Using Equation 1.15 above the k_{ch} value obtained from the intercepts of the regression lines

was found to be $2.2x10^7$ $mol^{-1}cm^3s^{-1}$, a value much higher than that reported in literature [25]

Inset (b) in Figure 3.23 shows the plot of the Ep vs. the log of the kinetic current and the Tafel slope which represents the slope of this plot was approximately 70 mV dec^{-1} at all the potentials. Tafel slope value close to 60 mV dec^{-1} suggest a catalyst fast redox process as the first step followed by a non-redox (chemical step) rate-determining step (rds) such as analyte binding with the catalyst or possible deprotonation of the analyte [26,27] as a possible mechanism. The involvement of a chemical step in the rds is in agreement with the Koutecky-Levich plot which was found to be linear with positive intercept. The rate determining chemical step could be due to possible pi-pi interaction between SWCNT-PABS and EP molecule since CNTs are known for their ability to interact with organic aromatic compounds through pi-pi interaction and possibly also by hydrophobic interaction [28].

3.2.4.3 Chronoamperometric Analysis

Double potential step chronoamperometric experiments were recorded at the Au-DMAET, Au-DMAET-SWCNT-PABS and Au-DMAET-(SWCNT-PABS-*nano*FePc) by polarizing the potentials to 0.18 V and 0.0 V. Figure 3.24 shows well resolved double-step

chronoamperometric evolutions obtained at the Au-DMAET-SWCNT-PABS electrode in the absence (buffer alone) and presence of consecutive addition of 1 ml of 1 μM epinephrine in phosphate buffer.

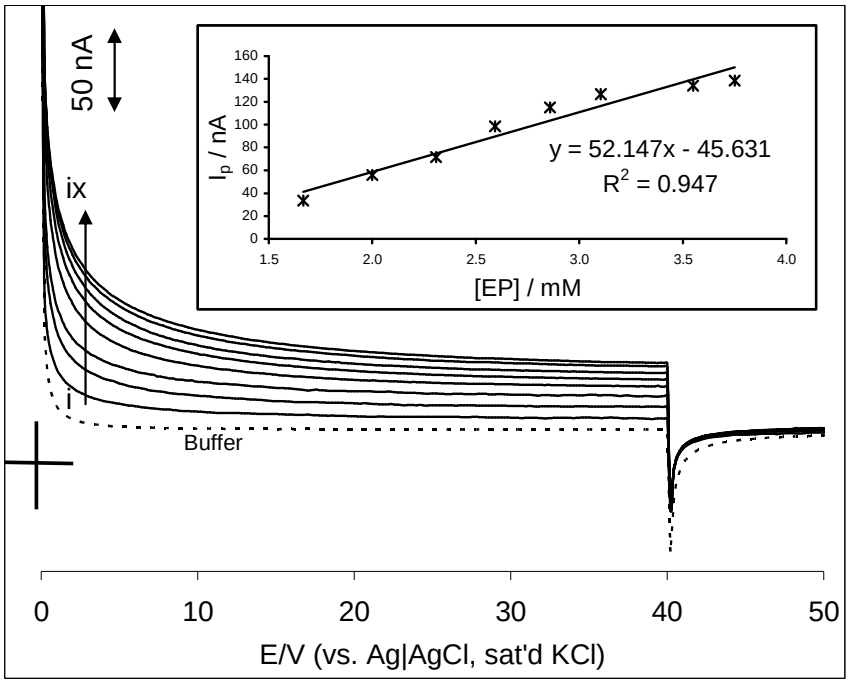

Figure 3.24: Typical double potential step chronoamperometric transients at Au-DMAET-SWCNT-PABS in PBS solution (pH 7.4) following addition of epinephrine. (i) to (ix) correspond to, 1.67, 2.00, 2.31, 2.59, 2.86, 3.10, 3.55, 3.75 μM, respectively. Inset shows the plot of chronoamperometric current at t = 1.6 s vs. [EP].

As previously shown the LoD and sensitivity were calculated from the linear relationship between transient catalytic current (measured at 1.6 s) and epinephrine concentrations. The LoD and sensitivity at Au-DMAET-SWCNT-PABS were calculated to be 3.35 x 10^{-7} M and 66.9 m AM^{-1} respectively. In order to investigate the real sample analysis

potential of the DMAET-SWCNT-PABS, the same experiment was carried out using a screen printed gold electrode (SPAuE); SPAuE is good for once off detection and ideal for real sample analysis. The LoD (4.52×10^{-7} M) value obtained is similar (within experimental error) to that obtained for Au-DMAET-SWCNT-PABS. When compared to presently available literature reports [29-37] on Au based electrodes towards the electrocatalytic detection of epinephrine (Table 3.2) it is observed that these results show comparable sensitivity and lower detection limits in some cases. Equations 1.13 and 1.14 were used as previously to calculate the diffusion coefficient (1.52×10^{-10} cm^2 s^{-1}) and catalytic rate constant (1.11×10^{7} M^{-1} s^{-1}) of epinephrine at constant concentration (at 10 μM in pH 7.4 PBS) poised at +180 mV versus Ag|AgCl. However, for this analyte n = 2 in the Cottrell equation (Eq. 1.13) as expected for the oxidation of epinephrine to epinephrinequinone [21,22,37].

Table 3.2: Comparative analytical data for the detection of epinephrine using electrochemical techniques.

Electrode[1]	**Analytical Parameter**				
	Electrolyte	**LCR**	**Sensitivity**	**LoD**	**Ref**
Au-DMAET-SWCNT-PABS	0.1 M PBS pH 7.4	3.3×10^{-8} – 1.4×10^{-7} M	66.9 m AM^{-1}	3.35×10^{-7} M	This work
SPAE-DMAET-SWCNT-PABS	0.1 M PBS pH 7.4	$4.22 – 3.57 \times 10^{-8}$ M	6.57 m AM^{-1}	4.52×10^{-7} M	This work
Au-DMAET-SWCNT-PABS/ FeTSPc	0.1 M PBS pH 7.4	$0.143 – 0.388 \times 10^{-6}$ M	2.45 m AM^{-1}	24×10^{-9} M	This work
Au-Cys-SWCNT	PBS, pH 7.0	Up to 130 μM	9.4×10^{-3} A M^{-1}	6×10^{-6} M	24
Au-DTT/DDT-*nano* Au	PBS, pH7.0	10^{-7} – 10^{-6} M, (10^{-5} – 2×10^{-4} M)	0.3261 μA μM^{-1}, (0.0233 μA μM^{-1})	60×10^{-9} M	22
Nano Au-ITO	0.1 M PBS pH 7.4	5×10^{-6} – 2×10^{-3} M	1.3199 μA mM^{-1}	1.8×10^{-6} M	29
Au-Cys-FeOCPc	PBS, pH 7.4	300 – 425 nM	0.53 m AM^{-1}	0.138×10^{-7} M	30

Au-Mascorbic Acid	PBS, pH 7.2	10^{-7} – 10^{-6} M, (10^{-5} – $2x10^{-4}$ M)		0.50 x 10^{-7}M	31
Au-Pen	PBS, pH 7.0	$5x10^{-7}$ – 10^{-6} M, (10^{-5} –$2x10^{-6}$ M)	0.0517 µA $µM^{-1}$, (0.0233 µA $µM^{-1}$)	0.1 x 10^{-6} M	32
Au-DMSA/PCA	PBS, pH 7.7	$5x10^{-6}$ – $8x10^{-4}$ M	0.00534 µA $µM^{-1}$	0.39 x 10^{-6} M (0.25 x 10^{-6} M)	33
Au-3MPA	PBS, pH 6.8	$2x10^{-7}$ – 10^{-6} M, ($1x10^{-6}$ – $5x10^{-4}$ M)	-	1.0 x 10^{-7} M	34
Au-LCys-FcAl	PBS, pH 7.4	$1.7x10^{-7}$ – 10^{-4} M	0.9202 µA $µM^{-1}$	0.18 x 10^{-7} M	35
Au-TA SBB	pH 4.4	10^{-7} – 10^{-5} M, (10^{-5} – $6x10^{-4}$ M)	0.083 A M^{-1}, (0.012 A M^{-1})	10 x 10^{-9} M	36

1. DTT/DDT: dithiothreitol/dodecanethiol, FeOCPc: iron octacarboxy phthalocyanine, SWCNT-CoTAPc: single-walled carbon nanotubes-cobalt(II)tetra-aminophthalocyanine, Mascorbic Acid: mercaptoacetic acid, Pen: penicillamine, DMSA/PCA: meso-2,3-dimercaptosuccinic acid/penicillamine, 3 MPA: 3-mercaptopropionic acid, LCys-FcAl: Lcysteine/aminylferrocene, TA: triazole. The values in parentheses were obtained at higher concentration ranges.

3.3 Colloidal Gold and Nanosized Iron (II) Phthalocyanine modified Gold Electrodes

Following the interesting LBL results seen in the previous section using *nano*FePc and SWCNT, I was curious to test the impact of the integration of *nano*FePc and colloidal gold (AuNP).

3.3.1 Layer-by-layer Self Assembly Process

The layer-by-layer assembly involving colloidal gold and *nano*FePc follows the similar fabrication process shown in Scheme 3.2. However, the SWCNT-PABS is obviously replaced by AuNP and four bilayers are used instead of five.

3.3.2 Atomic Force Microscopy

Figure 3.25 shows the topographic AFM images of (a) Au-DMAET and (b) Au-DMAET-AuNP, (c) Au-DMAET-(AuNP-*nano*FePc) and (d) Au-DMAET-(AuNP-*nano*FePc)$_4$. The AFM feature of the Au-DMAET has previously been discussed and added to Figure 3.25 merely for comparative reasons. Subsequent to the deposition of *nano*FePc onto the surface of the AuNP there is an increase in the topographic height as well as the mean roughness profile, indicating the change in surface morphology. Also, the base monolayer seen in Figure 3.25 (a) and (b) becomes less visible in Figure 3.25 (c) indicating a complete coverage

of *nano*FePc onto AuNP. Consequently in Figure 3.25 (d) the base monolayer can no longer be seen and the Au-DMAET-(AuNP-*nano*FePc)$_4$ the AFM feature can be described as a bunch of globular particles clumped together. The substantial growth in Figure 3.25 (d) is further confirmed by the dramatic increase in the root mean square deviation and maximum height of the roughness profiles. The grooves in some of the panels may indicate surfaces whose morphology was modified by the lateral movement of the tip.

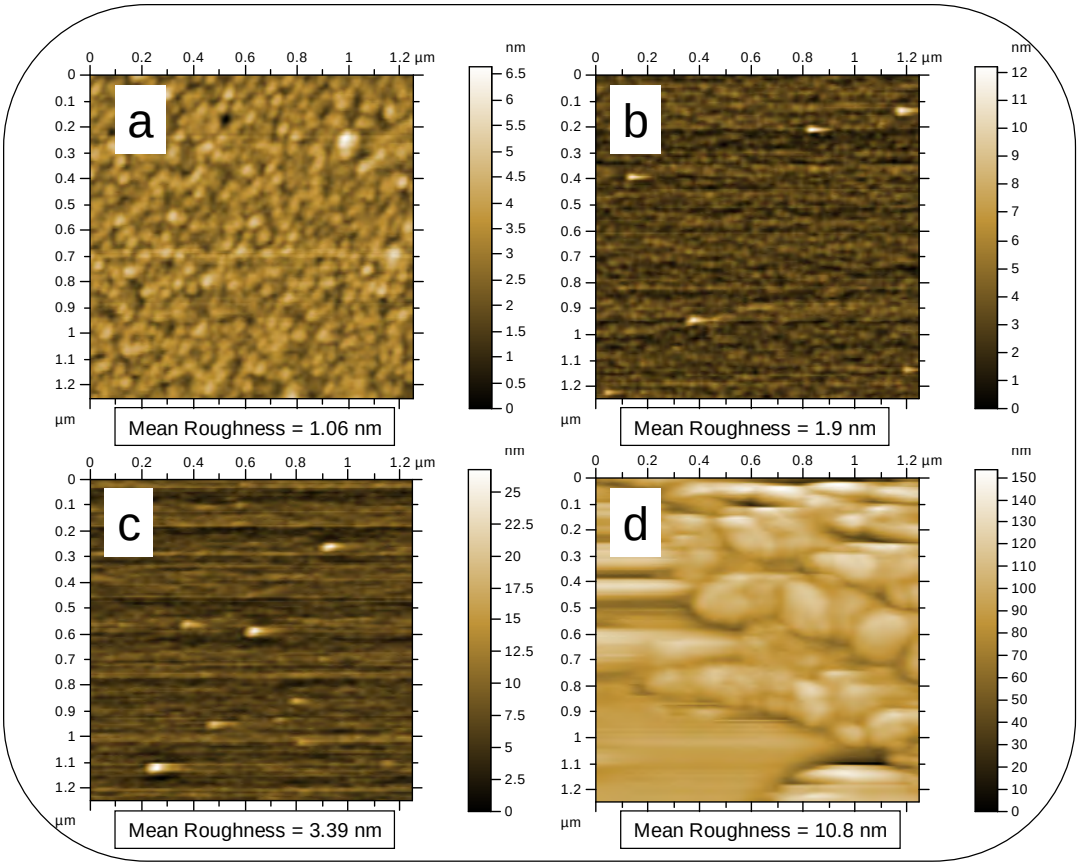

Figure 3.25: Topographic AFM images of (a) Au-DMAET and (b) Au-DMAET-AuNP, (c) Au-DMAET-(AuNP-*nano*FePc) and (d) Au-DMAET-(AuNP-*nano*FePc)$_4$.

3.3.3 Cyclic Voltammetry

Figure 3.26 shows the CV profiles of the (AuNP-*nano*FePc) individual bilayer assemblies in 0.1 M KCl containing equimolar mixture of $[Fe(CN)_6]^{3-}$/ $[Fe(CN)_6]^{/4-}$ solutions. The CV profiles of the layer-by-layer build up illustrated in Figure 3.26 shows the electrode's ability to impede and promote electron transport in $[Fe(CN)_6]^{4-/-3}$ solution. The electron transport ability of the electrode was impeded or blocked following the attachment of AuNP to *nano*FePc. This is not surprising considering gold nanoparticle films can behave as conducting or insulating material depending on the size and mutual distance of the metal cores. [38a] However, phthalocyanines are well known for their excellent electrocatalytic abilities [14,15] and this can be seen from the CVs in Figure 3.26 (b –d) where the electrodes electron transport ability is increased subsequent to the attachment of *nano*FePc onto AuNP at each bilayer.

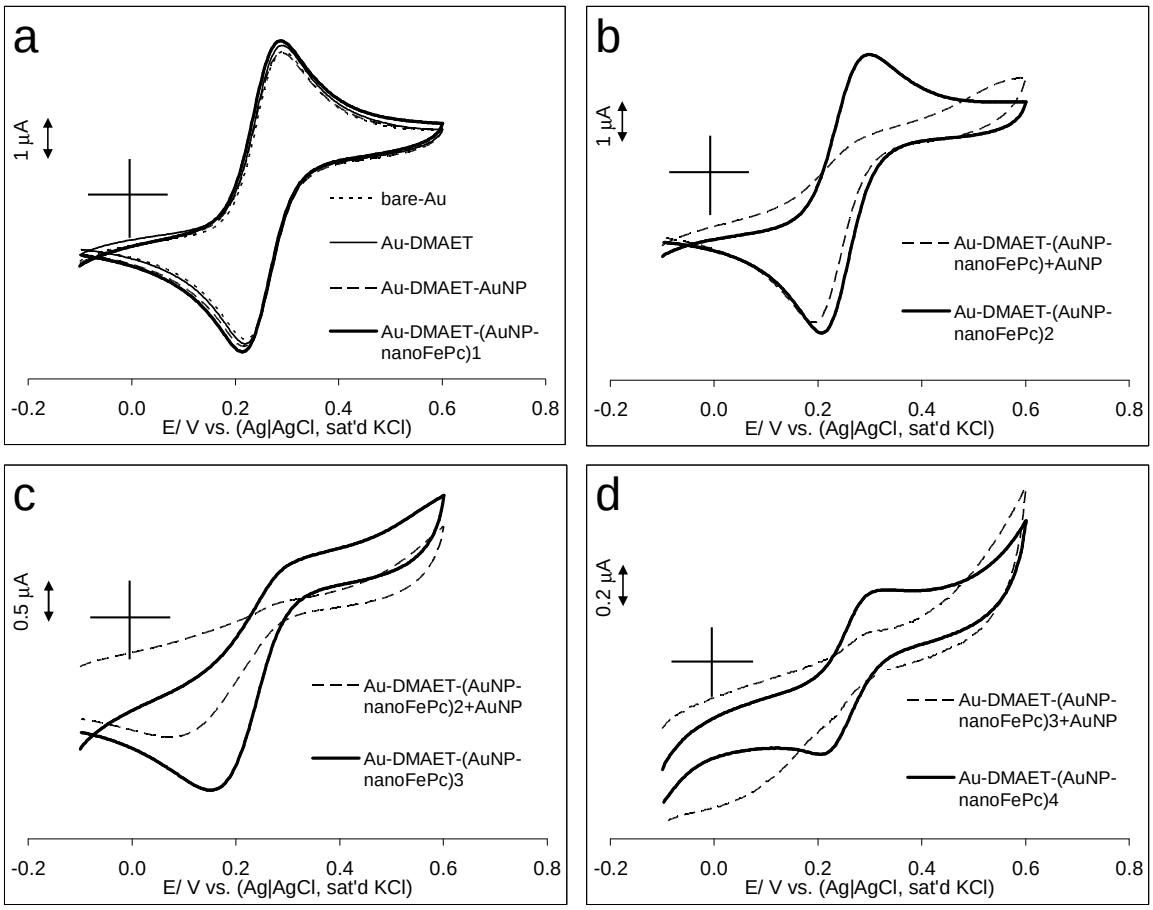

Figure 3.26: Typical CV profiles of (a) bare-Au, Au-DMAET, Au-DMAET-AuNP and Au-DMAET-(AuNP-*nano*FePc)$_1$, (b) 2nd Bilayer, (c) 3rd Bilayer and (d) 4th Bilayer assemblies in 0.1 M KCl containing equimolar mixture of $[Fe(CN)_6]^{3-}$/ $[Fe(CN)_6]^{4-}$ solutions at a scan rate of 25 mV s^{-1}.

The AuNP acts as an insulator that slows down the electron transfer rate between the electrode and the AuNP. Contrastingly, Bethell *et al.* [38b] showed that the thiol layer restricts the electrodes ability while the gold clusters deposited onto the thiol layers promotes the electrode. Although the *nano*FePc promoted the electrode, the

current was not restored to the previous current response. Also, the peak-to-peak separation potential (ΔE_p) increases from the first to fourth bilayer. Therefore, the rate of electron transport is the fastest at the first bilayer since it decreases with increasing (ΔE_p). The blocking of the electrode by the AuNP can be attributed to the repulsive interaction between the negative charges of the AuNP and negative redox probe. The nanoFePc is positively charged and therefore attracts the negatively charged $[Fe(CN)_6]^{-4/-3}$, thus promoting the electrode, resulting in an increased current response compared to the AuNP. It should be noted that this was not observed in the previous section involving negatively charged SWCNT-PABS and positively charged *nano*FePc possibly because the SWCNT acts as nanowires and readily accommodate the electrons movement along the tube.

3.3.4 Electrochemical Impedance Spectroscopy

The nyquist plots shown in Figure 3.27 for the bare-Au, Au-DMAET, Au-DMAET-AuNP, Au-DMAET-(AuNP-*nano*FePc)$_1$, Au-DMAET-(AuNP-*nano*FePc)$_1$+ AuNP and Au-DMAET-(AuNP-*nano*FePc)$_2$ satisfactorily fitted (in terms of low percent errors obtained after several iterations) the modified Randles equivalent circuit (Fig. 1.8a). The charge transfer resistance was only measured up until the 3rd bilayer since additional bilayers resulted in scattered points. The

nyquist plot of the 3rd bilayer was omitted in Figure 3.27 for clarity. However, the R_{ct} values for all the bilayers were included in the bar graph illustrated in Figure 3.28. The charge transfer resistance values showed the same trend for the rate of electron transport as the ΔE_p values showed in cyclic voltammetry; where the attachment of AuNP increases the resistance to flow of electrons while the attachment of *nano*FePc reduces the resistance.

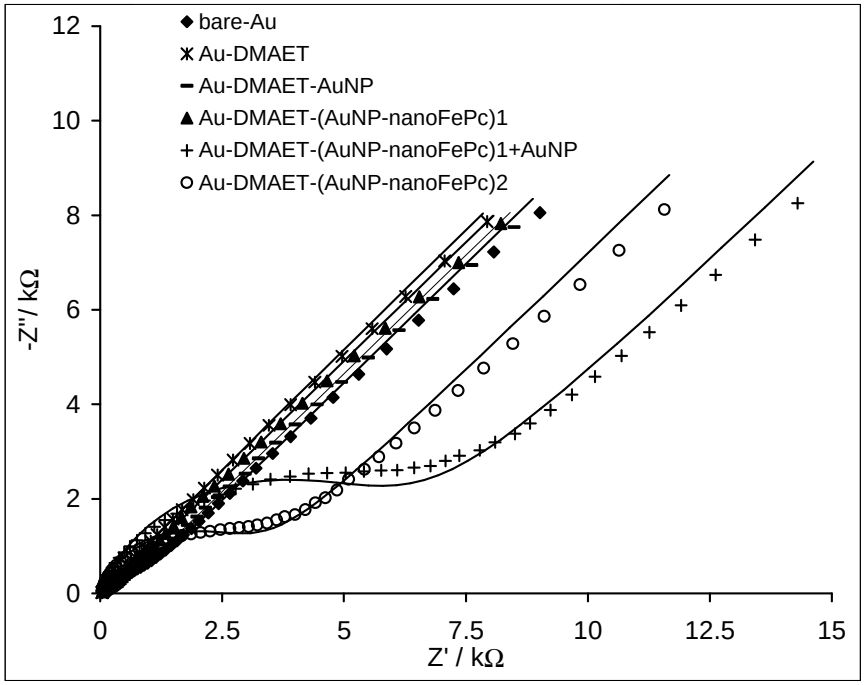

Figure 3.27: Nyquist plots for the bare-Au, Au-DMAET, Au-DMAET-AuNP, Au-DMAET-(AuNP-*nano*FePc)$_1$, Au-DMAET-(AuNP-*nano*FePc)$_1$+AuNP and Au-DMAET-(AuNP-*nano*FePc)$_2$. Successive bilayers were omitted for clarity.

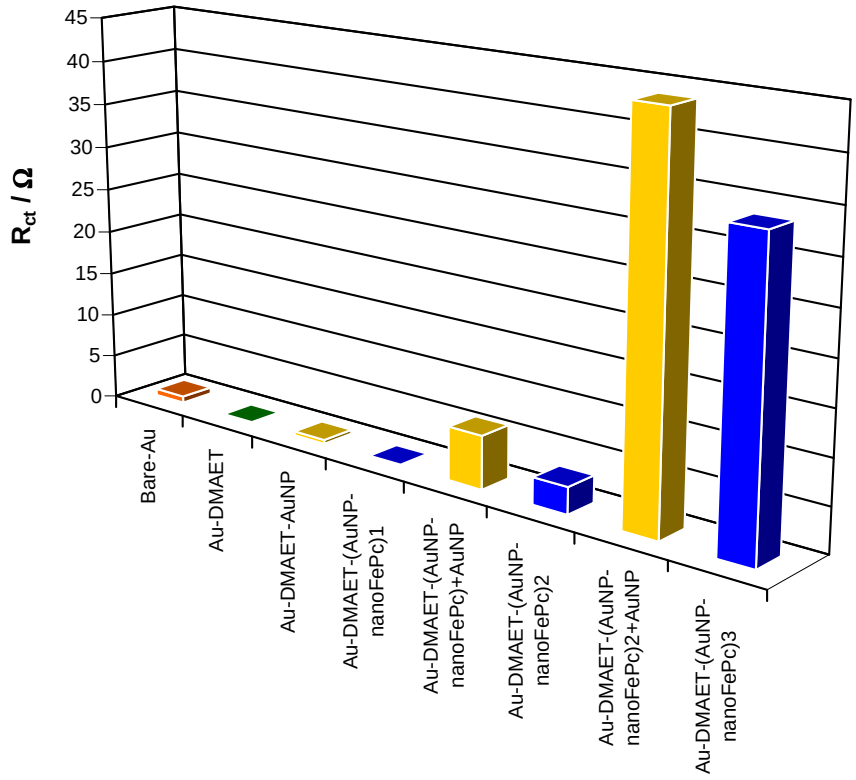

Figure 3.28: 3-D Bar graph representing the R_{ct} values of the bare-Au, Au-DMAET, Au-DMAET-AuNP and the underlying bilayers.

3.3.5 Electrochemical Response towards H_2O_2

The electrode was further tested at each bilayer to determine its ability as a potential sensor towards H_2O_2 detection in physiological pH conditions (pH 7.4). Figure 3.29 compares the reduction current responses of 1 mM H_2O_2 in PBS (pH 7.4) at increasing bilayers (*nano*FePc being the exposed layer). From CV profiles in Figure 3.29 it can be seen that the current response decrease upon increasing bilayers. A similar trend is observed when AuNP is represented as the outer most layer (*nano*FePc-AuNP). Therefore, Au-DMAET-(AuNP-

*nano*FePc)$_1$ is the best electrode in terms of current response for the detection of H_2O_2.

In general, increasing number of bilayers decrease electron transport and voltammetric response of H_2O_2.

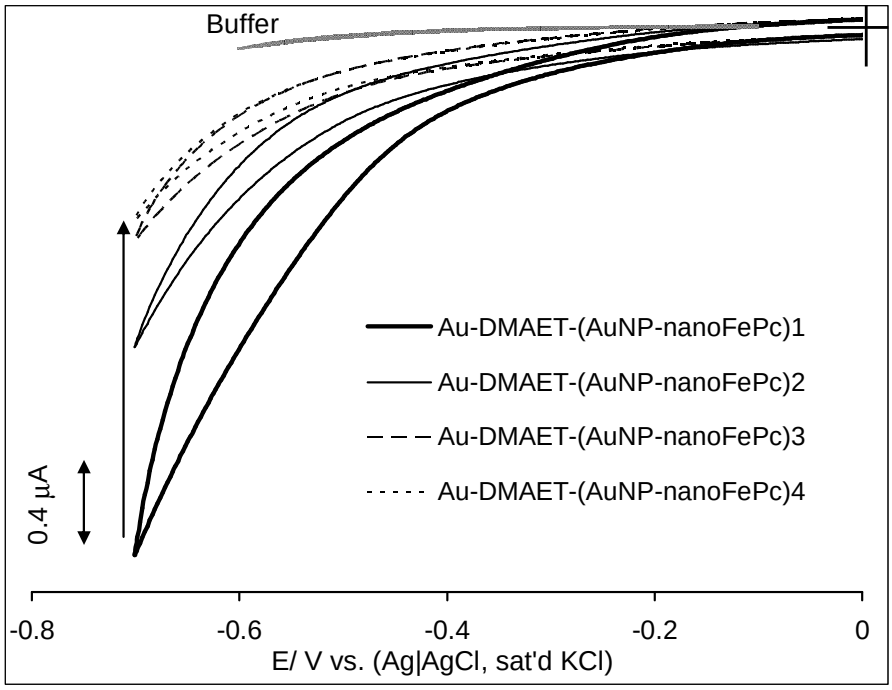

Figure 3.29: Typical CV profiles showing the impact of increasing (a) bilayers (*nano*FePc being the exposed layer) on the current response of 1 mM H_2O_2 in PBS (pH 7.4). Scan rate: 25 mV s^{-1}.

3.4 Single Walled Carbon Nanotubes and Iron (II) Tetrasulphophthalocyanine Modified Gold Electrodes

Following the use of positively charged phthalocyanine, I was now curious to learn the impact if any, of negatively charged phthalocyanine in particular the water-soluble iron (II) tetrasulfophtalocyanine (FeTSPc). However, due to the similar charges of SWCNT-PABS and FeTSPc, I formed a hybrid mixture (SWCNT/FeTSPc) of the two. As a result of their individual competitiveness for the positively charged base monolayer I had to ensure complete coverage of the base gold electrode. Therefore, longer deposition times (~36 h) and slightly higher concentration (5 mM) of DMAET were employed.

3.4.1 Electrode Self Assembly Process

Scheme 3.3 represents the self-assembly fabrication of the various electrodes via strong electrostatic interaction between the positively-charged DMAET and the negatively-charged FeTSPc and SWCNT-PABS species.

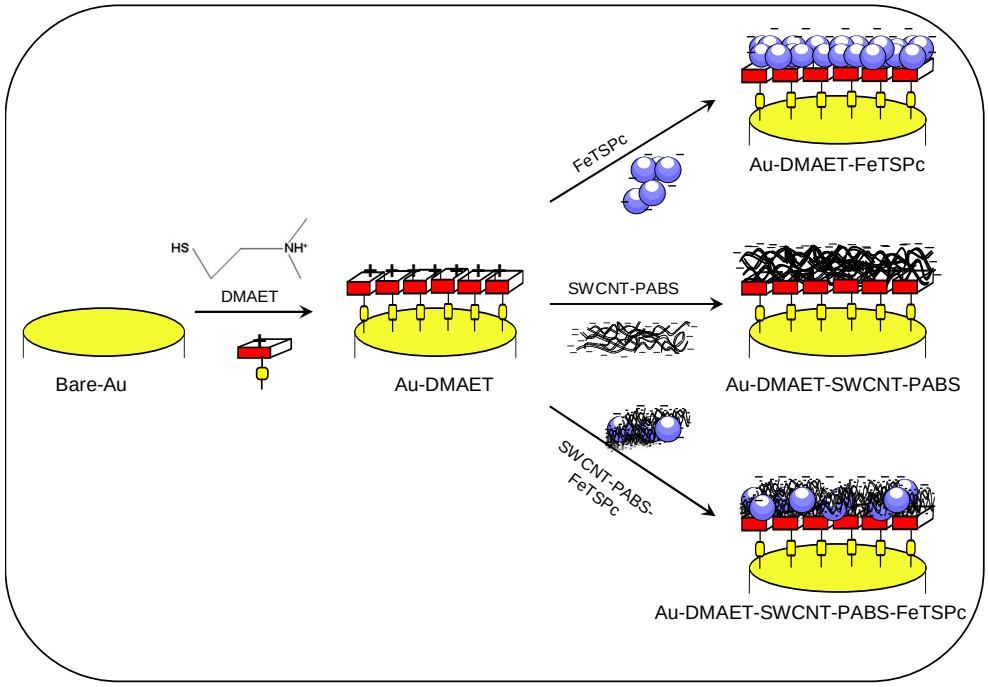

Scheme 3.3: Schematic representation showing the fabrication route for Au-DMAET-FeTSPc, Au-DMAET-SWCNT-PABS and Au-DMAET-SWCNT-PABS/FeTSPc.

3.4.2 Characterization

3.4.2.1 Atomic Force Microscopy

The build-up and formation of the films on gold plates were confirmed using AFM. The AFM images of bare-Au, Au-DMAET and Au-DMAET-SWCNT-PABS have been identified earlier as previously stated. However, since 5 mM DMAET was used in this experiment, Figure 3.30 represents the topographic AFM images of (a) Au-DMAET, (b) Au-DMAET-FeTSPc, (c) Au-DMAET-SWCNT-PABS, (d) Au-DMAET-SWCNT-PABS/FeTSPc. The Au-DMAET depicted in Figure 3.25 (a) shows increased roughness and height profiles than the Au-DMAET discussed

above. This could be as a result of the higher depostion times and increased concentrations of DMAET used.

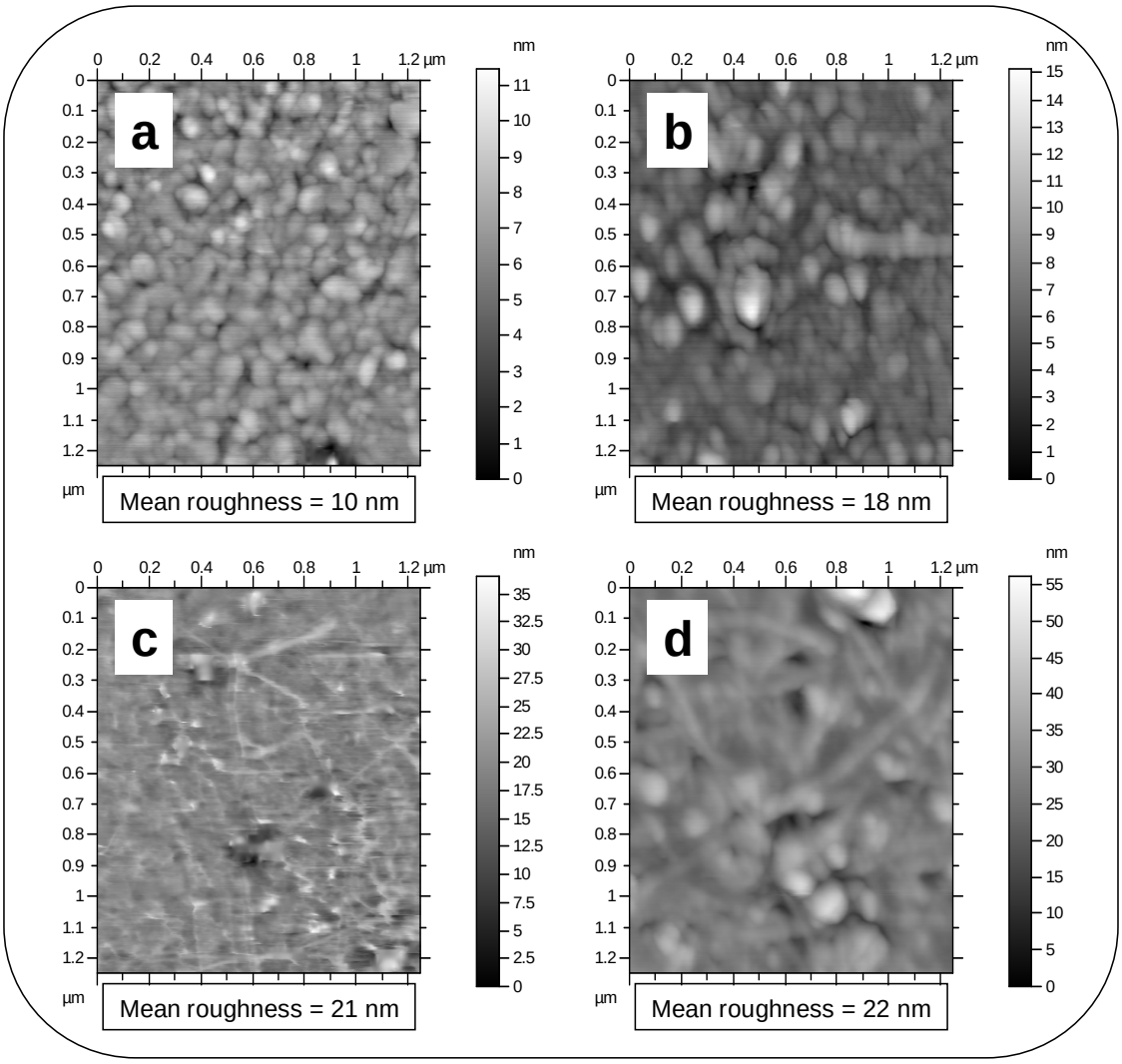

Figure 3.30: Topographic AFM images of (a) Au-DMAET, (b) Au-DMAET-FeTSPc, (c) Au-DMAET-SWCNT-PABS, (d) Au-DMAET-SWCNT-PABS/FeTSPc.

The presence of flat lying tubes is clearly visible in Figure 3.25 (c). Furthermore, there is an increase in root mean square (R_q) and height roughness (R_z) profiles compared to that of Au-DMAET. Upon

immobilization of Au-DMAET with FeTSPc, there is clear evidence of growth judging by (i) the bigger globular-like features on the image (Fig. 3.30b) which can be attributed to the FeTSPc aggregates, and (ii) increase in both R_q and R_z. The AFM features in Figure 3.30 clearly show the immobilization of both FeTSPc and SWCNT-PABS on Au-DMAET judging by mixed tubular and globular features of the images in an irregular arrangement. In addition, the R_q and R_z increased yet again.

3.4.2.2 Cyclic Voltammetry in Aqueous (pH 7.4) Conditions

Figure 3.31 compares the cyclic voltammograms of Au-DMAET, Au-DMAET-SWCNT-PABS, Au-DMAET-FeTSPc and Au-DMAET-SWCNT-PABS/FeTSPc in PBS (pH 7.4) recorded at 50 mV s^{-1}.

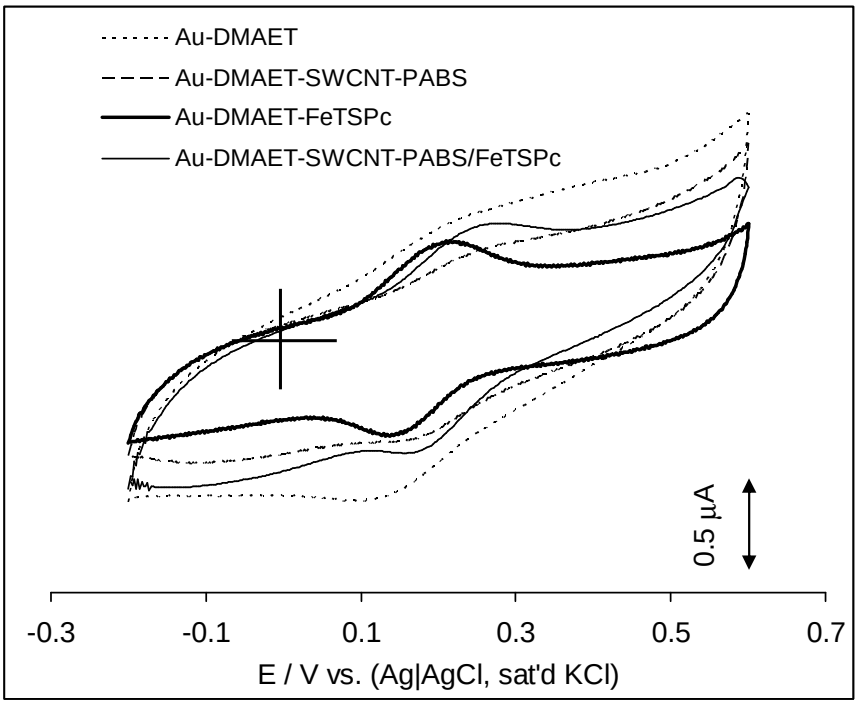

Figure 3.31: Comparative cyclic voltammograms in phosphate buffer pH 7.4 solutions obtained at Au-DMAET, Au-DMAET-SWCNT-PABS, Au-DMAET-FeTSPc and Au-DMAET- SWCNT-PABS/FeTSPc. Scan rate = 50 mV s^{-1}.

The weak reversible process shown by the Au-DMAET is attributed to the electric-field driven protonation/deprotonation process described earlier. It should be pointed out here that the CV of Au-DMAET is well-defined only when less deposition time (≤ 24 h) and/or slightly lower concentration of DMAET (< 5 mM) is used in the fabrication as observed earlier. Both Au-DMAET-FeTSPc and Au-DMAET-SWCNT-PABS/FeTSPc showed well-defined reversible peaks, attributed to the Fe^{2+}/Fe^{3+} redox processes [39]. The ratio of the anodic and cathodic

peak current densities (I_{pa}/I_{pc}) are approximately equal, indicating electrochemical reversibility.

Figure 3.32 (a) and (b) shows the cyclic voltammograms obtained at different scan rates (25 – 1000 $mV.s^{-1}$ range) in phosphate buffer pH 7.4 solution obtained at (a) Au-DMAET-FeTSPc and (b) Au-DMAET-SWCNT-PABS/FeTSPc respectively. The formal potentials ($E_{1/2} = [E_{pa} + E_{pc}]/2$) of Au-DMAET-FeTSPc and Au-DMAET-SWCNT-PABS/FeTSPc are 170 and 220 mV, respectively. Ideally, at small scan rates, the peak-to-peak potential separation ($\Delta E_p = |E_{pa} - E_{pc}|$) in a monolayer should be zero. However, the ΔE_p values for the Au-DMAET-FeTSPc and Au-DMAET-SWCNT-PABS/FeTSPc are 78 and 112 mV, respectively. The electron transport (signified by the magnitude ΔE_p) is fastest at the Au-DMAET-FeTSPc and Au-DMAET-SWCNT-PABS/FeTSPc. Also, the width at half the peak current (E_{fwhm} / mV) slightly deviates from the ideal value of 90.6/n mV for n = 1 [40-42], where, the Au-DMAET-FeTSPc and Au-DMAET-SWCNT-PABS/FeTSPc are 122 and 127 mV, respectively. The deviation of the ΔE_p and E_{fwhm} from their ideal values is typical of redox species being in located in different environments with different formal potentials [43-45]. Thus, it may be said that the FeTSPc molecules are located at different environments with different formal potentials. Simply stated, the FeTSPc species have different formal potentials when immobilized at the DMAET and/or SWCNT-

PABS, and thus the effective voltammetric wave consists of a superposition of distinct electrochemical responses, resulting in the observed non-ideal voltammograms. In all cases, the electrochemical parameters of the DMAET-FeTSPc are slightly better than those recorded for the SWCNT-PABS/FeTSPc, which can be attributed to the different environments and complexities of the SWCNT-PABS platform.

At higher scan rates where the voltammetry is controlled by the rate of electron transport, the ΔE_p increases with scan rates. The plots of the peak currents (I_p) against the scan rate (v) are shown in Figure 3.32 (c), where Figure 3.32 (c) i-iv are respectively the I_a for SWCNT-PABS/FeTSPc, I_a for DMAET-FeTSPc, I_c for DMAET-FeTSPc and I_c for SWCNT-PABS/FeTSPc versus scan rate (v). The plots are all linear which is characteristic of surface-confined redox species.

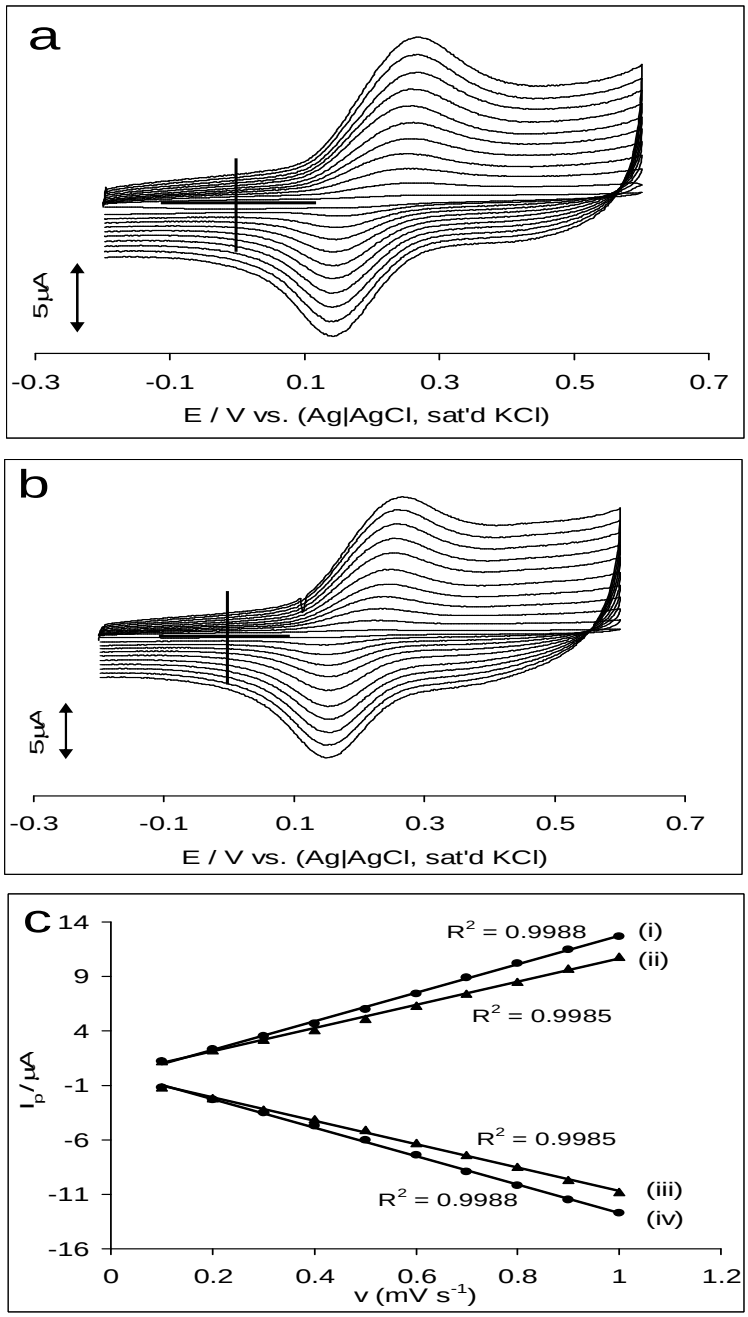

Figure 3.32: Cyclic voltammograms obtained at different scan rates (25 – 1000 mV s^{-1} range) in phosphate buffer pH 7.4 solution obtained at (a) Au-DMAET-FeTSPc; (b) Au-DMAET- SWCNT-PABS/FeTSPc and (c) Plots of I_p vs. v for I_a for (i) SWCNT-PABS/FeTSPc, (ii) I_a for DMAET-FeTSPc, (iii) I_c for DMAET-FeTSPc and (iv) I_c for SWCNT-PABS/FeTSPc.

3.4.2.3 Surface Coverage

The surface coverage (Γ/ mol cm^{-2}) of the FeTSPc at both (Au-DMAET and Au-DMAET-SWCNT-PABS) platforms were established from the slopes of the plots according to Equation 3.5 [39]:

$$I_p = \frac{n^2F^2A\Gamma\nu}{4RT} \qquad 3.5$$

where n = number of electrons involved in the redox process, F is the Faraday constant, and A is the area of the electrode, R is the ideal gas constant and T is the ideal temperature (K). The surface coverage was calculated to be (4.14 ± 0.21) x 10^{-8} mol cm^{-2} using the average slope values from both the I_a and I_c vs. ν plots for Au-DMAET-FeTSPc and (4.08 ± 0.28) x 10^{-8} mol cm^{-2} for Au-DMAET-SWCNT-PABS/FeTSPc. The estimated values indicate multilayer coverage rather than monolayers expected to be (for MPc molecules) in the ~ 10^{-10} mol cm^{-2} [46,47].

3.4.2.4 Stability Studies

The electrochemical stability of the Au-DMAET-FeTSPc and Au-DMAET-SWCNT-PABS/FeTSPc was conducted by repetitively scanning each electrode in PBS (pH 7.4). Figure 3.33 (a) shows the repetitive cycling of Au-DMAET-FeTSPc and Figure 3.33 (b) compares the CVs of the freshly prepared Au-DMAET-FeTSPc and Au-DMAET-FeTSPc after

one week of use in PBS. It can be seen from the repetitive cycling (Fig. 3.33a) as well as the comparative CVs (Fig. 3.33b) that in terms of I_p and E_p, there is so significant changes in CV patterns. The Au-DMAET-SWCNT-PABS/FeTSPc (not shown) showed a similar stability profile to that of the Au-DMAET-FeTSPc. Such remarkable stability is important for their electrochemical studies as well as their potential applications in aqueous conditions. This result is significant for the fact that FeTSPc is highly soluble in water but upon attachment to Au-DMAET film, there is a strong bond by electrostatic attraction between SO_3^- of FeTSPc and $NH^+(CH_3)_2$ of DMAET, and this bond is stable even when the electrode is used in aqueous media.

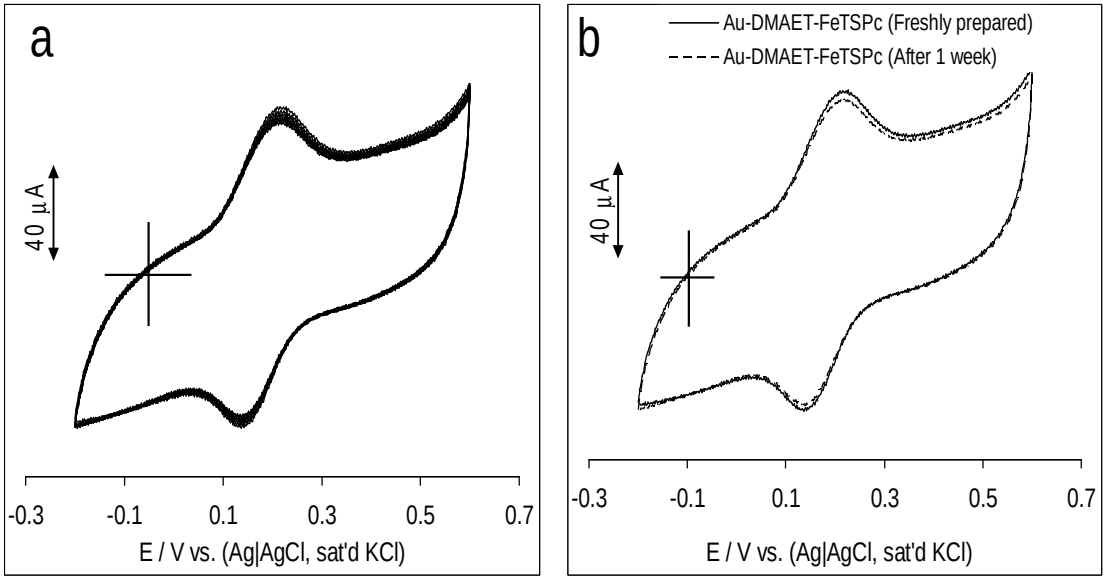

Figure 3.33: (a) Repetitive cyclic voltammograms obtained in PBS (pH 7.4) at Au-DMAET-FeTSPc and (b) CVs obtained at freshly prepared Au-DMAET-FeTSPc and a week later after use.

3.4.2.5 Cyclic Voltammetric Evolutions in $[Fe(CN)_6]^{3-/4-}$

Next, the extent to which the modifying species permit the electron transfer of the $[Fe(CN)_6]^{4-}/[Fe(CN)_6]^{3-}$ redox probe to the underlying gold electrode was investigated. From Figure 3.34 it can be seen that with the exception of the Au-DMAET-SWCNT-PABS/FeTSPc which showed the highest anodic and cathodic peak currents, the CV responses of the electrodes otherwise were essentially the same in terms of (i) peak-to-peak separation potential ($\Delta E_p \approx 70$ mV vs. Ag|AgCl, sat'd KCl), and (ii) the equilibrium potential ($E_{1/2} \approx 0.25$ V vs. Ag|AgCl, sat'd KCl).

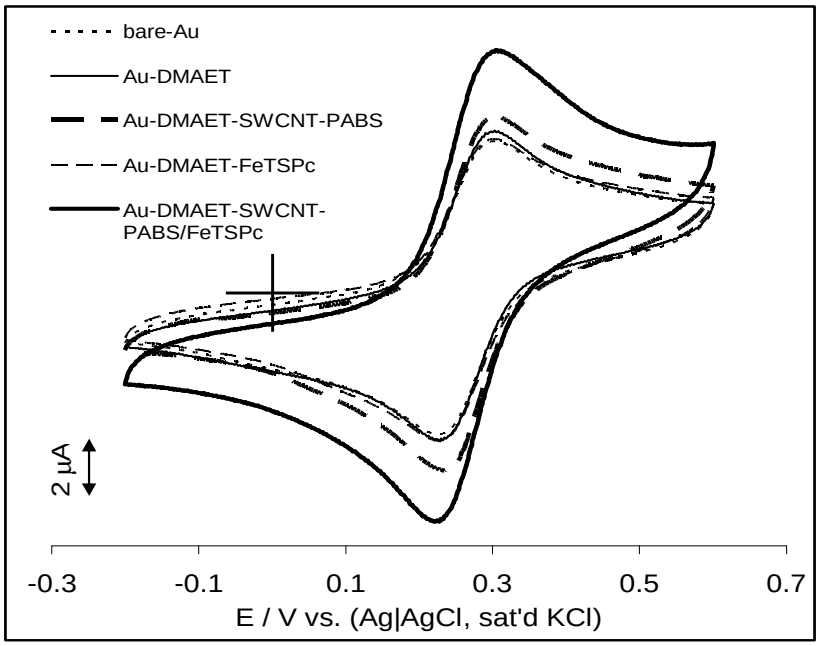

Figure 3.34: Cyclic voltammograms obtained in 1 mM $Fe(CN)_6^{3-/4-}$ in 0.1 M KCl at bare-Au, Au-DMAET, Au-DMAET-SWCNT-PABS, Au-DMAET-FeTSPc and Au-DMAET- SWCNT-PABS/FeTSPc.

3.4.2.6 Impedimetric Studies in $[Fe(CN)_6]^{3-/4-}$

For further understanding of the electronic behaviour of the electrodes, EIS studies were carried out in $[Fe(CN)_6]^{3-/4-}$ solution at the equilibrium potential of the redox couple ($E_{1/2} \approx 0.25$ V). Figure 3.35 (a) compares the nyquist plots of bare-Au, Au-DMAET, Au-DMAET-SWCNT-PABS, Au-DMAET-FeTSPc and Au-DMAET-SWCNT-PABS/ FeTSPc.

The bare gold electrode was satisfactorily fitted using the modified Randles' equivalent circuits (Fig. 1.8a). However, attempts to fit the modified electrodes with the ideal or modified Randles circuit or a simple one-reaction RC time constant circuit were unsuccessful as they led to very large fitting error values. The longer deposition times and slightly higher concentration of DMAET are believed to be reasons for the Au-DMAET and Au-DMAET-SWCNT-PABS not fitting the modified Randles' equivalent circuits as previously shown. The observed experimental data for Au-DMAET, Au-DMAET-SWCNT-PABS, Au-DMAET-FeTSPc and Au-DMAET-SWCNT-PABS/FeTSPc were satisfactorily fitted (judged by the low values of relative % errors in Table 3.3) with the electrical equivalent circuit two voigt RC element (Fig. 3.35b) involving solution resistance (R_s), double-layer capacitance (C_{dl}), electron-transfer resistance (R_{ct}) and CPE.

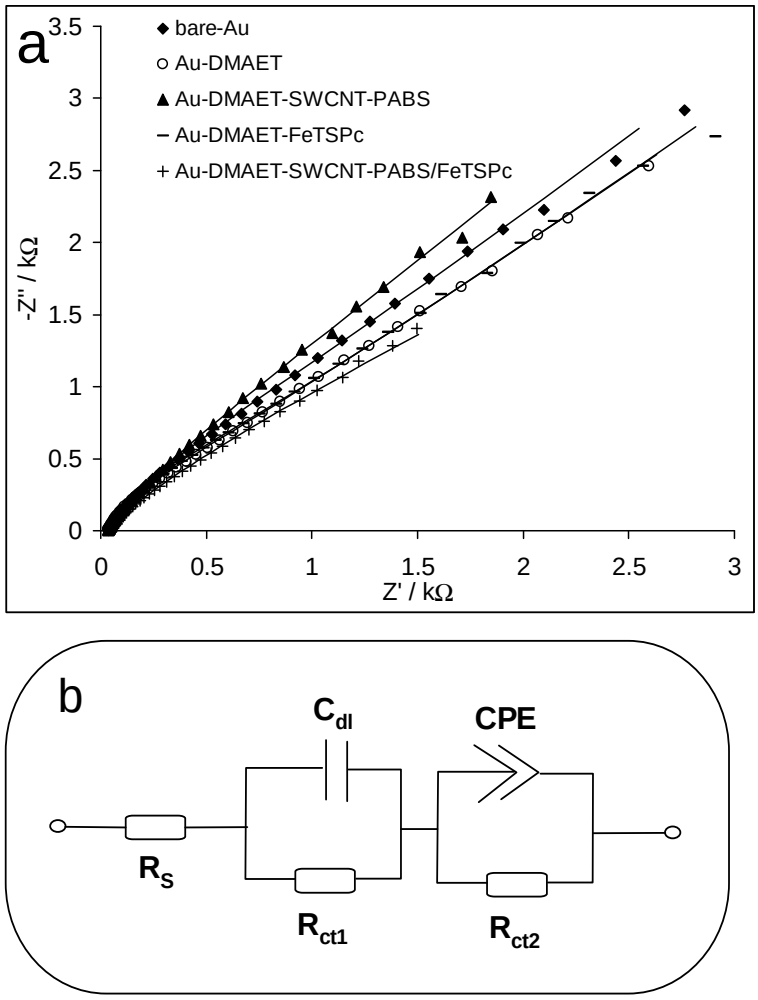

Figure 3.35: (a) Nyquist plots obtained in $Fe(CN)_6^{3-/4-}$ 0.1 M KCl at (i) bare-Au, (ii) Au-DMAET, (iii) Au-DMAET-SWCNT-PABS, (iv) Au-DMAET-FeTSPc and (v) Au-DMAET- SWCNT-PABS/FeTSPc and (b) the equivalent circuits used for fitting (ii) – (iv). Figure 1.8 (a) was used to fit (i).

The apparent electron transfer rate constant (k_{app}) values of the electrodes were obtained from the equation [48.49]:

$$k_{app} \approx k^o = \frac{RT}{n^2 F^2 A R_p C} \qquad 3.6$$

where n is the number of electron transferred (1), C is the concentration of the $[Fe(CN)_6]^{3-}$ (in mol cm^{-3}, the concentration of $[Fe(CN)_6]^{3-}$ and $[Fe(CN)_6]^{4-}$ are equal), A is the experimentally-determined area of the electrode, R_p is obtained by the series connection of the two charge-transfer resistances (i.e., $R_p = R_{ct1} + R_{ct2}$).

The following features shown by the impedimetric data of the modified electrodes should be emphasized. First, from data in Table 3.3, the Au-DMAET-SWCNT-PABS/FeTSPc gave the highest k_{app} value, indicating that charge-transfer processes between the $[Fe(CN)_6]^{3-/4-}$ and the underlying gold surface are made a lot easier by the synergistic combination of the FeTSPc and SWCNT-PABS. The reason for this is not fully understood but may be related to such factors as the high surface area of the SWCNT-PABS that permits diffusion of the redox probe as well as its ability to act as efficient electric conducting nanowires.

Second, equivalent circuit models suggesting physico-electrochemical phenomena involving more than one RC time constants, as seen from the circuit model (Fig. 3.35b), are mainly due to multiple or coupled reaction sequences, to roughening of the electrode, and to frequency-dependent ohmic resistances caused by non-uniform charging of the electrode/electrolyte double layer. The

impedance of CPE is defined by Equation 1.18. As mentioned above the capacitive nature of CPE can be deduced by the magnitude of n. Table 3.3 shows n ≥ 0.70, indicating pseudocapacitive behaviour. Also, from the bode plots (Fig. 3.36a) of log |Z| vs. log f the slopes are approximately similar (*ca*. –0.60) at the mid frequency region, indicative of pseudocapacitive behaviour.

Third, impedance spectra are known to contain features that could be directly related to microstructures, with the grain boundary phases of microstructures having a dominant blocking effect on the impedance spectra [50,51]. Since electron transport processes occurring via permeation of the redox probe through the spaces created by the assembled species is expected to be faster than that arising through the layers [52], the first Voigt element (R_{ct1}/C_{dl}) may be associated to the polarization phenomenon due to electron transfer occurring through the layers of the molecules and/or the grain boundaries, while the second voigt element (R_{ct2}/CPE) to processes that occur through the spaces amongst the self-assembled molecular layers.

Finally, an attempt to replace the ideal C_{dl} with a CPE (a real application situation) in the modelling circuit proved unsuccessful. The explanation of this observation may be found from the relationship between C_{dl} and CPE. It has been elegantly described by Orazem and Tribollet [51], that frequency dispersion leading to CPE behaviour occurs

as a result of distribution of time constants along either the area of the electrode surface (involving a 2-dimensional aspect of the electrode) or along the axis normal to the electrode surface (involving a 3-dimensional surface). A 2-D distribution presents itself as an ideal RC behaviour, meaning that impedance measurements are very useful in distinguishing whether the observed global CPE behaviour is due to a 2-D or 3-D distribution or both. Thus, the observed impedimetric behaviour seen at the modified electrodes likely involves 2-D and 3-D distributions. Also, note that despite the fitting of the spectra with ideal RC element (1st Voigt element), the phase angles seen on the Bode plots (i.e., –phase angle (θ) vs. log f, (Fig. 3.36b) are in the range of 48 - 56^{o}, which are less than the 90^{o} expected of an ideal capacitive behaviour, thus further confirming presence of the 2-D distribution arising from CPE behaviour and the pseudocapacitive nature of the modified electrodes.

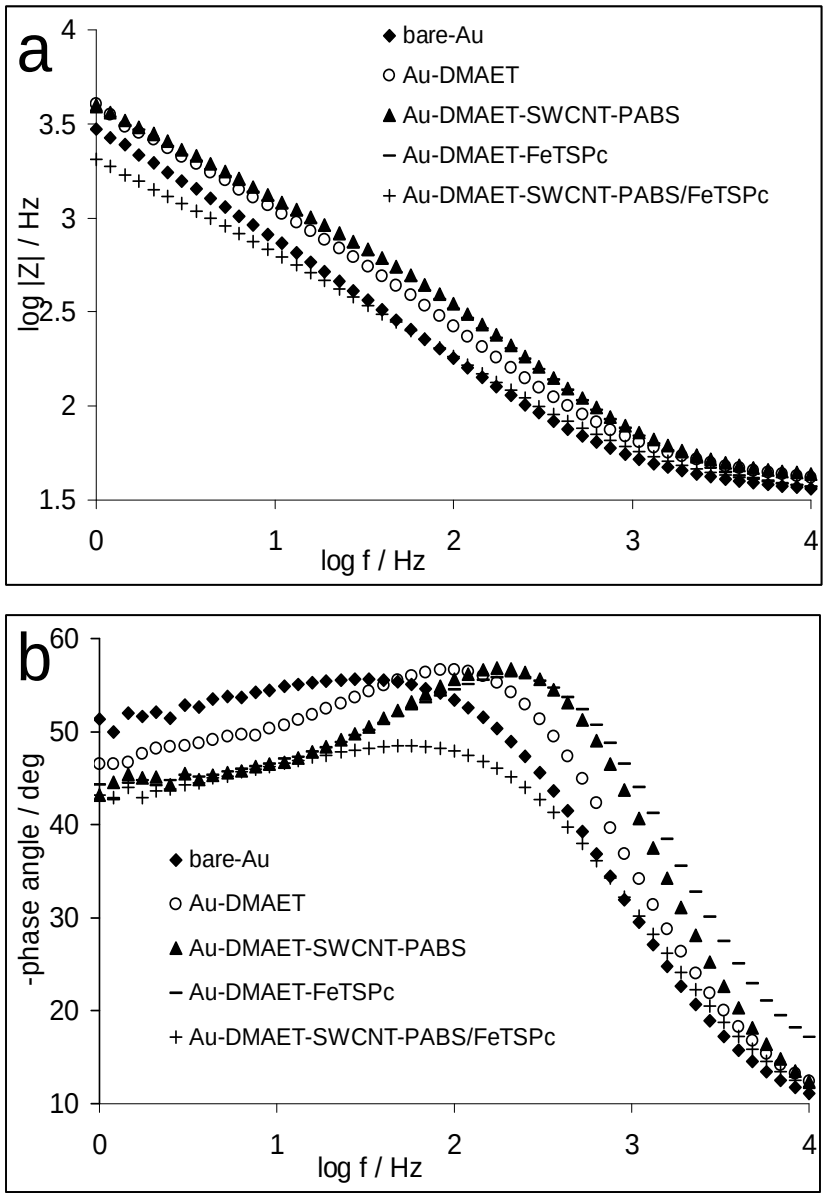

Figure 3.36: Bode plots of (a) log |Z| vs. log f and (b) -Phase angle vs. log f obtained in $Fe(CN)_6^{3-/4-}$ 0.1 M KCl at bare-Au, Au-DMAET, Au-DMAET-SWCNT-PABS, Au-DMAET-FeTSPc and Au-DMAET- SWCNT-PABS/FeTSPc.

Table 3.3: Comparative EIS paprameter data obtained for Au-DMAET, Au-DMAET-SWCNT-PABS, Au-DMAET-FeTSPc and Au-DMAET-SWCNT-PABS/FeTSPc.

Electrochemical impedance parameters[1]	**Electrode[2]**			
	Au-DMAET	**Au-DMAET-SWCNT-PABS**	**Au-DMAET-FeTSPc**	**Au-DMAET- SWCNT-PABS/FeTSPc**
R_s / Ω cm^2	0.98 (1.06)	0.99 (1.93)	0.78 (2.24)	0.81 (1.19)
R_{ct1} / kΩ cm^2	0.16 (4.62)	0.15 (5.77)	0.13 (5.93)	0.07 (8.22)
C_{dl} / µF cm^{-2}	1.22 (3.31)	1.05 (4.19)	1.17 (4.65)	3.36 (7.05)
R_{ct2} / kΩ cm^2	0.041 (4.38)	0.038 (4.89)	0.038 (5.42)	0.037 (7.09)
CPE / µF cm^{-2}	0.94 (3.02)	0.58 (5.40)	0.75 (5.18)	2.44 (3.05)
n	0.75 (0.60)	0.77 (0.99)	0.74 (0.97)	0.65 (0.71)
10^3 k_{app} / cm s^{-1}	1.32 ± 0.08	1.44 ± 0.10	1.54 ± 0.11	2.30 ± 0.22

1. Value in parenthesis is the estimated percent errors in fitting the experimental impedance spectra.

2. Bare gold electrode was fitted with the modified Randles equivalent circuit (Fig. 7b(i)) with estimated values of R_s ≈ 2.8 Ωcm^2, R_{ct} ≈ 15 Ω cm^2, Z_w ≈ 2 x 10^{-6} Ω cm^2, CPE ≈ 21 µF cm^{-2}, n ≈ 0.9 and k_{app} ≈ 18x10^{-3} cm s^{-1}. Estimated percent fitting errors ≤ 4%

3.4.3 Electrocatalytic Detection of Epinephrine

Electrocatalytic detection of EP was used to test the ability of the surface-confined FeTSPc to detect biologically significant analytes. Figure 3.37 compares cyclic voltammetric evolutions of 10^{-5} M EP in phosphate buffer solution (pH 7.4) at bare-Au, Au-DMAET-FeTSPc and Au-DMAET-SWCNT-PABS/FeTSPc.

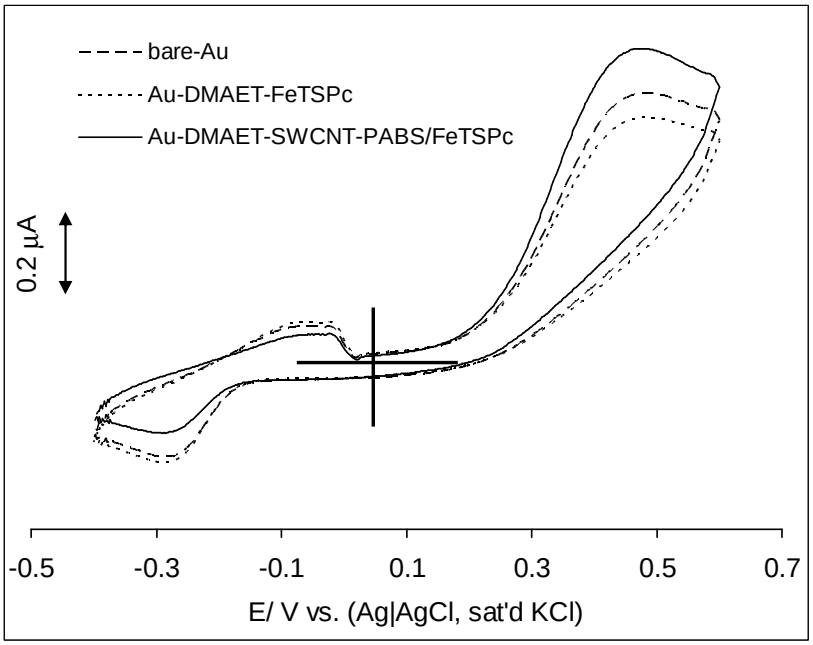

Figure 3.37: Cyclic voltammograms obtained at bare-Au, Au-DMAET-FeTSPc and Au-DMAET-SWCNT-PABS/FeTSPc in 10^{-4} M EP PBS (pH 7.4) Scan rate = 50 mV s^{-1}.

The relatively enhanced current response at the Au-DMAET-SWCNT-PABS/FeTSPc compared to Au-DMAET-FeTSPc is attributed to synergic properties arising from the co-existence of FeTSPc and

SWCNT-PABS. Hence, Au-DMAET-SWCNT-PABS/FeTSPc was further used for chronoamperometric detection of EP.

Double potential step chronoamperometric experiments were recorded at Au-DMAET-SWCNT-PABS/FeTSPc by polarizing the potentials to 0.35 V and 0.0 V. Figure 3.38 shows a well-resolved double-step chronoamperometric evolutions obtained in the absence (buffer alone) and presence of consecutive addition of 1 ml of 1 μM epinephrine in phosphate buffer solution (pH 7.4) to 20 ml phosphate buffer. Figure 3.38 (inset) clearly shows the corresponding plot of transient catalytic current (measured at 4 s) and epinephrine concentrations, a linear relationship (R^2 = 0.990) was obtained. The sensitivity of the plot of transient catalytic current (measured at 4 s) and epinephrine concentrations was found to be 2.45 AM^{-1}. The limit of detection was calculated to be 24 nM. From equations 1.12 and 1.13 the diffusion coefficient, D, and the catalytic rate constant, k, of 10 μM epinephrine in phosphate buffer (pH 7.4) were calculated to be 22.4 x 10^{-3} cm^2 s^{-1} and 5.49 x 10^6 M^{-1} s^{-1} respectively. For reasons previously mentioned n = 2 in the Cottrell equation.

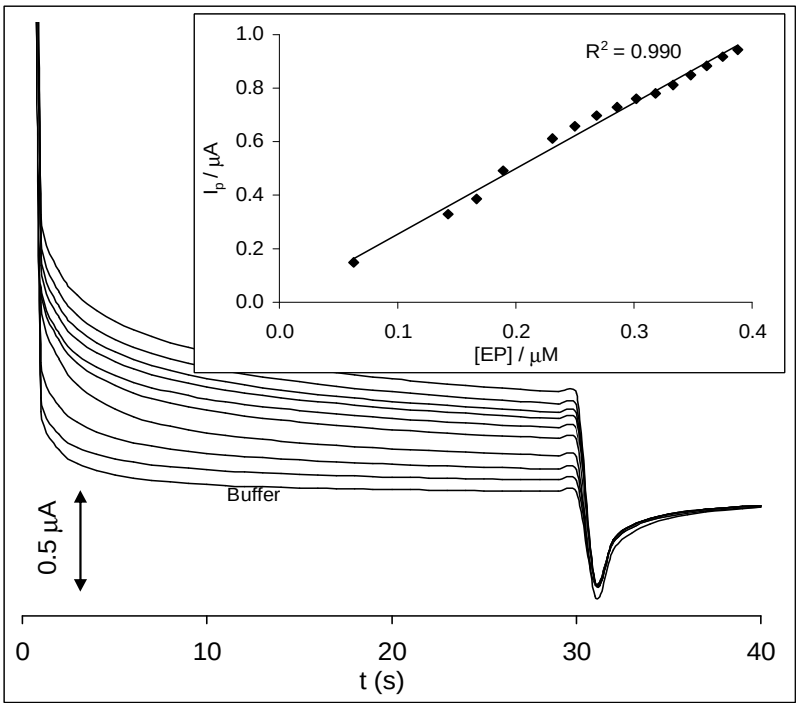

Figure 3.38: Typical double potential step chronoamperometric transients obtained for epinephrine electro-oxidation at Au-DMAET-SWCNT-PABS/FeTSPc. Inset: Plot of I_p vs. [EP] in phosphate buffer pH 7.4; 0.143, 0.167, 0.211, 0.231, 0.268, 0.302, 0.333, 0.362 and 0.388 µM are the concentrations from outer to inner. Inset shows the plot of chronoamperometric current at t = 1.6 s vs. [EP].

3.5 Monolayer-Protected Clusters of Gold Nanoparticles modified Gold Electrodes

The final part of this dissertation investigates the impact of different ratios of the protecting –OH and –COOH based monolayer ligands of redox-active gold nanoparticles on the dynamics of electron transport between solution species, in organic and aqueous media, and the electrode surface. The popular electrostatic self-assembly strategy technique was used for the immobilisation of MPCAuNPs onto the gold electrode. [53-59]. Considering the low concentration (~ 15 x 10^{-10} mol L^{-1}) of the MPCAuNPs, longer period adsorption (18 h) was adopted to allow for the electrostatic integration of the MPCAuNPs with the positively-charged DMAET SAM (Scheme 3.4). To my knowledge, this is the first time this type of architecture involving different ratios of carboxylated and hydroxyl containing ligands is fabricated and described.

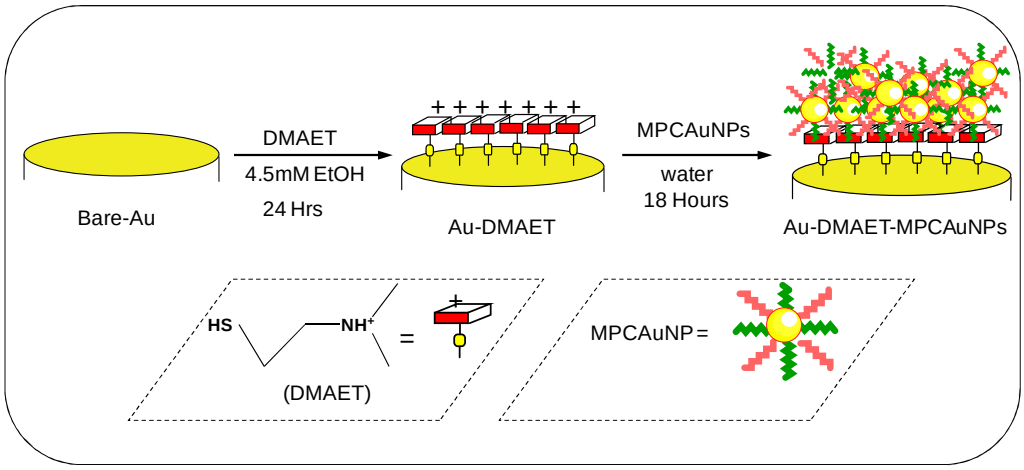

Scheme 3.4: Schematic of the self-assembly process via electrostatic interaction between the positively-charged DMAET monolayer and the negatively-charged monolayer-protected clusters of gold nanoparticles.

3.5.1 Spectroscopic and Microscopic Characterization

The preparation of the MPCAuNPs (summarized in Scheme 1.2) was adopted from the previous work by Tshikudo *et al.* [60]. The PEG-stabilized MPCAuNPs are extremely stable in the water. They can be centrifuged, dried and re-suspended in aqueous solution without any loss of materials. Unlike their citrate-stabilised counterpart that changed colour from red to colourless solution after about 2 months storage, the PEG-stabilised MPCAuNPs have not shown any detectable change in their ruby-red solutions even after 8 months. Also, unlike most other hydrosols, the PEG-stabilized MPCAuNPs do not show any detectable aggregation in 2 M NaCl solution. Their size is similar to their precursor citrate-stabilized gold nanoparticles (14±1 nm) as

confirmed by their TEM images, exemplified in Figure 3.39 with MPCAuNP-$COOH_{99\%}$.

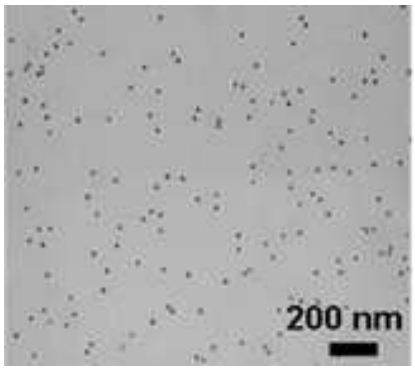

Figure 3.39: Typical TEM image of Au-DMAET-MPCAuNP-$COOH_{99\%}$.

Figure 3.40 shows the comparative 3-D AFM images of the bare-Au, Au-DMAET, Au-DMAET-MPCAuNP-$COOH_{50\%}$ and Au-DMAET-MPCAuNP-$COOH_{99\%}$.

As previously mentioned for an ultra thin film monolayer, there is very little difference between the thickness of bare-Au and Au-DMAET [1] which is also identified from the very small change in their roughness root mean square deviation (rms) values. However integration with the PEG-stabilized MPCAuNPs, the topographic heights increased to ~ 5 nm (with roughness factor of ~2.2 nm) for the Au-DMAET-MPCAuNP-$COOH_{1\%}$ (not shown), ~ 8 nm (with roughness factor of ~2.9 nm) for the Au-DMAET-MPCAuNP-$COOH_{50\%}$ and to about 10 nm (with roughness factor of ~3.2 nm) for the Au-DMAET-MPCAuNP-$COOH_{99\%}$. There is a slight increase in the topographic

height subsequent to adsorption of PEG-stabilized MPCAuNPs which may be attributed to the chain length of the ligands. The PEG-stabilized MPCAuNPs assembled as bundles with needle-like protrusions, presumably due to the strong van der Waal's attractive forces existing between carbon chains. In general, all the PEG-Stabilized MPCAuNPs show similar surface morphology.

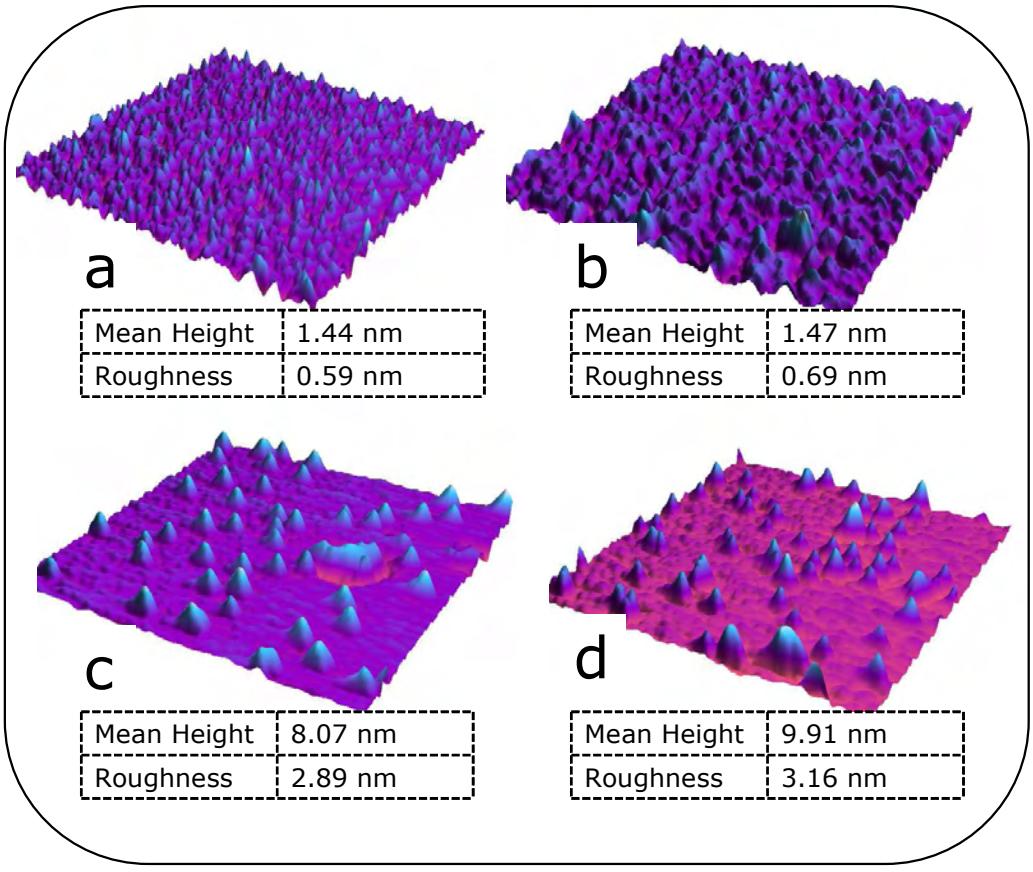

Figure 3.40: Typical 3-D AFM images of (a) bare-Au, (b) Au-DMAET, (c) Au-DMAET-MPCAuNP-$COOH_{50\%}$ and (d) Au-DMAET-MPCAuNP-$COOH_{99\%}$.

3.5.2 Cyclic Voltammetric Evolution and Electron Transfer in Non-Aqueous Solution

Figure 3.41 (a) shows the CV profiles of bare-Au, Au-DMAET, Au-DMAET-MPCAuNP-$COOH_{1\%}$, Au-DMAET-MPCAuNP-$COOH_{50\%}$ and Au-DMAET-MPCAuNP-$COOH_{99\%}$ in CH_2Cl_2 containing 0.1 M tetra-*n*-butylammonium perchlorate (TBAP). Some well-defined voltammetric peaks are observed in the potential range of –0.8 and +1.1 V (vs. AgCl). The activities in the negative potential region (0.0 to –0.8 V) may be attributed to the presence of the DMAET molecule since the bare gold electrode is the only electrode that shows no peak at -0.45 V. For clarity, the voltammetric evolutions in the positive potential region (0.0 to +1.1 V) are shown for the activities of the Au-DMAET-MPCAuNP-$COOH_{1\%}$ (Fig. 3.41b), Au-DMAET-MPCAuNP-$COOH_{50\%}$ (Fig. 3.41c) and Au-DMAET-MPCAuNP-$COOH_{99\%}$ (Fig. 3.41d).

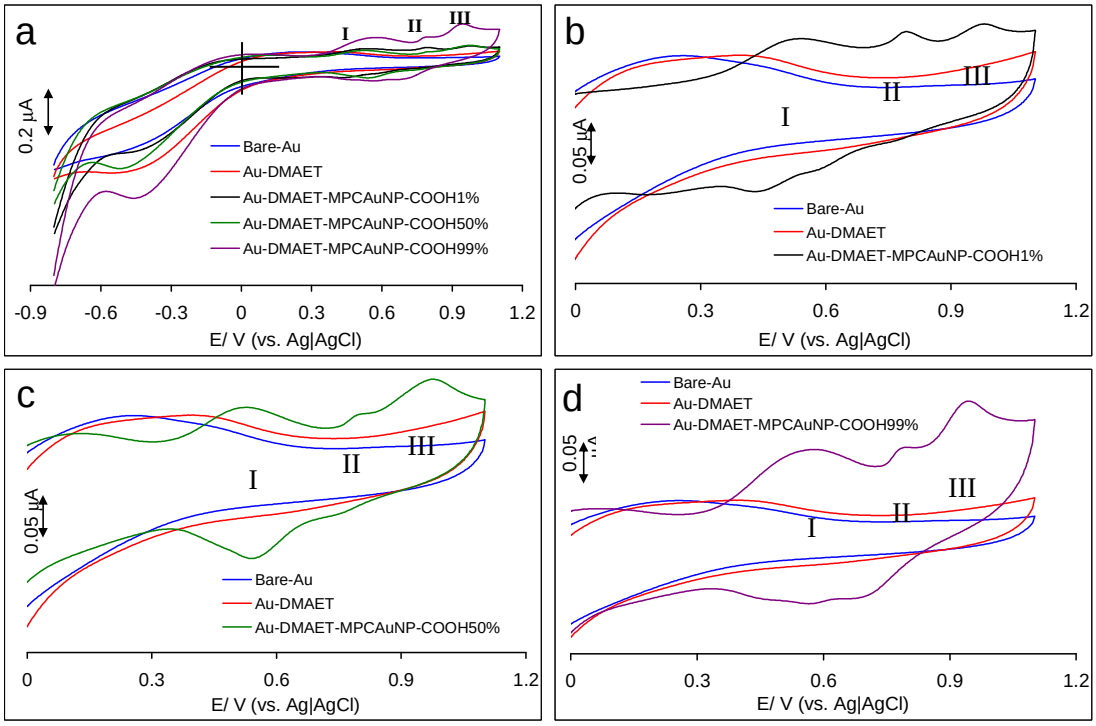

Figure 3.41: (a) Cyclic voltammograms of bare-Au, Au-DMAET, Au-DMAET-MPCAuNP-$COOH_{1\%}$, Au-DMAET-MPCAuNP-$COOH_{50\%}$ and Au-DMAET-MPCAuNP-$COOH_{99\%}$ in CH_2Cl_2 containing 0.1M TBAP at a scan rate of 25mV/s. The amplified area between 0 – 1.2 V (vs. Ag|AgCl) of Au-DMAET-MPCAuNP-$COOH_{1\%}$, Au-DMAET-MPCAuNP-$COOH_{50\%}$ and Au-DMAET-MPCAuNP-$COOH_{99\%}$ are exemplified in b, c and d respectively.

All the three PEG-stabilized MPCAuNP exhibit three well-defined redox processes at equilibrium potential ($E_{1/2} \approx 0.53$, 0.78 and 0.96 V vs. AgCl wire). From previous works on ligand-protected gold nanoparticles [61-63], these redox processes may be ascribed to the discrete charging of the adsorbed particle double layers [64,65]. The observation of the discretized double-layer charging is dependent on the nanoparticle potential change (ΔV) incurred upon a single electron

transfer to/from the working electrode or any other electron-donor/acceptor. ΔV is the space between any two neighbouring peak voltages. These nanoparticles are usually described as 'quantum capacitors', with their stored-charge potentials changing by values that are easily seen upon single-electron transfers. From Figure 3.41, it can be seen that the charging peak around 0.5 V (**I**) appeared broad for all three electrodes, suggesting the occurrence of a two-electron transfer process arising from two close ΔVs. In fact, a closer look at the scan rate studies, exemplified for the Au-DMAET-MPCAuNP-$COOH_{1\%}$ (Fig. 3.42a) and Au-DMAET-MPCAuNP-$COOH_{99\%}$ (Fig. 3.42b), clearly prove that the broad peak at the **I** is two peaks. Thus, the two close peaks are assigned to $MPC^{1+/0}$ and $MPC^{2+/1+}$, while processes **II** and **III** may be ascribed to the $MPC^{3+/2+}$ and $MPC^{4+/3+}$, respectively.

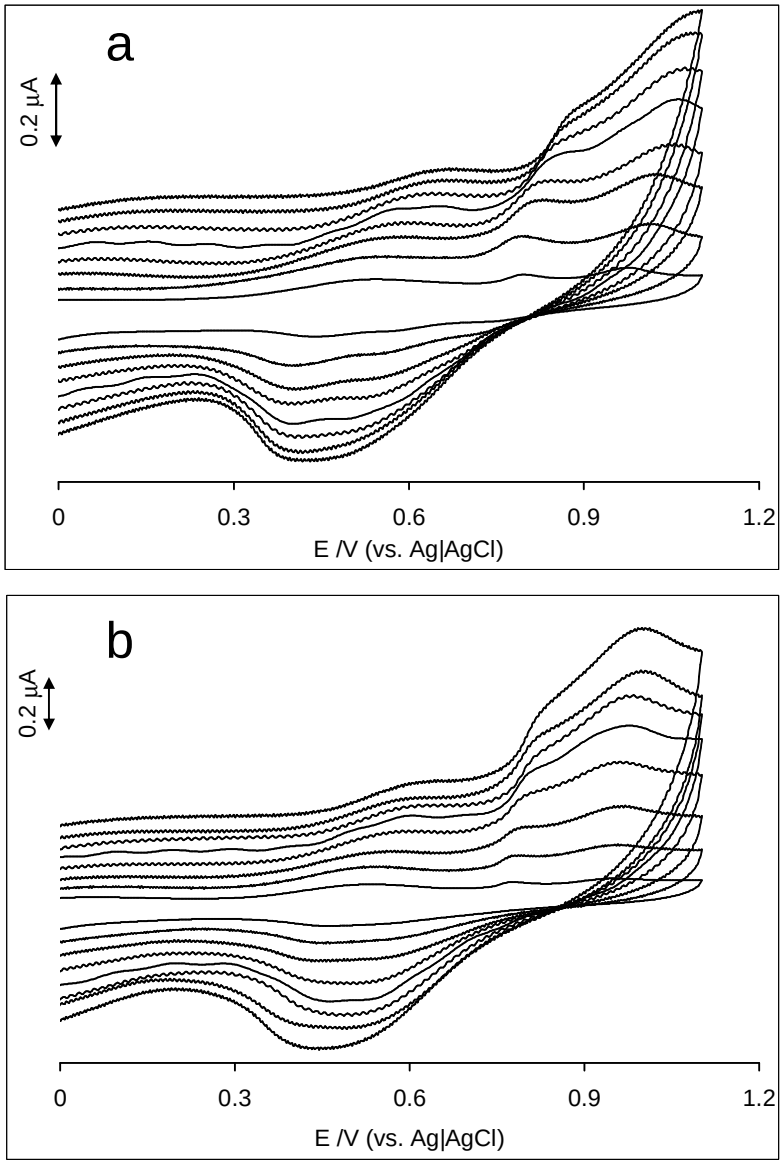

Figure 3.42: Scan rate studies at (a) Au-DMAET-MPCAuNP-$COOH_{1\%}$ (25 mV – 200 mV) and (b) Au-DMAET-MPCAuNP-$COOH_{99\%}$ (25 mV – 300 mV).

Electrochemical impedance spectroscopy represents a crucial technique for probing the heterogeneous electron transfer kinetics at gold electrodes modified with self-assembled MPCAuNPs. EIS

experiments were carried out for each of the modified electrodes. Figure 3.43 presents typical comparative Nyquist plots obtained for the three modified electrodes, based at different potentials (~0.53, 0.78 and 0.96 V vs. Ag|AgCl). The experimental data were satisfactorily fitted with the modified Randles electrical equivalent circuit (Fig. 3.39).

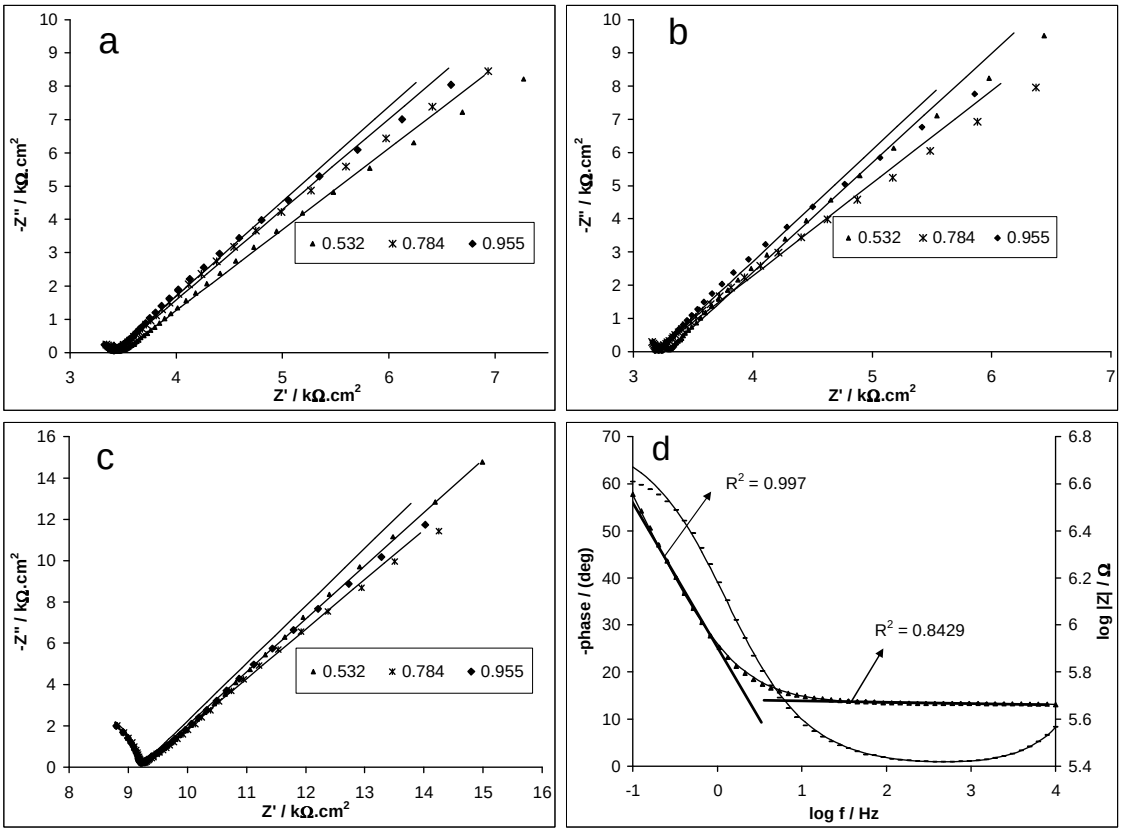

Figure 3.43: (a-c) Nyquist plots resulting from Au-DMAET-MPCAuNP-$COOH_{1\%}$, Au-DMAET-MPCAuNP-$COOH_{50\%}$ and Au-DMAET-MPCAuNP-$COOH_{99\%}$ respectively, in CH_2Cl_2 containing 0.1 M TBAP. (d) Typical bode plot of Au-DMAET-MPCAuNP-$COOH_{99\%}$ in the same solution.

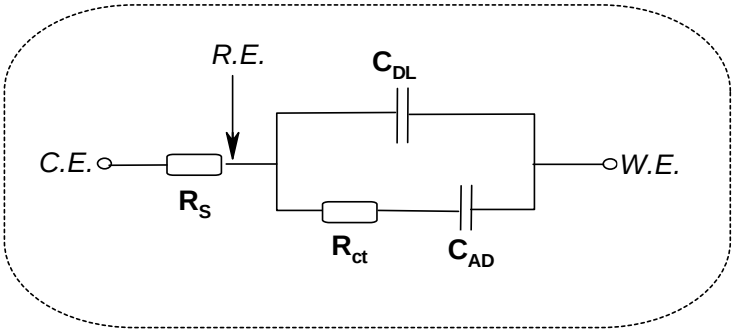

Figure 3.44: Modified Randles electrical equivalent circuit.

In the model, the R_s is the solution or electrolyte resistance, R_{ct} represents the electron-transfer resistance, C_{Au} is double-layer capacitance of the gold electrode, while C_{ads} is the capacitance of the adsorbed MPCAuNP species, defined as Equation 3.7:[66].

$$C_{ads} = \frac{F^2 A\Gamma}{4RT} \qquad 3.7$$

where F is the Faraday constant, A is the area of the electrode, Γ is the surface coverage, R is the gas constant, and T is the Kelvin temperature. From this equation, the values of surface coverage (determined using the one-electron processes **II** ($MPC^{3+/2+}$) and **III** ($MPC^{4+/3+}$) in Figure 3.42 are: Au-DMAET-MPCAuNP-$COOH_{1\%}$ (*ca.* 9.2 x 10^{-12} mol cm^{-2} or 5.54 x 10^{12} molecules cm^{-2}), Au-DMAET-MPCAuNP-$COOH_{50\%}$ (*ca.* 8.5 x 10^{-12} mol cm^{-2} or 5.12 x 10^{12} molecules cm^{-2}) and Au-DMAET-MPCAuNP-$COOH_{99\%}$ (*ca.* 10.7 x 10^{-12} mol cm^{-2} or 6.44 x 10^{12} molecules cm^{-2}).

Table 3.4: Comparative EIS data obtained for the electrodes in CH_2Cl_2 containing 0.1 M TBAP.

Electrodes	**Potentials (V)**	**R_s (kΩ cm^2)**	**C_{dl} (μF cm^{-2})**	**R_{ct} (kΩ cm^2)**	**C_{ads} (μF cm^{-2})**	**Γ (mol cm^{-2})**	**K_{et} (s^{-1})**
Au-DMAET-MPCAuNP-$COOH_{1\%}$	0.532	3.06 (0.870)	9.50 (4.164)	8.56 (8.964)	12.43 (7.839)	9.17 x 10^{-12}	4.69 ± 0.45
	0.784	3.01 (0.832)	9.93 (4.271)	7.38 (8.928)	13.05 (7.019)	9.63 x 10^{-12}	5.19 ± 0.47
	0.955	2.96 (0.760)	11.07 (3.644)	9.57 (9.370)	11.79 (8.010)	8.7 x 10^{-12}	4.43 ± 0.41
Au-DMAET-MPCAuNP-$COOH_{50\%}$	0.532	3.34 (0.640)	10.01 (3.114)	11.56 (9.425)	8.67 (6.763)	6.4 x 10^{-12}	4.98 ± 0.41
	0.784	3.25 (0.648)	10.98 (3.293)	9.49 (8.156)	12.05 (6.925)	8.89 x 10^{-12}	4.37 ± 0.42
	0.955	3.25 (0.584)	12.83 (3.022)	11.13 (9.320)	10.98 (7.746)	8.1 x 10^{-12}	4.09 ± 0.38
Au-DMAET-MPCAuNP-$COOH_{99\%}$	0.532	9.67 (1.106)	10.50 (3.684)	56.65 (8.605)	14.54 (7.665)	1.07 x 10^{-11}	0.61 ± 0.07
	0.784	9.61 (1.067)	11.02 (3.478)	63.08 (8.842)	13.94 (8.044)	1.03 x 10^{-11}	0.57 ± 0.06
	0.955	9.56 (1.075)	12.83 (3.678)	60.31 (9.767)	15.09 (8.776)	1.11 x 10^{-11}	0.55 ± 0.08

Assuming a closed-packed structure of the surface MPCAuNP assembly, this corresponds to a (centre-to-centre) inter-nanoparticle distance of approximately 4 nm. This value is smaller than the physical diameter of 14 nm (core + mixed ligand monolayers), and represents a surface coverage of about a magnitude higher than the expected monolayer for 14 nm (i.e., 8.47 x 10^{-12} mol cm^{-2} or 5.10 x 10^{11} molecules cm^{-2}). The reason for this higher coverage is possibly due to relatively higher assembling time used in this work. However, attempts at using short assembling time did not produce noticeable voltammeric response, necessitating the longer assembling period (18 h) used in this study.

For all the MPCAuNP-modified gold electrodes, the slopes of the Bode plots (log $|Z|$ vs. log f, Figure 3.43d) are approximately similar (*ca*. –0.62, r^2 = 0.992) at the mid frequency region, indicative of pseudocapacitive behaviour. At high frequency regions, the slopes are almost zero, indicative of resistive behaviour at these high frequency regions. The phase angles seen on the other Bode plots (i.e., –phase angle (ϕ) vs. log f, Figure 3.43d) are in the range of 49 - 60°, which are less than the 90° expected of an ideal capacitive behaviour. These results indicate that both C_{Au} and C_{ads} used in the fitting are constant phase elements (CPE), not true double-layer capacitances. CPE arises from such factors as (i) the nature of the electrode (e.g., roughness

and polycrystallinity), (ii) distribution of the relaxation times due to heterogeneities existing at the electrode/electrolyte interface, (iii) porosity and (iv) dynamic disorder associated with diffusion [67-69].

The electron transfer rate constant (k_{et} / s^{-1}) of each of the electrodes was obtained from [66]:

$$k_{et} = \frac{1}{2R_{ct}C_{ads}} \qquad 3.8$$

From Table 3.4, it is seen that the average k_{et} value decreases as the concentration of the surface-exposed –COOH group in the protecting monolayer ligand increases: Au-DMAET-MPCAuNP-$COOH_{1\%}$ (~ 5 s^{-1}) > Au-DMAET-MPCAuNP-$COOH_{50\%}$ (~ 4 s^{-1}) >> Au- DMAET-MPCAuNP-$COOH_{99\%}$ (~ 0.5 s^{-1}). Considering that the ionisation constant (pK_a) values of alkanols are inherently higher than their corresponding alkanoic acids [70]. Thus, this trend may be interpreted in terms of the hydrophobicity or affinity of the terminal functional groups (-COOH and –OH) with organic solvent such as CH_2Cl_2. Considering that the pK_a of –OH based monolayer ligands will be higher that their –COOH counterparts, the extent to which these MPCAuNPs will associate with the organic solvents will decrease as MPCAuNP-$COOH_{1\%}$ > MPCAuNP-$COOH_{50\%}$ > MPCAuNP-$COOH_{99\%}$.

Next, the same cyclic voltammetric experiment was carried out in 0.5 M H_2SO_4 for the three MPCAuNPs (Fig. 3.45) and made three

important findings. First, the quantized charging processes of the MPCAuNPs seen in the non-aqueous solution (Fig. 3.41) are not seen or clearly defined in aqueous solution (Fig. 3.45). This observation is in agreement with other workers who carried out similar experiments in aqueous PBS solution. The observation may be interpreted using the proposed equivalent circuit (Fig. 3.44). In organic solutions, the overall electrode double-layer capacitance is governed by the adsorbed MPCAuNPs (i.e., C_{ads} > C_{Au}, Table 3.4) [64,71] while the measured current response is the collective quantized charging of individual surface-confined MPCAuNP. In the aqueous solution, however, the inverse is the case (i.e., C_{ads} << C_{Au}) [64,71].

Second, from the comparative cyclic (Fig. 3.45a) and square wave voltammograms (SWV) (Fig. 3.45b), only the MPCPCAuNP-$COOH_{99\%}$ showed a weak redox peak at a formal potential ($E_{1/2}$) of about 0.22 V, attributed to the MPCAuNP redox process. Also, the three gold-modified MPCAuNPs, including the bare gold and Au-DMAET, showed a broad peak at ~0.45 V, which was ascribed in section 3.1.2 to surface reactions of the bare gold and/or the electric field-induced protonation/deprotonation redox processes of the DMAET SAM.

Third, it is clearly seen in Figure 3.45 that the Au-DMAET-MPCAuNP-$COOH_{99\%}$ showed slightly higher capacitive/background current than the Au-DMAET-MPCAuNP-$COOH_{1\%}$ or Au-DMAET-

MPCAuNP-COOH$_{50\%}$. This is also confirmed from the EIS experiment (Fig. 3.46, Table 3.5) where the C_{ad} value decreased as MPCAuNP-COOH$_{99\%}$ (0.51 µF) ≈ MPCAuNP-COOH$_{50\%}$ (0.51 µF) > MPCAuNP-COOH$_{1\%}$ (0.46 µF).

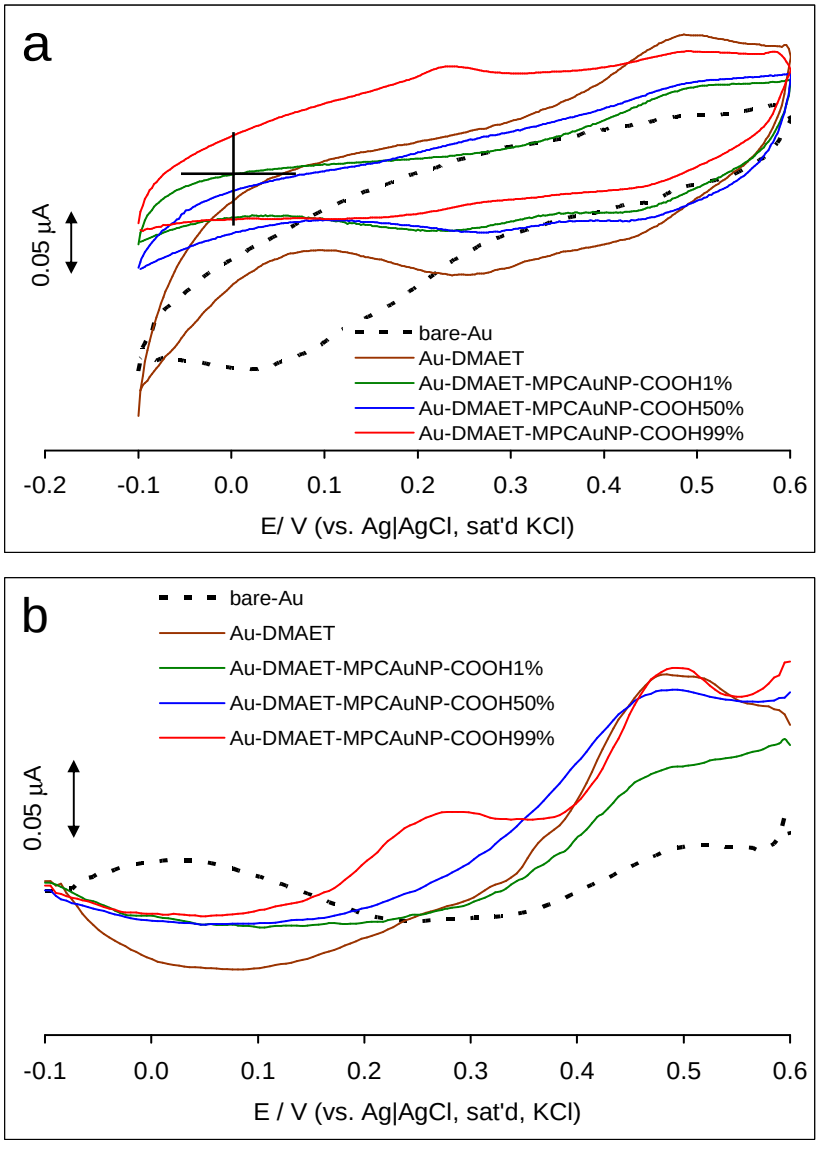

Figure 3.45: (a) CV and (b) SWV plots of bare-Au, Au-DMAET, Au-DMAET-MPCAuNP-COOH$_{1\%}$, Au-DMAET-MPCAuNP-COOH$_{50\%}$ and Au-DMAET-MPCAuNP-COOH$_{99\%}$ in 0.5 M H_2SO_4.

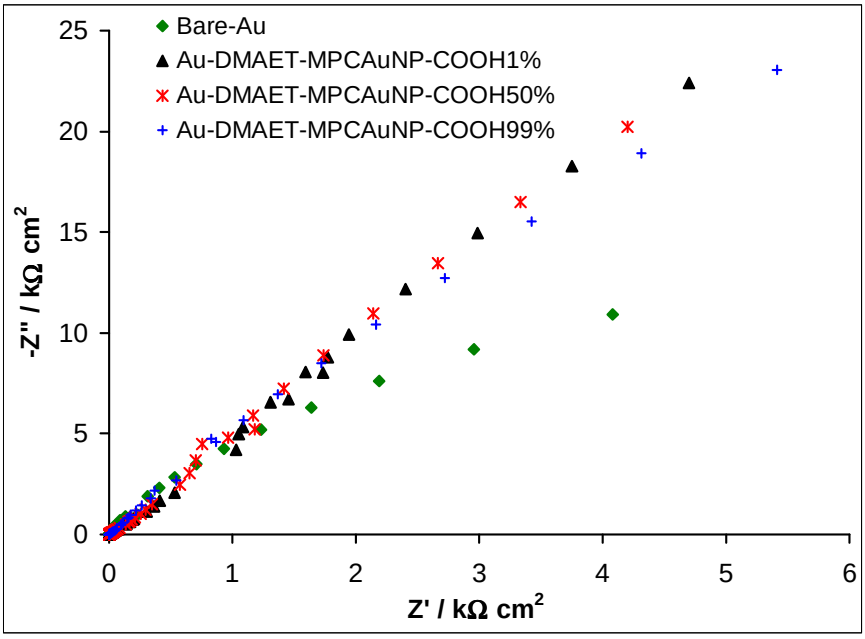

Figure 3.46: Nyquist plots resulting from bare-Au, Au-DMAET, Au-DMAET-MPCAuNP-$COOH_{1\%}$, Au-DMAET-MPCAuNP-$COOH_{50\%}$ and Au-DMAET-MPCAuNP-$COOH_{99\%}$ in 0.5 M H_2SO_4.

Table 3.5: Comparative EIS data obtained for the electrodes in H_2SO_4.

Electrodes	**R_s (Ω cm^2)**	**C_{dl} (μF cm^{-2})**	**R_{ct} (kΩ cm^2)**	**C_{ads} (μF cm^{-2})**	**K_{et} (s^{-1})**
Bare-Au	0.63 (9.524)	66.63 (3.425)	2.44 (23.488)	60.31 (13.616)	3.40
Au-DMAET-MPCAuNP-$COOH_{1\%}$	0.94 (33.465)	13.50 (6.134)	1.22 (24.429)	22.84 (12.471)	17.89
Au-DMAET-MPCAuNP-$COOH_{50\%}$	1.10 (20.416)	15.97 (5.144)	0.98 (20.125)	23.48 (10.46)	21.80
Au-DMAET-MPCAuNP-$COOH_{99\%}$	1.10 (16.168)	19.46 (4.654)	0.88 (21.889)	24.08 (7.665)	23.11

It is well established that the capacitance of any thiol-SAM is dependent on its terminal functional group, and increases as –COOH > -OH > -CH_3 [70]. In addition, the hydrophilic terminal groups are by nature quasi-liquids, while the hydrophobic groups are quasi-solids [70, 72-74], meaning that the SAMs of the –COOH terminal groups (in this case, the MPCAuNP-$COOH_{99\%}$) should be more permeable to solution ions than those of the –OH terminated MPCAuNPs (notably the Au-DMAET-MPCAuNP-$COOH_{1\%}$). The charge transfer constants, also estimated from Equation 3.8, decreased as follows: Au-DMAET-MPCAuNP-$COOH_{99\%}$ (23.11 s^{-1}) > Au-DMAET-MPCAuNP-$COOH_{50\%}$ (21.80 s^{-1}) > Au-DMAET-MPCAuNP-$COOH_{1\%}$ (17.89 s^{-1}). The higher k_{et} value of the MPCAuNP-$COOH_{99\%}$ may also be explained by the quasi-liquidity of these materials that allow the penetration of the solution species. Such penetration may be enhanced by (i) the electrostatic interactions between the negatively-charged carboxylic head group of the MPCAuNP-$COOH_{99\%}$ and the H_3O^+ of the electrolyte solution, and/or (ii) the repulsive interactions between the neighbouring ionised –COOH head groups that could create some interparticle voids or pinholes that permit the penetration of the solution ions [75]. As a contrast, the relatively lower k_{et} of the more hydrophobic MPCAuNP-$COOH_{1\%}$ is due to the unfavoured interaction of the solution ions with the unionised, quasi-solid terminal -OH groups.

3.5.3 Electron transfer Kinetics in an Aqueous Solution of $[Fe(CN)_6]^{3-/4-}$

Electron transport properties of the electrodes were studied in 0.1 M KCl containing equimolar (1 mM) mixture of $K_4Fe(CN)_6$ and $K_3Fe(CN)_6$. Typical comparative CVs are shown in Figure 3.47. The modified electrodes exhibited stable electrochemistry as the voltammograms recorded did not change after several repetitive cycling.

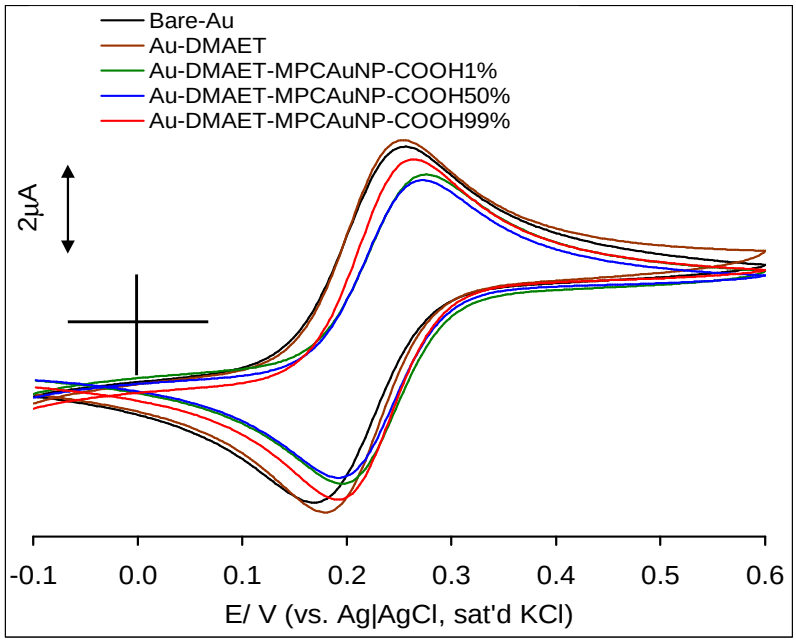

Figure 3.47: CV profiles showing bare-Au, Au-DMAET, Au-DMAET-MPCAuNP-$COOH_{1\%}$, Au-DMAET-MPCAuNP-$COOH_{50\%}$ and Au-DMAET-MPCAuNP-$COOH_{99\%}$ in 0.1 M KCl containing equimolar mixture of $K_4Fe(CN)_6$ and $K_3Fe(CN)_6$ at a scan rate of 25 mV s^{-1}.

From the CV, the current responses of the modified electrode are essentially the same as that of the bare gold electrode. This type of behaviour has been elegantly described by the theoretical framework of Davies [76-77] and Compton [76-78] as the type 4 behaviour (i.e., planar / linear diffusion, wherein the diffusion layer thickness, δ, is much larger than the insulating layer leading to a complete or heavily overlapping of the adjacent diffusion layers and a linear concentration profile).

Also, the cyclic voltammograms in Figure 3.47 shows that the peak-to-peak separation potential (ΔE_p) approximately follows this trend, MPCAuNP-$COOH_{1\%}$ (0.081 V) > MPCAuNP-$COOH_{50\%}$ (0.079 V) > MPCAuNP-$COOH_{99\%}$ (0.070 V), suggesting that the electron transport at the MPCAuNP-$COOH_{1\%}$ is slowest compared to the other electrodes. All the electrodes showed almost same formal potential ($E_{1/2} \approx 220$ mV).

Electrochemical impedance spectroscopy experiments were carried out for further insights into the electron transport properties. Figure 3.48 shows typical Nyquist plots obtained for the electrodes in 0.1 M KCl containing the $[Fe(CN)_6]^{4-}$/ $[Fe(CN)_6]^{3-}$ solution at the formal potential of the electrodes (0.22 V vs. Ag|AgCl sat'd KCl).

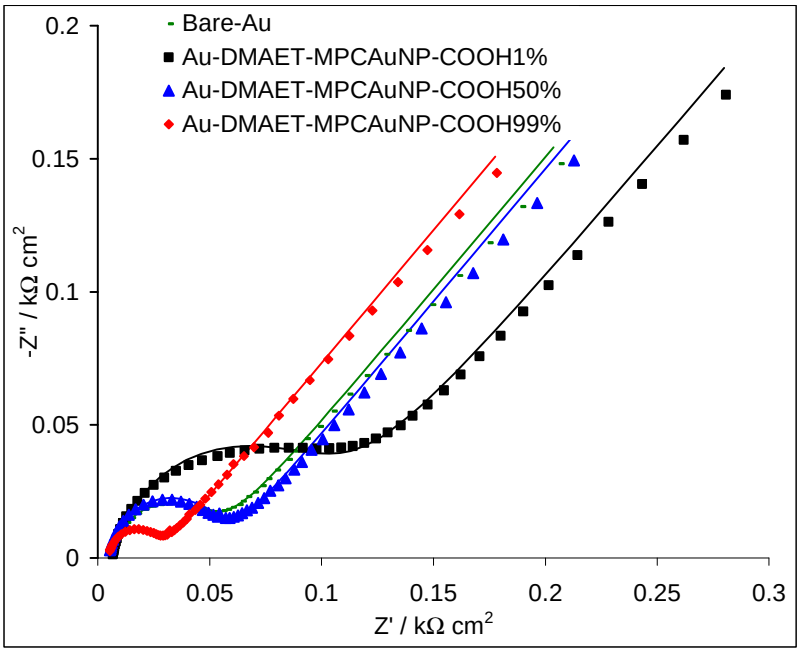

Figure 3.48: Nyquist plots resulting from bare-Au, Au-DMAET, Au-DMAET-MPCAuNP-$COOH_{1\%}$, Au-DMAET-MPCAuNP-$COOH_{50\%}$ and Au-DMAET-MPCAuNP-$COOH_{99\%}$ in 0.1 M KCl containing equimolar mixture of $K_4Fe(CN)_6$ and $K_3Fe(CN)_6$.

The EIS data were satisfactorily fitted with the modified Randles equivalent circuit model (Fig. 1.8a), wherein the true capacitance is replaced by the CPE. In this model the Z_w is the Warburg impedance, while other parameters retain their usual meaning. The apparent electron transfer rate constant (k_{app} / cm s^{-1}) of each of the electrodes was obtained from Equation 3.6 [49]. However, in this experiment R_p = R_{ct}.

$$k_{app} \approx k^o = \frac{RT}{n^2 F^2 A R_p C}$$

where the R_{ct} value is obtained from the fitted Nyquist plots and all other terms retain their usual meaning. From Table 3.6, the k_{app} value decreases as the concentration of the surface-exposed –COOH group in the protecting monolayer ligand decreases: Au-DMAET-MPCAuNP-$COOH_{99\%}$ (12.2×10^{-3} cm s^{-1}) > Au-DMAET-MPCAuNP-$COOH_{50\%}$ (5.3×10^{-3} cm s^{-1}) > Au-DMAET-MPCAuNP-$COOH_{1\%}$ (2.7×10^{-3} cm s^{-1}).

Table 3.6: Comparative EIS data obtained for the electrodes in 0.1 M KCl containing equimolar mixture of $K_4Fe(CN)_6$ and $K_3Fe(CN)_6$

Electrodes	**R_s (Ω cm^2)**	**CPE (μF cm^{-2})**	**n**	**R_{ct} (Ω cm^2)**	**$10^3 Z_w$ (μF cm^{-2})**	**$10^3 K_{app}$ (cm s^{-1})**
Bare-Au	4.96 (0.851)	47.26 (3.308)	0.86 (0.466)	46.50 (0.700)	0.12 (0.545)	(5.7±0.04)
Au-DMAET-MPCAuNP-$COOH_{1\%}$	6.17 (1.367)	84.89 (4.991)	0.83 (0.793)	96.67 (1.577)	0.10 (1.556)	(2.7±0.04)
Au-DMAET-MPCAuNP-$COOH_{50\%}$	4.76 (1.992)	18.91 (6.102)	0.89 (0.783)	50.0 (1.017)	0.11 (0.960)	(5.3±0.05)
Au-DMAET-MPCAuNP-$COOH_{99\%}$	4.44 (1.741)	20.24 (6.910)	0.89 (0.876)	23.11 (1.033)	0.12 (0.536)	(12.2±0.12)

Also from the bode plot (-Phase angle vs. log. f, Figure 3.49) the frequency synonymous with rate of reaction [78-79] at which the phase angles were observed decreased as follows: Au-DMAET-MPCAuNP-$COOH_{99\%}$ (2511.9 Hz) > Au-DMAET-MPCAuNP-$COOH_{50\%}$ (1513.6 Hz) > Au-DMAET-MPCAuNP-$COOH_{1\%}$ (316.2 Hz), corroborating the k_{app} trend.

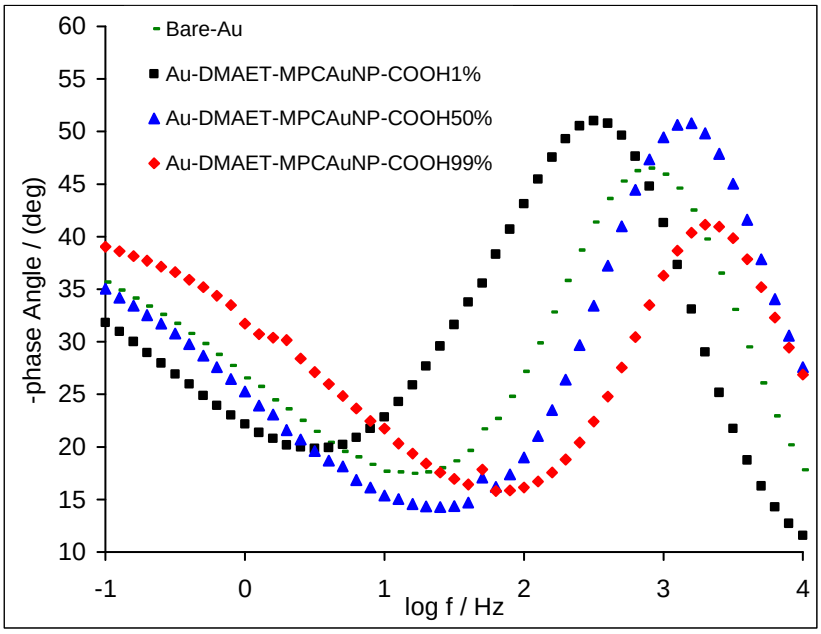

Figure 3.49: Bode plots showing the -phase angle vs. log. of frequency for the bare-Au, Au-DMAET, Au-DMAET-MPCAuNP-$COOH_{1\%}$, Au-DMAET-MPCAuNP-$COOH_{50\%}$ and Au-DMAET-MPCAuNP-$COOH_{99\%}$ in 0.1 M KCl containing equimolar mixture of $K_4Fe(CN)_6$ and $K_3Fe(CN)_6$.

The k_{app} for this outer-sphere redox probe in aqueous solution follows the same trend as in the 0.5 M H_2SO_4, but the reverse of the results obtained in the non-aqueous electrolyte already discussed. The high k_{app} value for the MPCAuNP-$COOH_{99\%}$ is interpreted as for the

experiment in the 0.5 M H_2SO_4, that is, in terms of its quasi-liquid nature as opposed to the quasi-solid nature of the MPCAuNP-$COOH_{1\%}$.

3.5.4 Surface pK_a of the MPCAuNPs

The pK_a of a surface-immobilized species is the value of the pH in contact with monolayer when half of the functional groups have been ionized [80]. Surface pK_a is easily determined with EIS strategy using solutions of $[Fe(CN)_6]^{4-}/[Fe(CN)_6]^{3-}$ of different pH values [81-83]. Figure 3.50 represent typical impedance spectral profiles of (a) MPCAuNP-$COOH_{1\%}$, (b) MPCAuNP-$COOH_{99\%}$ and Figure 3.51 shows (c) plots of the R_{ct} vs. pH for MPCAuNP-$COOH_{1\%}$ MPCAuNP-$COOH_{50\%}$ and MPCAuNP-$COOH_{99\%}$ obtained obtained in PBS solutions of $[Fe(CN)_6]^{4-}/[Fe(CN)_6]^{3-}$ (pH 1.91 – 10.0 range). There are four main findings in this experiment. First, at the pH < 8.0, the resistance to electron transport (R_{ct}) follows as MPCAuNP-$COOH_{1\%}$ > MPCAuNP-$COOH_{50\%}$ > MPCAuNP-$COOH_{99\%}$, which means that at low pH the redox species experiences more difficulty in penetrating the MPCAuNP monolayer as the concentration of the –COOH group decreases.

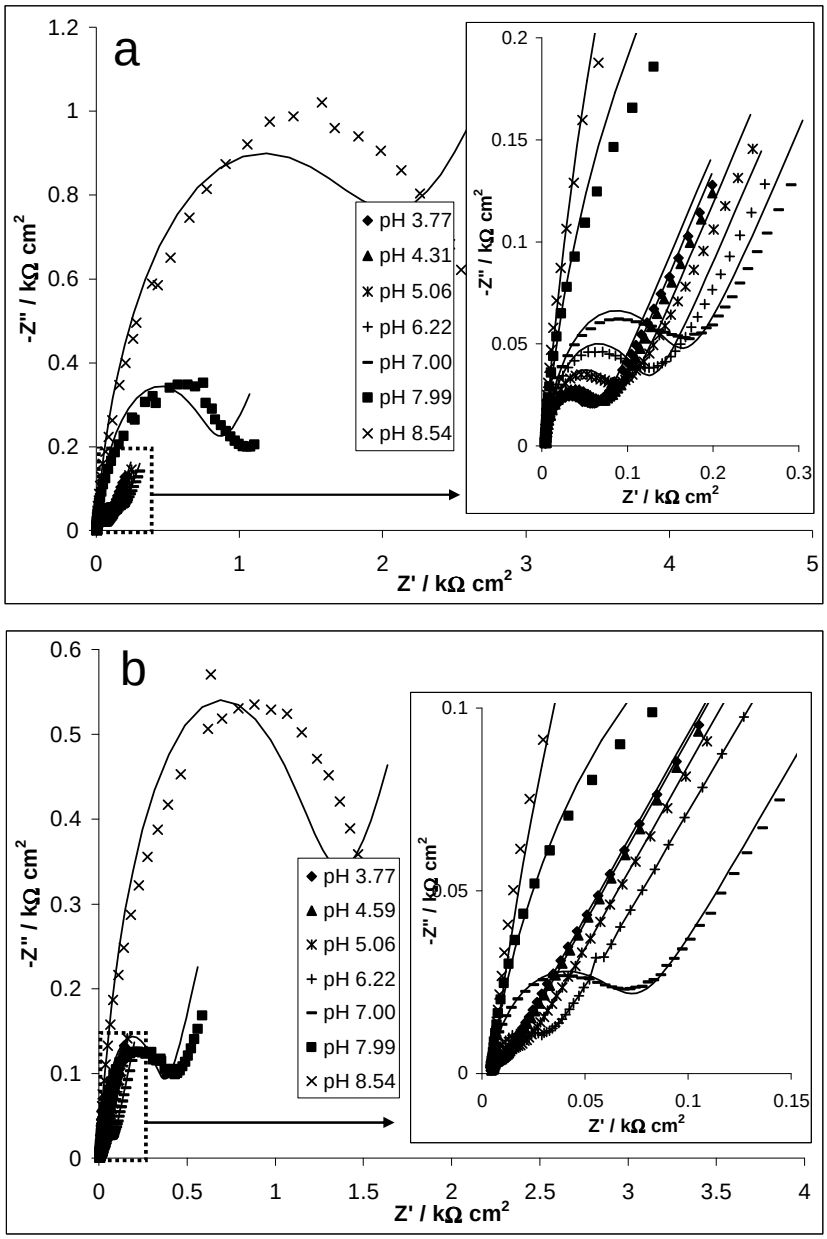

Figure 3.50: Typical impedance spectral profiles showing nyquist plots of (a) MPCAuNP-$COOH_{1\%}$, (b) MPCAuNP-$COOH_{99\%}$ obtained in PBS solutions of $[Fe(CN)_6]^{4-}/[Fe(CN)_6]^{3-}$.

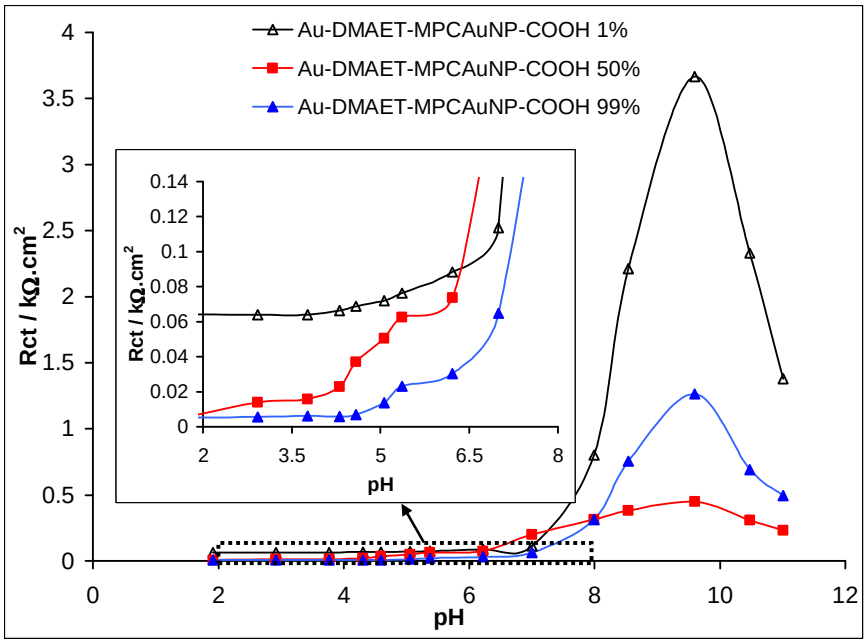

Figure 3.51: Plot of charge transfer resistance (R_{ct} / kΩ) against pH for MPCAuNP-$COOH_{1\%}$ MPCAuNP-$COOH_{50\%}$ and MPCAuNP-$COOH_{99\%}$ obtained in PBS solutions of $[Fe(CN)_6]^{4-}/[Fe(CN)_6]^{3-}$ (pH 1.91 – 10.0 range).

Second, the electron transport of the MPCAuNPs are much higher at pH > 8.0 than at pH < 8.0, indicating that the surface groups are more deprotonated at pH > 8.0, resulting in electrostatic repulsion between these negatively-charged head groups and the negatively-charged $[Fe(CN)_6]^{4-}/[Fe(CN)_6]^{3-}$. Note that at the pH > 8.0 the resistance to electron transport is more difficult at the MPCAuNP-$COOH_{1\%}$ compared to the MPCAuNP-$COOH_{50\%}$ and MPCAuNP-$COOH_{99\%}$, which means that the penetration of the redox probe at the terminal –OH group is more difficult compared to the –COOH groups. The

efficient electron transport observed for the MPCAuNP-$COOH_{50\%}$ and MPCAuNP-$COOH_{99\%}$ may be related to the enhanced repulsive interactions amongst the neighbouring deprotonated groups that create wider spaces (pinholes) for the penetration of the redox probe into the films. Third, unlike the MPCAuNP-$COOH_{1\%}$, both MPCAuNP-$COOH_{50\%}$ and MPCAuNP-$COOH_{99\%}$ exhibit a sigmoidal shape with a midpoint at ~ pH 5, signifying an initial pK_a of ~ 5. Fourth, at pH > 8, the three MPCAuNPs gave well defined sigmoidal curves; pK_a of ~8.2 for the MPCAuNP-$COOH_{1\%}$, while both MPCAuNP-$COOH_{50\%}$ and MPCAuNP-$COOH_{99\%}$ showed two pK_a values of ~5.0 and ~8.0. These two p*K*a's may be related to two possible locations of the –COOH groups, presumably the well surface-exposed –COOH groups that easily access the electrolyte, and the slightly 'buried' –COOH groups that are somewhat less easily accessible to the electrolyte solution.

In general, the electronic communication is strongly influenced by the hydrophobicity / hydrophilicity of the head groups (-OH and –COOH); in aqueous solution the electron transport of the –COOH based ligand is favoured, while in the non-aqueous medium the electron transport of the –OH based ligands is favoured. Unfortunately, there is no accessible literature for surface pK_a of MPCAuNP with which to compare the present data.

3.5.5 Voltammetric Detection of Ascorbic Acid and Epinephrine

Figure 3.52 shows comparative cyclic voltammetric evolutions at Au-DMAET-MPCAuNP-$COOH_{1\%}$, Au-DMAET-MPCAuNP-$COOH_{50\%}$ and Au-DMAET-MPCAuNP-$COOH_{99\%}$ in a PBS solution (pH 7.4) containing 10 µM ascorbic acid. Clearly, Au-DMAET-MPCAuNP-$COOH_{1\%}$ shows a significantly greater peak current response than the MPCAuNPs with higher carboxyl content. While the terminal –COOH group of the PEG-ligands and ascorbic acid are expected to be fully deprotonated at this pH 7.4 (pK_a of ascorbic acid = 4.17 [84]), the deprotonation of the terminal –OH group is highly unlikely considering the inherent high pK_a values of alkanolic compounds. Thus, the excellent suppression of the voltammetric response of the ascorbic acid by the Au-DMAET-MPCAuNP-$COOH_{99\%}$ may be attributed to the repulsive interaction between the negatively-charged ascorbic acid and the -COOH groups of the PEG-ligands.

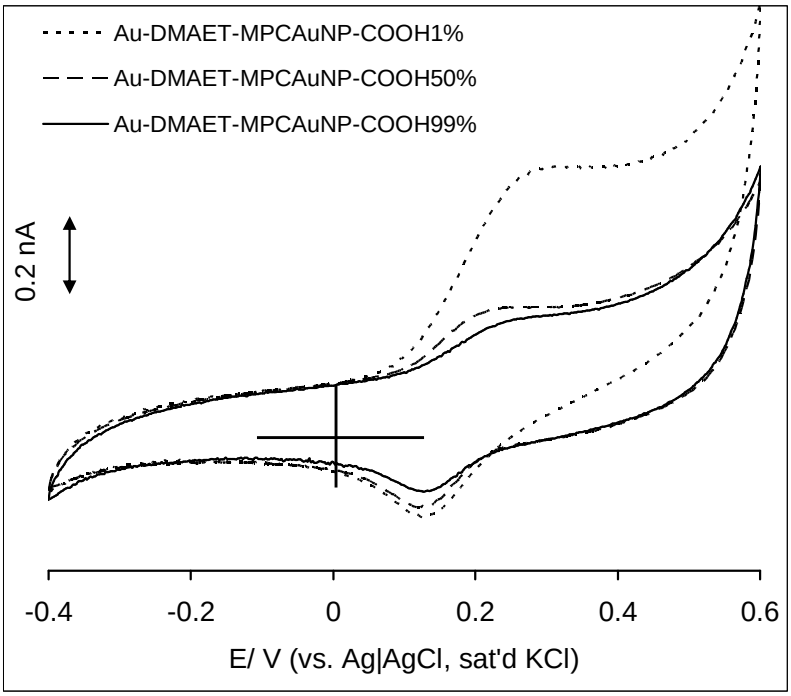

Figure 3.52: Cyclic voltammetric evolutions in 10 µM ascorbic acid at Au-DMAET-MPCAuNP-$COOH_{1\%}$, Au-DMAET-MPCAuNP-$COOH_{50\%}$ and Au-DMAET-MPCAuNP-$COOH_{99\%}$.

Figure 3.47 shows the voltammetric response of epinephrine in PBS solutions of different pH (pH 7.4 and 9.68) using the electrodes with two extreme mixtures (i.e., 1:99 and 99:1 ratios of PEG-COOH to PEG-OH ligands). Considering that epinephrine has different p*K*a's (8.7, 9.9 and 12.0 [85-87]), identical experiments in pH 7.4 and pH 9.68 were conducted. Figure 3.47 (a) and (c) shows comparative CV evolutions of Au-DMAET-MPCAuNP-$COOH_{1\%}$ and Au-DMAET-MPCAuNP-$COOH_{99\%}$ in 10 µM epinephrine pH7.4 and 9.68 respectively.

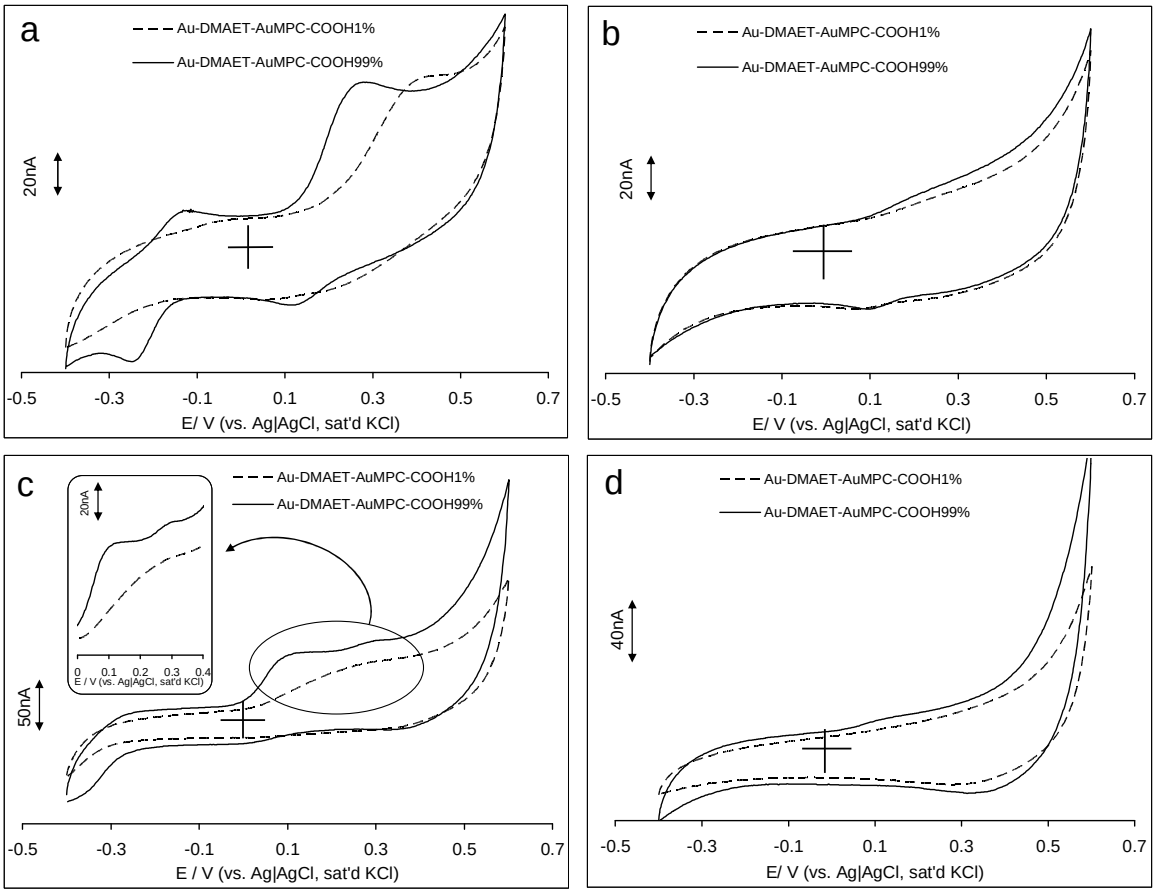

Figure 3.53: (a) and (c) shows comparative CV evolutions of Au-DMAET-MPCAuNP-$COOH_{1\%}$ and Au-DMAET-MPCAuNP-$COOH_{99\%}$ in 10 μM epinephrine pH7.4 and 9.68 respectively. (b) and (d) represent their corresponding CVs in their respective buffer solutions only.

Figure 3.40 (b) and (d) represents their corresponding CVs in their respective buffer solutions only. At pH 7.4, the onset potentials of the epinephrine were obtained at 0.10 and 0.15 V for the Au-DMAET-MPCAuNP-$COOH_{99\%}$ and Au-DMAET-MPCAuNP-$COOH_{1\%}$, respectively. The peak potential at the Au-DMAET-MPCAuNP-$COOH_{99\%}$ was at 0.3 V, while at the Au-DMAET-MPCAuNP-$COOH_{1\%}$ it was observed at a more

positive value (0.5 V). Also, in the alkaline medium (pH 9.68), Au-DMAET-MPCAuNP-$COOH_{99\%}$ and Au-DMAET-MPCAuNP-$COOH_{1\%}$ showed onset potential of 0.0 and 0.07 V, respectively. The current response at the Au-DMAET-MPCAuNP-$COOH_{99\%}$ is better defined than that at the Au-DMAET-MPCAuNP-$COOH_{1\%}$. These results clearly indicate that the Au-DMAET-MPCAuNP-$COOH_{99\%}$ exhibits more electrocatalytic activity towards the detection of epinephrine than the Au-DMAET-MPCAuNP-$COOH_{1\%}$. Also, unlike the Au-DMAET-MPCAuNP-$COOH_{1\%}$, the Au-DMAET-MPCAuNP-$COOH_{99\%}$ showed two oxidation peaks for epinephrine in pH 9.68 at 0.1 and 0.3 V (inset of Figure 3.47). The occurrence of these two oxidation peaks may be related to the oxidation of the different forms of the epinephrine in this pH conditions.

From the results in pH 7.4, considering peak current responses, it seems that for a simultaneous detection of the AA and EP in physiological pH medium, the Au-DMAET-MPCAuNP-$COOH_{1\%}$ may prove to be the best electrode. Further experiments are required to prove this concept, and will be the subject of future engagement. However, the key finding in this experiment is that one can possibly tune the ability of the gold nanoparticles to electrochemically recognize AA or EP in aqueous medium by smart manipulation of the ratios of their monolayer-protecting PEG-ligands.

Reference:

1. J. M. Campiña, A. Martins, F. Silva, *J. Phys. Chem. C.* 111 (2007) 5351.
2. H.S. White, J.D. Peterson, Q. Cui, K.J. Stevenson, *J. Phys. Chem. B* 102 (1998) 2930.
3. I. Burgess, B. Seivewright, R.B. Lennox, *Langmuir* 22 (2006) 4420.
4. S.M. Rosenthal, I.J. Burgess, *Electrochim. Acta* 53 (2008) 6759.
5. C.P. Smith, H.S. White, *Langmuir* 9 (1993) 1.
6. H. O. Finklea in Encyclopedia Chemistry, A. J. Bard and I. Rubinstein, Eds., Marcel Dekker: New York, 1996, Vol.19, pp109-335.
7. T.R. Lee, R.D. Carey, H.A. Biebuyck, G.M. Whitesides, *Langmuir* 10 (1994) 741.
8. D. Nkosi, K.I. Ozoemena, *Electrochim. Acta* 53 (2008) 2782.
9. B.O. Agboola, K.I. Ozoemena, *Phys.Chem.Chem.Phys* 10 (2008) 2399.
10. F. Caruso, E. Rodda, D.N. Furlong, V. Haring, *Sens. Actuators B* 41 (1997)189.
11. C. Saby, B. Ortiz, G.Y. Champagne, D. Bèlanger, *Langmuir* 13 (1997) 6805.

12. P. Abiman, A. Crossley, G.G. Wildgoose, J.H. Jones, R.G. Compton, *Langmuir* 23 (2007) 7847.

13. P. Abiman, G.G. Wildgoose, A. Crossley, J.H. Jones, R.G. Compton, *Chem. Eur. J.* 13 (2007) 9663.

14. J. Pillay, K. I. Ozoemena, *Electrochem. Commun*. 7 (2007) 1816.

15. K.I. Ozoemena, T. Nyokong, *Electrochim. Acta* 51 (2006) 2669.

16. B-Y. Chang, S-Y. Hong, J-S. Yoo, S-M. Park, *J. Phys.Chem. B.* 110 (2006) 19385.

17. L. Yang, Y. Li, *Biosens. Bioelectron*. 20 (2005) 1407.

18. G.D. Christian, Analytical Chemistry, sixth ed., John Wiley and Sons, New York, 2004.

19. S. Majdi, A. Jabbari, H. Heli, A. A. M-Movahedi, *Electrochimica Acta* 52 (2007) 4622.

20. Z. Yang, G. Hu, X. Chen, J. Zhao, G. Zhao, *Colloids Surf. B: Biointerf.* 54 (2007) 230.

21. L. Wang, J. Bai, P. Huang, H. Wang, L. Zhang, Y. Zhao, *Electrochem. Commun.* 8 (2006) 1035.

22. M.D. Hawley, S.V. Tatawawadi, S. Piekarski, R.N. Adams, *J.Am. Chem. Soc.* 89 (1967) 447.

23. S. H. Kim, J. W. Lee, I-H. Yeo, *Electrochim. Acta* 45 (200) 2889.

24. K. I. Ozoemena, D. Nkosi, J. Pillay, *Electrochim. Acta* 53 (2008) 2844.

25. N.B. Li, W. Ren, H.Q. Luo, *Anal. Chim. Acta* 378 (1999) 151.

26. J.H. Zagal, S. Lira, S. Ureta-Zanartu, *J. Electroanal. Chem.* 210 (1986) 95.

27. J.P. Collman, M. Kaplun, C.J. Sunderland, R. Boulatov, *J. Am. Chem. Soc.* 126 (2004) 11166.

28. A. Star, T.R. Han, J. Christophe, P. Gabriel, K. Bradley, G. Gruner *Nano. Lett.* 3 (2003) 403.

29. J. Zhang, M. Kambayashi, M. Oyama, *Electroanalysis* 17 (2005) 408.

30. B. O. Agboola, K. I. Ozoemena, *Electroanalysis* 20 (2008) 1696.

31. J.Y. Bai, L. Wang, H.J. Wang, P.F. Huang, Y.Q. Zhao, S.D.Fan, *Microchim. Acta* 156 (2007) 321.

32. L. Wang, J. Bai, P. Huang, H. Wang, L. Zhang, Y. Zhao, *Int. J.Electrochem. Sci.* 1 (2006) 238.

33. Y. B. He, H. Q. Luo, N. B. Li, *Instrum. Sci. Technol.* 35 (2007) 163.

34. B. Zeng, Y. Yang, F. Zhao, *Electroanalysis* 15 (2003) 1054.

35. B. Fang, X.-H. Deng, X.-W. Kan, H.-S. Tao,W.-Z. Zhang, M.-G. Li, *Anal. Lett.* 39 (2006) 697.

36. Y.-X. Sun, S.-F. Wang, X.-H. Zhang, Y.-F. Huang, *Sens.Actuators B* 113 (2006) 156.

37. A. Salimi, C. E. Banks, R. G. Compton, *Analyst* 129 (2004) 225.

38. [a] P. Liljeroth, D. Vanmaekelbergh, V. Ruiz, K. Kontturi, H. Jiang, E. Kauppinen, B.M. Quinn, *J. Am. Chem. Soc.* 126 (2004) 7126. [b] D. Bethell, M. Brust, D.J. Schiffrin, C. Kiely, *J. Electroanal. Chem.* 409 (1996) 137.

39. A.B.P. Lever, E.L. Milaeva, G. Speier, In Phthalocyanines: Properties and Applications; eds.; VCH Publishers: New York, 1993.

40. H.O. Finklea, In Encyclopaedia of Analytical Chemistry, Applications, Theory and Instrumentations; eds.; R.A. Meyers, Wiley: Chichester, 2000.

41. H.O. Finklea, *J. Am. Chem. Soc.* 114 (1992) 3173.

42. H.O. Finklea, M.S. Ravenscroft, D.A. Snider, *Langmuir* 9 (1993) 223.

43. J. Liu, M.N. Paddon-Row, J.J. Gooding, *J. Phys. Chem. B* 108 (2004) 8460.

44. J.J. Gooding, A. Chou, J. Liu, D. Losic, J.G. Shapter, D.B. Hibbert, *Electrochem. Commun.* 9 (2007) 1677.

45. B.S. Flavel, J. Yu, A.V. Ellis, J.G. Shapter, *Electrochim. Acta* 54 (2009) 3191.

46. K.M. Kadish, K.M. Smith, R. Guilard, The Porphyrin Handbook; eds.; Academic Press, Boston, 2003.

47. M.P. Somashekarappa, J. Keshavaya, S. Sampath, *Pure Appl. Chem.* 74 (2002) 1609.

48. E. Sabatini, I. Rubinstein, *J. Phys. Chem.* 91 (1987) 6663.

49. A.J. Bard and L.R. Faulkner, in *Electrochemical Methods: Fundamentals and Applications, 2nd ed*., John Wiley & Sons Inc., Hoboken, NJ, 2001.

50. E. Barsoukov, J.R. Macdonald, Impedance Spectroscopy: Theory Experiment, and Applications; 2nd ed.; Wiley: Hoboken, New Jersey, 2005.

51. M.E. Orazem, B. Tribollet, Electrochemical Impedance Spectroscopy; John Wiley & Sons Inc: Hoboken, NJ. 2008.

52. J-Y. Park, Y-S. Lee, B.H. Kim, S-M. Park, *Anal. Chem.* 80 (2008) 4986.

53. F. Caruso, E. Rodda, D. N. Furlong and V. Haring, *Sens. Actuators* B 41 (1997)189.

54. M. Aslam, N.K. Chaki, Jadab Sharma, K. Vijayamohanan, *Current Applied Physics* 3 (2003) 115.

55. K. Stolarczyk, R. Bilewics, *Electrochim. Acta* 51 (2006) 2358.

56. J. Tien, A. Terfort, G.M. Whitesides, *Langmuir* 13 (1997) 5349.

57. Y. Lui, Y. Wang, H. Lu, R.O. Claus, *J. Phys. Chem. B* 103 (1999) 2035.

58. H. Paloneimi, M. Lukkarinen, T. Aäritalo, S. Areva, J. Leiro, M. Heinonen, K. Haapakka, J. Lukkari, *Langmuir* 22 (2006) 74.

59. J. Shen, Y. Hu, C. Li, C. Qin, M. Shi, M. Ye, *Langmuir* 25 (2009) 6122.

60. T. R. Tshikhudo, D. Demuru, Z. Wang, M. Brust, A. Secchi, A. Arduini and A. Pochini, *Angew. Chem. Int. Ed.* 44 (2005) 2.

61. S. Chen, R.S. Ingram, M.J. Hostetler, J. J. Pietron, R.W. Murray, T.G. Schaaff, J.T. Khoury, M.M. Alvrez, R.L. Whetten, *Science* 280 (1998) 2098.

62. J.F. Hicks, F.P. Zamborini, R.W. Murray, *J. Phys. Chem. B* 106 (2002) 7751.

63. B. Su, H.H. Girault, *J. Phys. Chem. B* 109 (2005) 23925.

64. S. Chen, R.W. Murray, *J. Phys. Chem. B* 103 (1999) 9996.

65. S. Chen, R.W. Murray, *Langmuir* 15 (1999) 682.

66. S. E. Creager, T.T. Wooster, *Anal. Chem.* 70 (1998) 4257.

67. D.D. MacDonald, *Electrochim. Acta* 51 (2006) 1376.

68. M.E. Orazem, B. Tribollet, *Electrochemical Impedance Spectroscopy*. New Jersey: John Wiley & Sons; 2008.

69. E. Barsoukov, J.R. Macdonald (Eds), *Impedance spectroscopy: Theory, Experiment, and Applications*. 2nd ed. New Jersey: John Wiley & Sons; 2008.

70. P.Y. Bruice, *Organic Chemistry*, fiftth ed., Person Prentice Hall, NewJersey, 2007, pp. 1041–1045, chapter 22.

71. S. Chen, *J. Phys. Chem. B* 104 (2000) 663.

72. H.O. Finklea, in: R.A. Meyers (Ed.), Encyclopedia of Analytical Chemistry: Applications, Theory and Instrumentations, Vol.11, Wiley & Sons, Chichester, 2001.

73. C.E.D. Chidsey, D.N. Loiacono, *Langmuir* 6 (1990) 682.

74. K.I. Ozoemena, T. Nyokong and P. Westbroek, *Electroanalysis* 15 (2003) 1762.

75. Y.Y. Jun, K.S. Beng, *Electrochem. Commun*. 6 (2004) 87.

76. T.J. Davies, R.G. Compton, *J. Electroanal. Chem.* 585 (2005) 63.

77. T.J. Davies, C.E. Banks, R.G. Compton, *J. Solid. State Electrochem.* 9 (2005) 797.

78. X. Dai, G.G. Wildgoose, C. Salter, A. Crossley, R.G. Compton, *Anal. Chem*. 78 (2006) 102.

79. E. Sabatani, I. Rubinstein, *J. Phys. Chem.* 91 (1987) 6663.

80. T.R. Lee, R.D. Carey, H.A. Biebuyck, G.M. Whitesides, *Langmuir* 10 (1994) 741.

81. D. Nkosi, K.I. Ozoemena, *Electrochim. Acta* 53 (2008) 2782.

82. B O. Agboola, K.I. Ozoemena, *Phys. Chem. Chem. Phys.* 10 (2008) 2399.

83. R.Z. Shervedani, M. Bagherzadeh, S.A. Mozaffari, *Sens. Actuators B* 115 (2006) 614.

84. M.H. Pournaghi-Azar, R. Ojani, *Talanta* 42 (1995) 1839.

85. S. L. Jewett, S. Eggling, L. Geller, *J. Inorg. Biochem*. 66 (1997) 165.

86. C. E. Sanger-van de Griend, A. G. Ek, M. E. Widahl-Nasman, E. K. M. J. Andersson, *Pharm. Biomed. Anal.* 41 (2006) 77.

87. E. L. Ciolkowski, K. M. Maness, P. S. Cahlil, R. M. Wightman, *Anal. Chem.* 66 (1994) 3611.